

## INFORMATION TO USERS

This manuscript has been reproduced from the microfilm master. UMI films the text directly from the original or copy submitted. Thus, some thesis and dissertation copies are in typewriter face, while others may be from any type of computer printer.

**The quality of this reproduction is dependent upon the quality of the copy submitted.** Broken or indistinct print, colored or poor quality illustrations and photographs, print bleedthrough, substandard margins, and improper alignment can adversely affect reproduction.

In the unlikely event that the author did not send UMI a complete manuscript and there are missing pages, these will be noted. Also, if unauthorized copyright material had to be removed, a note will indicate the deletion.

Oversize materials (e.g., maps, drawings, charts) are reproduced by sectioning the original, beginning at the upper left-hand corner and continuing from left to right in equal sections with small overlaps. Each original is also photographed in one exposure and is included in reduced form at the back of the book.

Photographs included in the original manuscript have been reproduced xerographically in this copy. Higher quality 6" x 9" black and white photographic prints are available for any photographs or illustrations appearing in this copy for an additional charge. Contact UMI directly to order.

# UMI

A Bell & Howell Information Company  
300 North Zeeb Road, Ann Arbor MI 48106-1346 USA  
313/761-4700 800/521-0600



REAL TIME IMPLEMENTATION OF  
THE WIDE AREA AUGMENTATION SYSTEM FOR  
THE GLOBAL POSITIONING SYSTEM  
WITH AN EMPHASIS ON IONOSPHERIC MODELING

A DISSERTATION  
SUBMITTED TO THE DEPARTMENT AERONAUTICS AND ASTRONAUTICS  
AND THE COMMITTEE ON GRADUATE STUDIES  
OF STANFORD UNIVERSITY  
IN PARTIAL FULFILLMENT OF THE REQUIREMENTS  
FOR THE DEGREE OF  
DOCTOR OF PHILOSOPHY

YI-CHUNG CHAO

JUNE, 1997

**UMI Number: 9802010**

**Copyright 1997 by  
Chao, Yi-Chung**

**All rights reserved.**

---

**UMI Microform 9802010  
Copyright 1997, by UMI Company. All rights reserved.**

**This microform edition is protected against unauthorized  
copying under Title 17, United States Code.**

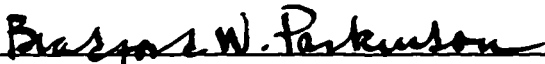
---

**UMI**  
**300 North Zeeb Road  
Ann Arbor, MI 48103**

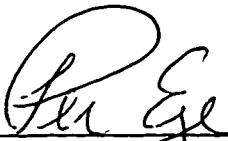
© Copyright by Yi-chung Chao 1997

All Rights Reserved

I certify that I have read this dissertation and that in my opinion it is fully adequate, in scope and in quality, as a dissertation for the degree of Doctor of Philosophy.

  
Bradford W. Parkinson (Principal Adviser)

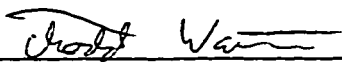
I certify that I have read this dissertation and that in my opinion it is fully adequate, in scope and in quality, as a dissertation for the degree of Doctor of Philosophy.

  
Per K. Enge

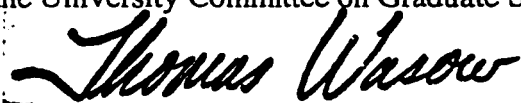
I certify that I have read this dissertation and that in my opinion it is fully adequate, in scope and in quality, as a dissertation for the degree of Doctor of Philosophy.

  
J. David Powell

I certify that I have read this dissertation and that in my opinion it is fully adequate, in scope and in quality, as a dissertation for the degree of Doctor of Philosophy.

  
Todd Walter

Approved for the University Committee on Graduate Studies:

  
Dean of Graduate Studies

# Abstract

The Global Positioning System (GPS) has demonstrated great potential to improve civilian aviation. However, before GPS can be used as a primary navigation system, the system's integrity and accuracy must be enhanced to meet the safety standards set by the Federal Aviation Administration (FAA).

To meet these requirements, the FAA proposed and initiated the development of the Wide Area Augmentation System (WAAS) for GPS. WAAS augments GPS with a ground network of GPS receivers to deliver the Wide Area Differential GPS corrections and system integrity alerts, as well as adding an extra ranging signal from a geosynchronous satellite to increase the continuity and time availability of the service. This augmentation will enable WAAS to be the primary navigation system for en route flight, terminal area approach, and non-precision approach, and can provide accurate vertical guidance for Category I precision approach.

This thesis presents the real-time WAAS implementation to meet the accuracy requirement of Category I precision approaches, especially includes algorithms for calibrating interfrequency biases, and for creating an ionospheric grid model. A feedback algorithm for generating the confidence level of the ionospheric correction shown in this thesis is proven to be useful. Furthermore, an integrity monitoring indicator using  $\chi^2$  has been proposed for detecting local ionospheric disturbances, which may represent the most significant threat to WAAS in the coming solar maximum around the year 2000.

# Acknowledgments

I would like to thank my advisor, Professor Bradford W. Parkinson, for giving me the opportunity to pursue this research. His insight and enthusiasm has inspired me and given me confidence and discipline to conduct research. I would also like to thank Professor Per Enge for his clear guidance and comprehensive knowledge about WAAS, which helped me to overcome the difficulties in the past years. I thank my defense and reading committees, including Professor Paul Segall, Professor Jonathan How and Dr. Todd Walter. Special thanks go to Professor J. David Powell for his clear teaching in my graduate study at Stanford, for his generous offer of his Piper Dakota, and for being the pilot for all the flight tests described in this thesis.

All the members at Stanford GPS and WAAS Laboratories are greatly appreciated for their friendship and great team work. I especially thank Dr. Todd Walter, who manages the WAAS Laboratory, for his daily discussion and his hard work which makes Stanford WAAS feasible. I would like to express my appreciation to Fiona Walter for her reading my thesis draft thoroughly and her suggestions. I also thank Dr. Hiro Uematsu for his discussions about the implementation of Square Root Information Filter used this study.

I most gratefully acknowledge the support and assistance of the FAA Technical Center, Program Office (AGS-100), and FAA personnel at Arcata, CA, Elko, NV and San Diego, CA.

Thanks are also due to Trimble Navigation engineers for their help in developing the reference station receiver data collection program. Especially, I have benefited from the discussions with Dr. Gary Lennon about the receiver interfrequency bias.

Last but not least, I want to express my highest respect to my parents in Taiwan. They provide endless love and courage to allow me to complete my study. Thanks also go to Yeh's family, and especially to my dearest wife, Vanessa. She has always kept me in high spirit in the past years. With her encouragement, I am highly motivated to pursue my career.



# Table of Contents

Abstract .....	iv
Acknowledgments .....	v
Table of Contents .....	vi
List of Figures .....	ix
List of Tables .....	xii
List of Abbreviations .....	xiii
<b>Chapter 1 Introduction .....</b>	<b>1</b>
1.1 The Goal .....	1
1.2 The Current Status of GPS .....	3
1.3 Previous Work of WAAS Development .....	6
1.4 WAAS Configuration .....	7
1.5 Challenges of WAAS .....	8
1.6 Previous Work of Ionospheric Modeling .....	8
1.7 Research Contributions .....	10
1.7.1 Interfrequency Bias Calibration .....	10
1.7.2 Ionospheric Grid Model Estimator Design .....	11
1.7.3 Integrity Monitoring .....	11
1.7.4 WAAS Algorithm Development .....	11
1.8 Thesis Organization .....	12
<b>Chapter 2 Real-time Implementation of WAAS .....</b>	<b>13</b>
2.1 Wide Area Differential GPS .....	13
2.2 Challenges of Real-time Implementation .....	16
2.3 GPS Signal Modeling .....	17
2.4 Stanford WAAS Processing .....	18

2.5 Reducing the Local Errors .....	19
2.5.1 Troposphere Delay Modeling .....	20
2.5.2 Dual Frequency Carrier Smoothing of Pseudorange and Ionospheric Delays .....	21
2.6 Satellite Location and Clock Corrections .....	23
2.6.1 Common View Time Transfer .....	25
2.6.2 Single Difference Snap-shot Satellite Location Determination .....	26
2.6.3 Satellite Clock Bias Estimation .....	29
2.6.4 Master Receiver Clock Estimation .....	29
2.6.5 Further Improvement on Satellite Clock/Location Estimation .....	29
2.7 Ionospheric Corrections .....	30
2.8 WAAS Weighted Navigation Solutions .....	31
2.9 WAAS Data Format and Messages .....	34
<b>Chapter 3 Ionospheric Measurements and Interfrequency Bias Calibration ...</b>	<b>37</b>
3.1 Ionospheric Measurements .....	37
3.2 Ionospheric Thin Slab Model .....	40
3.3 Interfrequency Bias Calibration .....	42
3.4 IFB Estimation Methodology .....	45
3.5 Temperature Dependence of the IFBs .....	49
3.6 Difficulties in Estimating the IFBs .....	51
<b>Chapter 4 Modeling and Integrity Monitoring of the Grid Model .....</b>	<b>54</b>
4.1 WAAS Ionospheric Vertical Delay Grid Model .....	54
4.1.1 Grid Model Implementation .....	55
4.1.2 Challenges of WAAS Grid Model .....	56
4.2 Grid Model Error Components .....	57
4.3 Error Propagation .....	58
4.3.1 Data Screening .....	59
4.3.2 IFB Errors .....	60
4.3.3 Obliquity Errors .....	60
4.3.4 Error Propagation of Grid Vertical Delay Model .....	62

4.4 Grid Modeling Estimators .....	62
4.4.1 Weighted Least-squares Estimator .....	63
4.4.2 Minimum Mean Square Error Estimator .....	66
4.4.3 GIVE Feedback Algorithm .....	67
4.4.4 Grid Correction .....	68
4.5 Integrity Monitoring .....	70
4.6 Difficulty in Using GIVE .....	74
<b>Chapter 5 Stanford WAAS Test Results .....</b>	<b>76</b>
5.1 Stanford WAAS Testbed .....	76
5.2 National Satellite Testbed .....	78
5.3 Stanford WAAS Data Flow .....	79
5.4 Test Results .....	80
<b>Chapter 6 Conclusion .....</b>	<b>84</b>
6.1 Summary .....	84
6.2 Conclusions .....	86
6.3 Recommendations of Future Work .....	87
6.4 A Final Remark .....	88
<b>Appendix A Position and Velocity from GPS .....</b>	<b>89</b>
<b>Appendix B Satellite Location Error Covariance Analysis of</b>	
<b>LADGPS and WADGPS .....</b>	<b>94</b>
<b>Appendix C Tropospheric Delay Model .....</b>	<b>99</b>
<b>Appendix D Dual-frequency Carrier-Smoothing Algorithm .....</b>	<b>104</b>
<b>Appendix E Master Clock Estimation .....</b>	<b>110</b>
<b>Appendix F Ionospheric Delay .....</b>	<b>114</b>
<b>Appendix G Interfrequency Bias Calibration Filter .....</b>	<b>122</b>
<b>Appendix H WAAS Ionospheric Grid Model User Algorithm .....</b>	<b>131</b>
<b>Bibliography .....</b>	<b>134</b>

# List of Figures

Figure 1.2.1 The Global Positioning System .....	3
Figure 1.2.2 GPS Standard Positioning Service .....	5
Figure 1.4.1 The Wide Area Augmentation System Configuration .....	7
Figure 2.1.1 Local Area Differential GPS .....	14
Figure 2.1.2 Wide Area Differential GPS .....	15
Figure 2.1.3 Comparison of Error Degradation of LADGPS and WADGPS .....	16
Figure 2.4.1 Stanford WAAS Data Processing .....	19
Figure 2.5.1 Dual Frequency Smoothing of Ionospheric Delays and Pseudoranges .....	22
Figure 2.5.2 Dual Frequency Smoothing Result .....	23
Figure 2.6.1 Simulation of Satellite Slow/Fast Corrections .....	28
Figure 2.6.2 Separation of Satellite Slow/Fast Corrections .....	28
Figure 2.7.1 WAAS Ionospheric Vertical Delay Grid Model .....	31
Figure 2.9.1 Basic WAAS Data Block Format .....	34
Figure 3.1.1 GPS Ionospheric Line-of-Sight Delay .....	37
Figure 3.1.2 Ionospheric Free Electron Density Profiles .....	38
Figure 3.1.3 Ionospheric Diurnal Variation .....	39
Figure 3.2.1 Ionospheric Thin Slab Model and Obliquity Factor .....	41
Figure 3.3.1 Interfrequency Bias Nomenclature .....	42
Figure 3.4.1 IFB Estimation Methodology .....	45
Figure 3.4.2 Stanford Testbed IPP Distribution and IFB Estimation Results .....	47
Figure 3.4.3 IFB Effects on WAAS Navigation Errors .....	48
Figure 3.5.1 Temperature Dependency of IFBs .....	50
Figure 3.5.2 Estimation Results of IFB Temperature Dependence Experiment ...	51
Figure 3.6.1 Ionospheric Mean Height Variation .....	52

Figure 4.1.1 Data Flow of WAAS Ionospheric Vertical Delay Grid Model .....	55
Figure 4.1.2 WAAS Ionospheric Grid for the Continental U.S. ....	56
Figure 4.2.1 Stanford WAAS Grid Model Processing Procedures .....	58
Figure 4.3.1 Ionospheric Variation Gradient Investigation .....	59
Figure 4.3.2 Obliquity Factor Error Calculation .....	61
Figure 4.3.3 WAAS Ionospheric Grid Model Error Propagation .....	62
Figure 4.4.1 Illustration of Grid Model Generation .....	63
Figure 4.4.2 Nominal Ionospheric Model: Klobuchar Model .....	65
Figure 4.4.3 Ionospheric Correlation Functions .....	65
Figure 4.4.4 Feedback Algorithm for GIVE Generation .....	67
Figure 4.4.5 GIVE to Cover 99.9% Ionospheric Error .....	68
Figure 4.4.6 User Ionospheric Model form WAAS MOPS .....	69
Figure 4.4.7 WAAS Grid Correction Error and UIVE .....	70
Figure 4.5.1 Fast Decorrelated Ionospheric Bubble .....	71
Figure 4.5.2 $\chi^2$ and Measurement Consistency .....	72
Figure 4.5.3 $\chi^2$ Histogram for the Real Ionospheric Data over CONUS .....	74
Figure 5.1.1 Stanford WAAS Testbed .....	76
Figure 5.1.2 Wide Area Reference Station Setup .....	77
Figure 5.2.1 FAA National Satellite Testbed .....	78
Figure 5.3.1 Stanford WAAS Data Processing Flow .....	79
Figure 5.4.1 Flight Test Using Piper Dakota and Local Data Link .....	80
Figure 5.4.2 WAAS Airborne User Positioning Errors .....	81
Figure 5.4.3 WAAS Static User Velocity Errors .....	82
Figure 5.4.4 WAAS Static User Positioning Error Histogram .....	83
Figure B.1.1 Geometry of LADGPS .....	95
Figure C.1.1 Geometry of Tropospheric Delay .....	102
Figure D.2.1 Dual Frequency Smoothing of Ionospheric Delays and <i>PRs</i> .....	108
Figure D.2.2 Dual Frequency Smoothing Result .....	109
Figure E.1 Results of Master Clock Estimation .....	113
Figure F.3.1 Geometry of Obliquity Factor and IPP Location .....	118

Figure G.1.1 The Sun-Earth Coordinate Frame .....	123
Figure G.1.2 The Solar-Magnetic Coordinate System .....	124
Figure G.4.1 IFB Estimation Program Block Diagram and Flow Chart .....	129
Figure H.1 Interpolation Algorithm Definition .....	132
Figure H.2 Ionospheric Grid Model Interpolation Weighting Function .....	133

# List of Tables

Table 2.9.1 WAAS Message Types .....	36
Table 3.4.1 Statistics of Relative Receiver IFBs in Stanford WAAS Testbed .....	49
Table 3.4.2 95% and 99.9% of the Stanford WAAS Vertical Error .....	49
Table 4.3.1 Maximal Sunspot Numbers (SSNs) for the Last Five Solar Maximum ...	61
Table 5.4.1 Summary of 3-D Error Histogram .....	83

# List of Abbreviations

C	Speed of Light	4
CVTT	Common View Time Transfer	25
DH	Decision Height	2
DME	Distance Measuring Equipment	2
DoD	Department of Defense	3
DOF	Degree Of Freedom	72
FAA	Federal Aviation Administration	2
GEO	Geosynchronous Satellite	6
GIC	GPS Integrity Channel	6
GIVE	Grid Ionospheric Vertical Error	32,55
GPS	Global Positioning System	1
IBLS	Integrity Beacon Landing System at Stanford	16
IFB	Interfrequency Bias	44,57
ILS	Instrument Landing System	8
IPP	Ionospheric Pierce Point	41,54
IRI 90	Ionospheric Reference International model, year 90	38,39,59
LAAS	Local Area Augmentation System	13
LADGPS	Local Area Differential GPS	13
MMSE	Minimum Mean Square Error	63,66
MOPS	Minimum Operation Performance Standard	19
NDB	Non-Directional Beacon	2
NSTB	National Satellite Testbed	9
OF	Obliquity Factor	41,55,56,60
PR	Pseudorange	4, 17,54
PRN	Pseudo Random Noise, or Satellite ID number	3 34
RAIM	Receiver Autonomous Integrity Monitoring	33



RVR	Runway Visual Range	2
SA	Selective Availability of GPS	4
SPS	Standard Positioning Service	5
SRIF	Square Root Information Filter	46
SSN	Sun Spot Number	59
UDRE	User Differential Range Error	32
UHF	Ultra High Frequency	19
UIVE	User Ionospheric Vertical Error	56
VOR	VHF Omnidirectional Radio	2
VPL	Vertical Protection Limit	3,32
WAAS	Wide Area Augmentation System	1
WADGPS	Wide Area Differential GPS	6,14
WLS	Weighted Least Squares Estimator	63
WMS	Wide area Master Station	7,19,54
WRS	Wide area Reference Station	7,19

# Chapter 1

## Introduction

**T**he development of the Wide Area Augmentation System (WAAS) is on-going research regarding the application of the Global Positioning System (GPS) as a navigation tool. In this introduction, I address the following questions:

- ◆ What is our goal in using GPS?
- ◆ Why do we need to augment GPS?
- ◆ What are the challenges of this augmentation?

### 1.1 The Goal

Our goal is to use GPS as the primary navigation system for commercial aircraft. This system differs from that of other GPS applications and other navigation systems in three ways:

- ◆ Our system is safety-critical. Because it is a primary navigation sensor, it not only has to have good accuracy but also has to meet all other critical requirements, like integrity and continuity, to guarantee flight safety. More specifically, the system has to provide accurate navigation guidance for the aircraft's taking off to Category I precision approach down to 200 ft decision height.
- ◆ Navigation signals come from space. Since all its navigation signals come from artificial satellites in space, unique problems are created. For example, the system has to account for the problems caused by atmospheric delays and radio frequency interference of the signals.
- ◆ This system provides wide coverage. We want to use this system for different phases of flight and therefore need to cover a large geographical area; at the same time, the system needs to be cost effective.

In order to address these issues, the system must meet accuracy and integrity requirements

established by the U.S. Federal Aviation Administration (FAA).

- ♦ **Accuracy.** The accuracy requirement is usually measured in terms of a 95% confidence level. For example, oceanic flight or en route flight over the continental U.S. requires only an accuracy of several hundred meters for guidance. However, as the aircraft approaches the airport, the pilots will certainly need higher navigation accuracy:

***Non-precision approach:*** The non-precision approach is a category of instrument approach without accurate vertical position information. It is used primarily by most general aviation. The 100-meter horizontal accuracy of a non-precision approach is required 99.999% of the time. Currently, ground based radio navigation aids such as VHF omnidirectional radio (VOR), distance measuring equipment (DME), and nondirectional beacon (NDB), are used for determining the horizontal position. The vertical guidance of the non-precision approach is usually provided by baro-altimeters. Judging from the current development of the navigation system (section 1.2), the GPS can satisfy this non-precision accuracy requirement but needs to improve its time availability for this type of approach.

***Precision approach:*** In this type of approach, pilots are provided with guidance for both the vertical and the horizontal directions. The three categories of precision approaches are rated by the pilot's visibility of the runway environment at the decision height (DH) and the horizontal visibility on the runway, known as runway visual range (RVR). Category I requires the airport's RVR be at least 2400 ft and the pilot must have the runway environment insight by the 200 ft DH . If at the DH the pilot is unable to see the run way, the approach must be abandoned. Category II is more stringent and requires pilots to have at least 1200 ft RVR and the DH is 100 ft. Category III operations include aircraft automatic landing with RVR less than 1200 ft [FAA AC 120-28, 1984]. Today, all three types of precision approach guidance criteria are provided by the Instrument Landing System (ILS), which uses a glide slope of approximately 3° for vertical positioning and a localizer for horizontal positioning. The real challenge for WAAS is to provide stringent *vertical guidance of 7.6 meters accuracy 95% of the time* as required for a Category I precision approach [FAA WAAS, 1994].

♦ **Integrity.** Integrity, the system's ability of a system to detect problems and alert users in a timely manner, is of one of the main measures of flight safety. An integrity risk arises when an undetected navigation system error, such as system failure or accuracy degradation, occurred that can result in danger to the aircraft. For the Category I precision approach, the navigation system can tolerate less than  $10^{-7}$  to  $10^{-8}$  probability of failure to deliver the integrity alert to guarantee flight safety. Furthermore, the system must be able to alert the user within 6 seconds once an integrity threat is detected. Integrity also requires all users to be updated within 6 seconds of any change to Vertical Protection Level (VPL) bound.

## 1.2 The Current Status of GPS

The GPS is a satellite-based ranging system with a constellation of 24 satellites in six 12-hour orbits. This navigation system was developed and implemented by the U.S. Department of Defense (DoD) and has been fully deployed since 1993. . Figure 1.2.1 presents the configuration of the GPS constellation. Each satellite continuously broadcasts its own specific pseudo-random noise (PRN) code for identification and

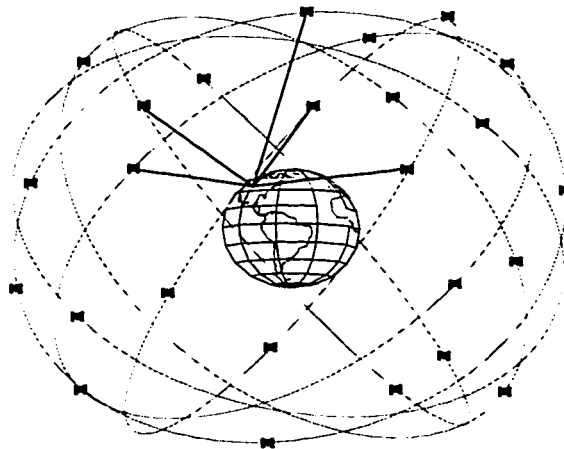


**Figure 1.2.1 The Global Positioning System**

The constellation comprises 21 satellites with three spares in six orbits. Each orbit is at  $55^\circ$  inclination angle and has a period of 11 hr 57 min. To determine its position, a receiver needs at least four satellites in view to measure at least four pseudoranges to estimate three dimensions of location and user clock error.

ranging purposes. The satellite PRN code and navigation information are broadcast at L-band microwave frequencies. The flight time of the GPS PRN signal traveling through space from satellite to receiver provides the basis for the range measurement. Civilian users measure these timing signals, termed pseudo-ranges ( $PRs$ ), from the satellites to calculate their positions [Appendix A includes basic position and velocity estimation algorithms].

The control station at Colorado Springs is responsible for orbit determination of the satellites and system maintenance. The satellite navigation information includes satellite location and ranging signals. The ranging measurement, pseudorange, is the time-of-flight of the signals from the satellite to the user. It is converted to range by multiplying the speed of light ( $C$ ), Equation (1.2.1). Because pseudorange is a timing signal, it contains not only the true range between the satellite and the receiver but also receiver and satellite clock biases.

Furthermore, as the signal travels through the ionosphere and troposphere, it experiences delays. Finally, as the receiver measures the signal, the local multipath and the receiver thermal noise also introduce errors. Therefore, we can write the  $PR$  measurement between the  $j^{th}$  satellite and  $i^{th}$  receiver as

$$PR_i^j = \Delta t_{transit} \cdot C \quad (1.2.1)$$

$$= \underbrace{\rho_i^j}_{\text{geometric range}} + \underbrace{b_i}_{\text{receiver clock bias}} - \underbrace{B_i^j}_{\text{satellite clock bias, including SA (fast)}} + \underbrace{I_i^j}_{\text{ionospheric delay (slow)}} + \underbrace{T_i^j}_{\text{tropospheric delay (slow \& local)}} + \underbrace{M_i^j}_{\text{multipath error}} + \underbrace{E_i^j}_{\text{measurement noise}}$$

The errors in  $PR$ , together with satellite geometry, affect the user positioning accuracy directly.

Currently, the DoD is deliberately adding errors, called Selective Availability (SA), to the satellite clock biases to degrade the positioning accuracy for national security reasons. SA has an rms of 23 meters [van Grass et al., 1996] and is the largest error component. The second largest component is the ionospheric delay. When it is very active, the ionosphere can cause a 30 to 50 meter delay in the pseudorange. For a single frequency receiver, this delay is usually corrected by the ionospheric model broadcast in the navigation message [Klobuchar, 1987] and can be reduced to a 4 meter rms ionospheric

error [Parkinson, 1996]. Compared to the rate of the SA variation, which is about 0.2 m/sec, the ionospheric delay is slow, varying at about 0.5 m/min ( $8 \times 10^{-3}$  m/sec) at most [Klobuchar et al., 1993].

Despite all the error sources, civilian users of the GPS Standard Positioning Service (SPS) can still reach 100 meter ( $2\text{-}\sigma$ ) horizontal accuracy and 150 meters ( $2\text{-}\sigma$ ) vertical accuracy. An example of SPS performance is shown in Figure 1.2.2. This level of SPS accuracy is global and accessible 24 hours a day in all weather conditions. Note that the key element enabling GPS to provide this accuracy in positioning result is the high quality of spaceborne Cesium and Rubidium clocks that are used. Their behavior can be predicted and corrected very well, thus bringing the determination of satellite orbit to better than 10 meters.

Even though GPS is better and more convenient compared to many other current navigation systems in terms of accuracy, its positioning service still has to be improved in order for it to serve as the primary navigation sensor for aviation around the world. An additional problem is that if a satellite failure or ionospheric disturbance occurred to threaten the system performance, the satellites would have to wait for the control station to uplink the information. As a result there would be delays, which would raise the integrity risks.

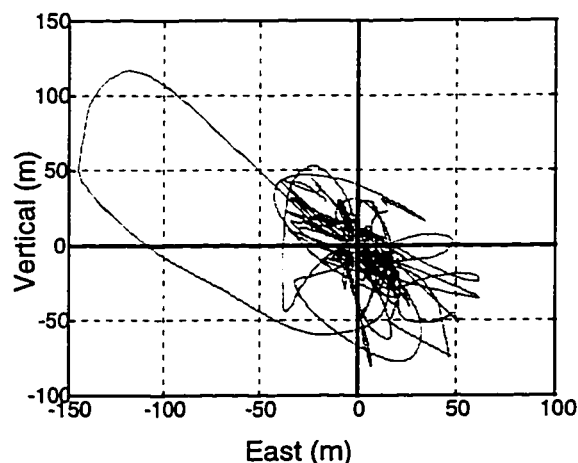


**Figure 1.2.2 GPS Standard Positioning Service**

An example of positioning error collected using a Trimble 4000 SSE receiver for 10 hours at a surveyed reference station.

### **1.3 Previous Work of WAAS Development**

Some mechanisms for improving GPS have already been proposed in order to meet the requirements of the primary navigation system. First of all, a group of researchers, Enge and Inmarsat's Nagle and Kinal [Enge et al., 1990, Nagel and Kinal., 1990] introduced the GPS Integrity Channel concept. They proposed to use geosynchronous (GEO) satellites to broadcast the system integrity information to the users in real-time. Their study showed that by broadcasting coarse corrections for SA, the GPS Integrity Channel will be able to meet the non-precision approach requirements.

Around the same time, Kee and Parkinson invented the Wide Area Differential GPS (WADGPS) [Kee et al., 1990 & 1991]. They demonstrated good accuracy over a large geographical area with only a few GPS differential reference stations. Later, the FAA's top managers, Robert Loh and Joseph Dorfler, asked the RTCA Inc., a nonprofit company that generate standards for aerospace (formerly Radio Technology Committee of Aerospace) the question "Can we combine the benefits from both the GPS Integrity Channel and WADGPS and further improve GPS performance?" Loh and Dorfler proposed the concept of WAAS. Enge [Enge et al., 1990] studied the proposal and concluded that by broadcasting both integrity information and WADGPS corrections at a 250 bit/sec data rate, WAAS would be able to meet the accuracy requirements for the Category I precision approach.

RTCA has already delivered the WAAS Minimum Operation Performance Standard for the non-precision approach and is working on standards for the precision approach [WAAS MOPS, 1995]. This standard will be used as the guideline for the development of consumer electronics. Currently, the FAA is developing WAAS with Hughes Aircraft Company and an operational WAAS is expected to be deployed by late or early 1999.

## 1.4 WAAS Configuration

Figure 1.4.1 illustrates the WAAS configuration. In this configuration, GPS is augmented with a network of reference stations. Each of the Wide Area Reference Stations (WRSs) is equipped with dual-frequency GPS receivers and meteorological sensors. All the measurements will be transferred to the Wide Area Master Station (WMS) for data processing. Because of the wide geographical coverage of the WRS network, WMS will be able to estimate the satellite clock error, to calculate 3-dimensional orbital error components, and to model the ionosphere. Simultaneously, WMS will also use the network measurements to monitor the system integrity. Both the correction and integrity information will be packed into the WAAS message and broadcast to single-frequency users via the GEO at the GPS L1 frequency. With this configuration, WAAS is aimed at being the primary aircraft navigation system capable of providing Category I precision approach to 200 ft DH.

Notice that the signals at the GPS L2 frequency were originally intended for military use only and the U.S. government did not guarantee the service of this signal [Parkinson

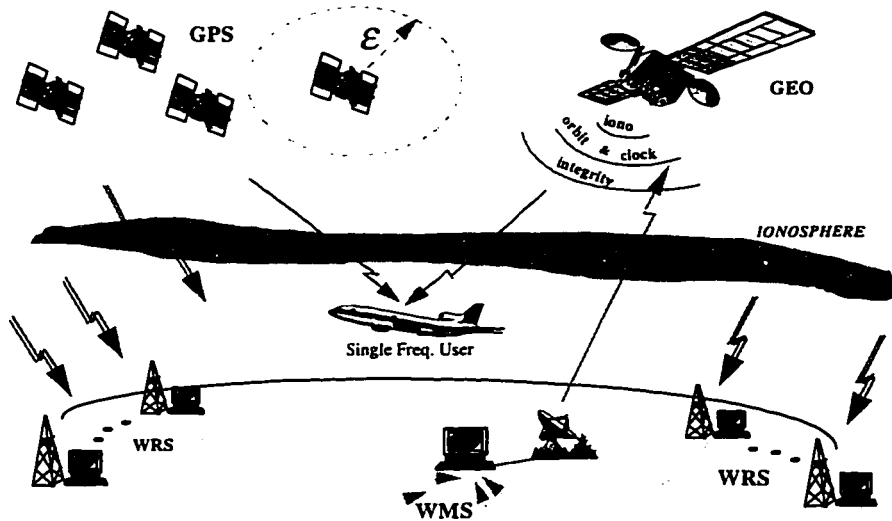


Figure 1.4.1 The Configuration of the Wide Area Augmentation System of GPS



et al., 1996]. Thus the dual-frequency receivers can not be certified for civilian aviation use and it is necessary for the WAAS of GPS to target single-frequency civilian users and to provide ionospheric corrections for them. Note that U.S. government just announced the guarantee of L2 carrier phase in the civilian application. However, the guarantee of the civilian L2 code phase is still under discussion [ION Newsletter, 1997].

A further augmentation is that the GEO will also send out ranging signals to aid the navigation solution. This augmentation enhances the overall satellite geometry and reduces the system dependency on individual GPS satellites. It therefore increases the continuity and time availability of the navigation service. The most important improvement provided by WAAS is that it will cover a large area and therefore all the airports under the coverage, large or small, will be capable of providing the Category I precision approach for the aircraft immediately without installing any ground Instrument Landing System equipment. However, airports still need to provide landing lights and special patterns on the runway surface to be qualified for providing Category I precision approach.

## **1.5 Challenges of WAAS**

Several researchers, using covariance analysis, have already predicted that WAAS will be able to provide enough accuracy for Category I precision approaches [Enge, et al., 1995, Pullen et al., 1995]. However, the real challenge is to meet the accuracy requirement in real time, especially under the 250 bit/sec data rate constraint. Note that the WAAS data rate is constrained because the signal will be broadcast at the GPS L1 frequency and must not interfere with the GPS signals. Therefore, the limited power and wide coverage requirements for the GEO result in the low data rate.

A more important point is that the system has to prove its integrity monitoring capability in real time using the network information. This integrity monitoring includes the satellite health, orbital errors, ionospheric disturbances, etc. Because of the nature of the ionosphere, the ionospheric disturbances may be most difficult to detect, and integrity

monitoring of this element becomes one of the most significant challenges to the success of WAAS.

To verify the system's performance, Stanford University joined the FAA effort and built a 3-WRS WAAS Testbed on the West Coast in 1993. Today we are processing data in real time from a dedicated network of 20 WRSs from the FAA National Satellite Testbed, which is a research and development project for WAAS. The primary WAAS contract was awarded to Hughes Aircraft Company in March of 1996 for both software and hardware development. The initial delivery of this navigation system is expected to occur in 1998.

## **1.6 Previous Ionospheric Modeling Work**

The followings are the studies have been done towards the modeling of ionosphere:

- ◆ Klobuchar proposed a vertical ionospheric delay model for the GPS single frequency ionospheric corrections [Klobuchar, 1986]. The parameters of this model, now being transmitted from GPS as part of the navigation message, can reduce 50 to 60% rms error of the ionospheric delay [Feess et al., 1987].
- ◆ Cohen explored the possibility of using a variation of obliquity factor to separate the ambiguities and to estimate the ionospheric delay from single receiver carrier-phase measurements [Cohen et al., 1992].
- ◆ For the study of ionospheric modeling and satellite interfrequency bias estimation, researchers at Jet Propulsion Laboratory generated a global ionospheric map using a world wide GPS network [Mannucci et al., 1993, Wilson et al., 1993]. Sardon studied the problem using only one reference station [Sardon et al., 1994]. Both of these are mainly scientific studies which provides no work on ionospheric correction integrity.
- ◆ In 1994, one of the FAA's main contractors, MITRE Corp., proposed the WAAS ionospheric grid model and implemented an initial static test [El-Arini et al., 1994]. This model has been adopted by the WAAS Minimum Operation Performance

Standard for real-time implementation. The ionospheric model of the present research is based on this grid concept.

Note that none of the above efforts have studied the integrity monitoring problem for the WAAS ionospheric corrections.

## **1.7 Research Contributions**

The goal of the Stanford effort is to develop WAAS algorithm and to demonstrate that WAAS meets Category I precision approach requirements in real time. Within this context, the central theme of this thesis is about the WAAS algorithm development, especially the improvement of the ionospheric model. My specific contributions are described in the sections below:

### **1.7.1 Interfrequency Bias Calibration**

I developed and verified a new algorithm for the estimation of the satellite and receiver interfrequency biases. These biases can be as high as 10 meters and are both satellite and receiver dependent. Even with hardware precalibration, their values can still deviate from the calibrated values by more than one meter because of variation of receiver ambient temperature and other factors. This variation affects the accuracy of line-of-sight ionospheric delay measurements. If the WAAS master station uses these biased measurements to generate the corrections for ionospheric vertical delay, then the user's positioning accuracy is degraded.

Using the interfrequency bias estimation developed in this study, the accuracy of the bias calibration has been demonstrated at better than 30 cm. The user's 95% vertical positioning accuracy has been improved by more than one meter, compared to the solutions that using old precalibrated values. By eliminating these systematic biases, one not only can reduce the WAAS users' average positioning errors, but can also reduce the error distribution. Most importantly, this calibration reveals the accuracy that is necessary for further system error analysis and integrity monitoring. These additional

efforts can be used in near real time to update the interfrequency biases which are expected to change over time.

### **1.7.2 Ionospheric Grid Model Estimator Design**

Using an ionospheric modeling estimator based on a grid algorithm, I demonstrated the accuracy of the WAAS ionospheric grid modeling over the Continental U.S., and the feasibility of integrity monitoring of the grid ionospheric vertical model; Specifically, I formalized the modeling approach using a Weighted Least Squares algorithm with ionospheric spatial correlation function. This modeling technique also includes an error propagation procedure and error analysis. This spatial correlation function was experimentally determined from archived National Satellite Testbed March 1996 data. To account for possible faster decorrelation in the coming maximum solar cycle anticipated around the turn of the century, I implemented a more conservative curve in a real-time algorithm for the system robustness. This algorithm will also be useful for real-time WAAS operation.

### **1.7.3 Integrity Monitoring**

This study also proposed integrity monitoring mechanism for the detection of ionospheric disturbance in the grid ionospheric vertical delay model. This scheme uses  $\chi^2$  to calculate the goodness-of-fit in the modeling process. From real-time data processing results, a threshold is set using the degree-of-freedom of the  $\chi^2$  parameter to detect ionospheric fast-decorrelated disturbances.

### **1.7.4 WAAS Algorithm Development**

In addition, the Stanford WAAS development team, of which I have been a member since its formation, has demonstrated the accuracy of the Category I precision approach using a three-station mini-WAAS Testbed on the West Coast since 1993. At the time of writing, using 22 reference stations from National Satellite Testbed, we can demonstrate real-time accuracy of 3 meters in the horizontal and 4 meters in the vertical 95% of the time. We developed both hardware and software for real-time implementation, and have

flight-tested the system at Palo Alto and Truckee, Lake Tahoe areas. Specifically, we developed a real-time algorithm for separating the slow and fast WAAS corrections for the 250 bit/second data constraint and validated the message types described in the WAAS Minimum Operation Performance Standard. That is, our algorithm effectively separated the satellite clock errors (fast), the satellite orbital errors (slow) and ionospheric delays (also slow).

For the real-time data processing, I developed an efficient clock filter for estimating the free-running receiver Rubidium oscillator under the effect of satellite SA. With the Common View Time Transfer method, I proposed and implemented a single difference snap-shot estimator (discussed in Chapter 2) for separating the satellite clock and orbital errors.

## **1.8 Thesis Organization**

This thesis discusses the real-time implementation of the Wide Area Augmentation System for GPS, especially the generation and integrity monitoring of the ionosphere corrections. Chapter 2 introduces the main functions in the WAAS, including wide area corrections and system integrity monitoring. Then it focuses on the overall real-time WAAS implementation, including the data processing techniques for satisfying the GEO broadcast data rate constraints. Chapter 3 describes the ionospheric measurements and the measurement interfrequency bias calibration methodology and results. The generation and integrity monitoring for the grid ionospheric vertical delay model are detailed in Chapter 4. Chapter 5 presents the real-time test results from Stanford's WAAS implementation, including those from the Stanford West Coast WAAS Testbed and the National Satellite Testbed. Chapter 6 concludes this thesis and suggests some work for future research. Finally, the appendices detail the implementation of estimators and methodologies that were used in this research but omitted in the thesis body, mainly for the sake of clarity.

## Chapter 2

# Real-time Implementation of WAAS

**W**AAS is a cost-effective navigation system providing wide-range geographical coverage. Designed to improve GPS positioning accuracy, real-time integrity monitoring capability, continuity and time availability of the navigation service, it is intended to be the primary navigation sensor on board an aircraft. This chapter discusses the real-time implementation of the Stanford WAAS, especially the generation of wide area corrections and integrity alerts.

### 2.1 Wide Area Differential GPS

In order to provide the 7.6-meter (95%) vertical guidance requirement of Category I landings, GPS accuracy must be improved by differential technology which provides corrections for users' measurements. One commonly used differential GPS technology is called Local Area Differential GPS (LADGPS) [Beser and Parkinson, 1981, Teasley et al., 1980]. Applied to aviation, it is often referred to as the Local Area Augmentation System (LAAS) by FAA. LADGPS employs a reference station at a surveyed position which, because of its known location, is able to calculate GPS pseudorange errors for each satellite in view. Each error for a specific satellite is the sum of satellite SA, ionospheric and tropospheric delays, and the reference station's multipath and receiver noises. The users in the vicinity of the reference stations apply these scalar corrections to cancel the common errors between them and the reference station to improve their positioning accuracy. However, as the users move away from the reference station, they no longer share the same pseudorange error as the reference station due to spatial decorrelation of the errors. For example, the orbital error and the ionospheric delay are dependent on the receiver-satellite line-of-sight (LOS), and as the user moves farther away from the reference station, the LOSs are different and the accuracy of the corrections is degraded.

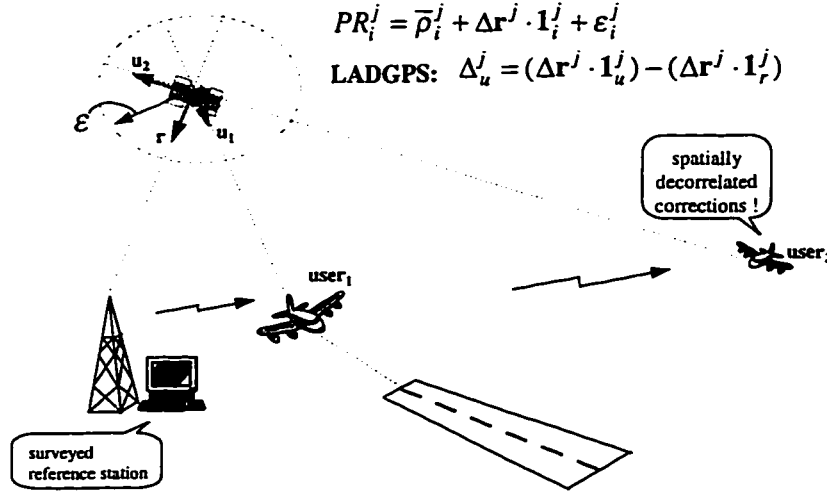


**Figure 2.1.1 Local Area Differential GPS**

$\bar{\rho}_i^j$  is the geometrical range between receiver  $i$  and satellite  $j$  calculated from broadcast satellite ephemeris.  $\Delta \mathbf{r}^j$  is the satellite  $j$  location error.  $\mathbf{1}_r^j$  is the unit line-of-sight vector from reference station to satellite  $j$  and  $\mathbf{1}_u^j$  is that from the user to the same satellite.  $\Delta_u^j$  is the correction residual of LADGPS.

The decorrelated corrections caused by the satellite orbital location error are shown in Figure 2.1.1. For a user within 200 to 300 km of the reference station, the LOSs  $\mathbf{1}_u^j$  and  $\mathbf{1}_r^j$  are nearly identical; therefore the residual of corrected errors in the pseudorange ( $\Delta_u^j$ ) of the user is very small. However, for a user beyond 500 km from the reference station, the correction becomes worse and the  $\Delta_u^j$  becomes larger. For an orbit error of 10 meters, the worst case  $\Delta_u^j$  can be as large as 0.25 meters for a baseline of 500 km (Appendix B).

To serve large areas, a better way of solving this problem is to provide the users with the components of each pseudorange error, that is, the estimate of the satellite location 3-dimensional errors,  $\Delta \mathbf{r}^j$ , so that the users can project the corrections onto their own LOSs. This technique is called the Wide Area Differential GPS (WADGPS). WADGPS was invented at Stanford University by Kee and Parkinson [Kee et al, 1991]. This approach differs from LADGPS in deploying multiple reference stations over a wide geographical area. With this broad scattering of the reference station network, WADGPS is able to estimate the GPS satellite orbital location 3-dimensional error components and satellite clock error (mainly SA). Furthermore, employing the dual-frequency reference receivers,

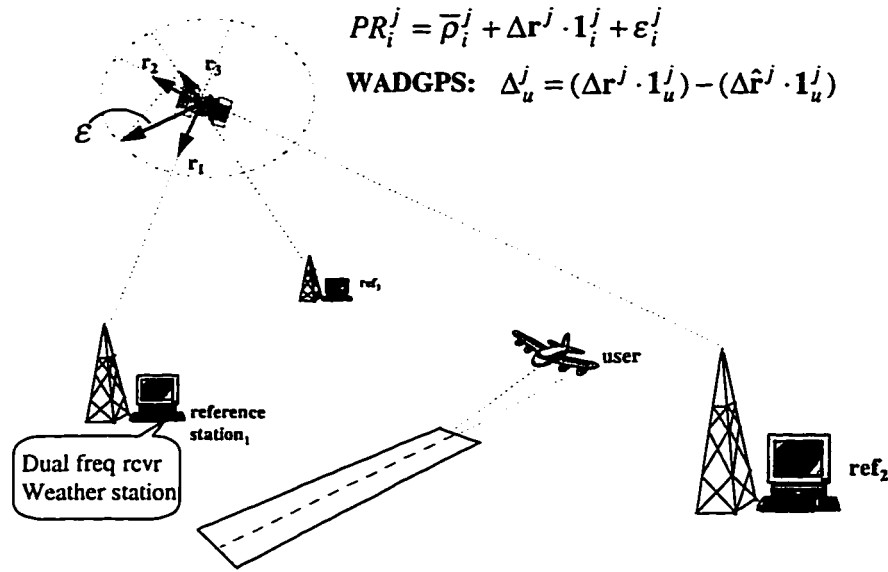


**Figure 2.1.2 Wide Area Differential GPS**

The same notations are used as Figure 2.1.1.  $\Delta \hat{r}^j$  is the estimate of satellite location error provided by the wide area reference station network.  $\Delta_u^j$  is the correction residual of WADGPS.

WADGPS use the ionospheric delay estimates to generate corrections for users over the coverage area. Therefore WADGPS can provide a vector of differential corrections for each satellite instead of just LADGPS scalar corrections. Figure 2.1.2 illustrates the WADGPS and its correction to the satellite orbital location error.

The capability of LADGPS and WADGPS to determine the satellite orbital location errors has been simulated, and Figure 2.1.3 illustrates the covariance analysis of this simulation. The figure is based on the covariance analysis in Appendix B [Enge, 1992]. Each case assumed the use of three reference stations at identical locations. From the figure, we can clearly see the benefits of the WADGPS technique. WADGPS can provide very good corrections for the orbital error for a very large geographical area without significant degradation, which is the main drawback of LADGPS.

The LADGPS nevertheless plays a very important role in highly accurate Category III landings which require better than 2-foot vertical guidance. Because of the nearly perfect local error cancellation, LADGPS enables real-time kinematic centimeter level accuracy



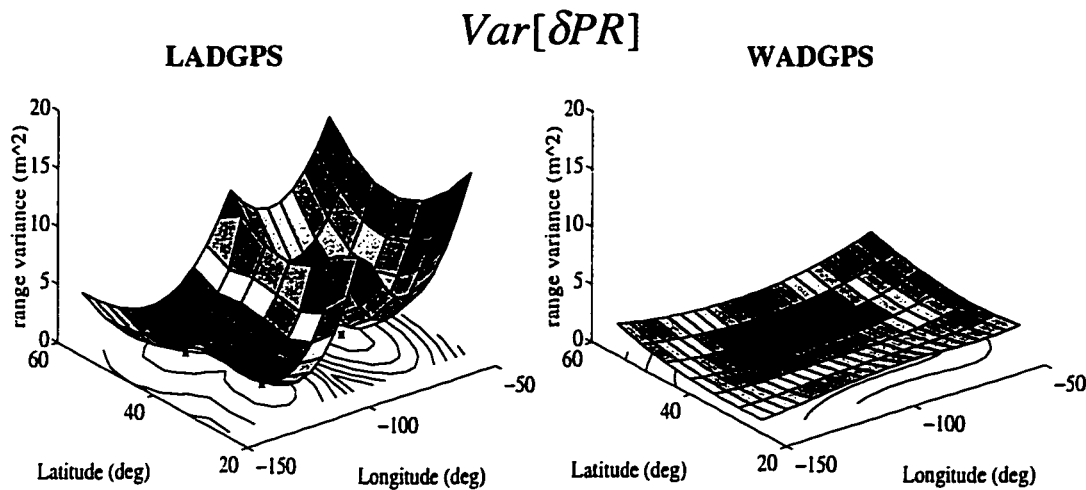


**Figure 2.1.3 Comparison of Error Degradation of LADGPS and WA DGPS**  
The error surfaces are the variances of pseudorange residuals after differential corrections.  
Each case assumed the use of three reference stations at identical locations.

through the carrier-phase measurement. One of the important successes in this development is the Stanford Integrity Beacon Landing System (IBLS) which resolves integer ambiguity in the carrier phase with the aid of pseudolites (pseudo-satellites) and demonstrated high accuracy in more than 100 Boeing 737 auto-landing flight tests [Cohen et al, 1994].

## 2.2 Challenges of Real-Time Implementation

Although the work of Kee on WADGPS [Kee, et al., 1991] and the covariance analysis of Enge and Pullen [Enge et al., 1995, Pullen et al, 1994] have predicted that WAAS will be able to support the stringent vertical accuracy requirement of Category I landings, the question remains as to whether we can demonstrate the same accuracy with real-time data, especially under the 250 bit/sec GEO data rate constraint. This rate constraint arises because of the wide coverage of the GEO footprint and the need to avoid interference with GPS signals (see Chapter 1). Another major challenge of WAAS is the integrity monitoring, that is, how well we can utilize the network information to provide the necessary integrity alerts to the users to guarantee flight safety.

Because of the nature of the ionosphere and because the GPS ionospheric measurements are widely spread, small scale ionospheric disturbances would be

particularly hard to detect. Therefore, the integrity monitoring of the ionospheric corrections is one of the most significant challenges in implementing WAAS.

## 2.3 GPS Signal Modeling

The GPS dual frequency code-phase pseudorange ( $PR$ ) and carrier-phase ( $\phi$ ) observables between  $i^{th}$  receiver and  $j^{th}$  satellite can be modeled as follows [ICD-GPS-200, 1992]:

$$PR_{L1} = \rho_i^j + b_i - B^j + I_{L1,i}^j + T_i^j + T_{gd}^j + M_{PR1} + E_{PR1} \quad (2.3.1)$$

$$PR_{L2} = \rho_i^j + b_i - B^j + \gamma \cdot I_{L1,i}^j + T_i^j + \gamma \cdot T_{gd}^j + R_i + M_{PR2} + E_{PR2} \quad (2.3.2)$$

$$\phi_{L1} = \rho_i^j + b_i - B^j - I_{L1,i}^j + T_i^j + T_{gd}^j + N_1 \lambda_1 + m_{\phi 1} + \varepsilon_{\phi 1} \quad (2.3.3)$$

$$\phi_{L2} = \rho_i^j + b_i - B^j - \gamma \cdot I_{L1,i}^j + T_i^j + \gamma \cdot T_{gd}^j + R_i + N_2 \lambda_2 + m_{\phi 2} + \varepsilon_{\phi 2} \quad (2.3.4)$$

$$\gamma = (L_1/L_2)^2 = (1575.42 / 1227.60)^2 = (77/60)^2 \equiv 1.647 \quad (2.3.5)$$

where the following notations are used:

$\rho_i^j$  is the true geometric distance between the  $j^{th}$  satellite and the  $i^{th}$  receiver,

$b_i$  and  $B^j$  are the receiver and satellite clock biases, respectively (Note that  $B$  also includes the artificial SA),

$I_{L1}$  is the ionospheric delay on GPS L1 frequency,

$T$  is the tropospheric delay,

$T_{gd}$  is the actual (as opposed to the broadcast) transmitter interfrequency bias in code-phase on L1 for the  $j^{th}$  satellite (According to ICD GPS-200, the control segment monitors the satellite timing so that the  $T_{gd}$  will be completely canceled when receivers calculate the ionosphere-free measurements. This is the reason why the satellite interfrequency bias is  $T_{gd}$  at L1 frequency, but  $\gamma \cdot T_{gd}$  at L2 frequency)<sup>1</sup>,

$R_i$  is the receiver differential interfrequency bias on L2 for the  $i^{th}$  receiver. Because the timing of the GPS receivers depends on the L1 C/A code, the differential

---

<sup>1</sup>  $T_{gd}$  and  $R$  are due to the different phase shifts between L1 and L2 in the analog part of the satellites and receivers. They are explained in detail in Chapter 3.

interfrequency bias on L1 is, by definition, zero, which is different from the modeling of satellite's  $T_{gd}$ ,

$N_1\lambda_1$  and  $N_2\lambda_2$  are the integer ambiguities in the carrier-phase observables,  $M_{PR}$  and  $m_\phi$  are the multipath effects in the pseudorange and carrier-phase observables, respectively and  $M_{PR}$  is on the order of several meters with  $M_{PR} \gg m_\phi$ ,  $E_{PR}$  and  $\varepsilon_\phi$  are the receiver measurement noise of pseudorange and carrier-phase observables, respectively and  $E_{PR} \gg \varepsilon_\phi$ .

Note that the ionospheric delays in the GPS L2 measurements are proportional to those in the L1 measurement, i.e.  $\gamma = (L_1/L_2)^2$ . Furthermore, the ionospheric effect on the carrier phase is exactly opposite to the effect on the pseudorange. In other words, the ionosphere creates an advance in the carrier phase but a group delay in the pseudorange. These different effects are usually referred to as the code-carrier divergence in the GPS literature. Detailed discussion and derivation of ionospheric effects are discussed in Chapter 3 and Appendix F. Chapter 3 also treats the combined effect of the interfrequency biases (IFBs),  $T_{gd}^j$  and  $R_i$ , in detail. Also note that since the L2 P-code is encrypted, its code phase measurement can only be obtained from advanced receiver technologies, for example, the cross correlation tracking. The output of the cross correlation is usually the difference between the L2 and L1 code phase pseudoranges [van Dierendonck, 1994].

## 2.4 Stanford WAAS Processing

Figure 2.4.1 shows the overall WAAS data processing procedures at Stanford University. First of all, the raw measurements are transmitted from the Wide Area

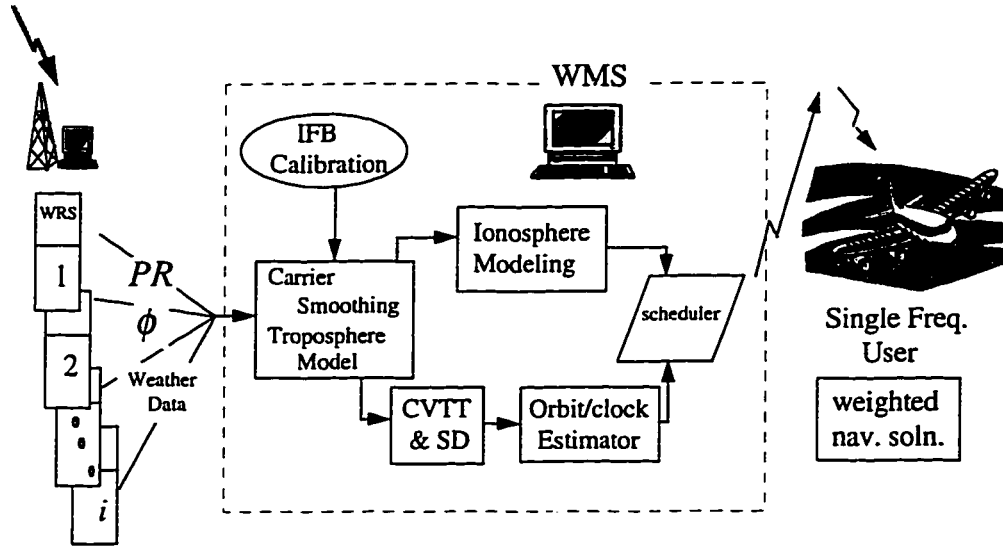


**Figure 2.4.1 Stanford WAAS Data Processing**

Reference Stations (WRSs) to the Wide Area Master Station (WMS) at the Stanford WAAS Laboratory through the network at a one hertz frame rate in real-time. The raw measurements are preprocessed to reduce local errors by carrier-aided smoothing, taking out tropospheric delay, and applying the interfrequency bias calibration. After processing and the reduction of local errors, the WMS estimates satellite clock/location errors and simultaneously models the ionosphere.

All these differential corrections together with information on system integrity are packed into WAAS messages and appropriately scheduled to be radioed to the users. The correction messages of the flight tests in this study were transmitted through ultra-high frequency (UHF) radio modem data links located at airports. Despite the fact that we were not using a geostationary (GEO) satellite, the UHF datalinks still transmitted corrections at the WAAS Minimum Operation Performance Standard (MOPS) specified rate of 250 bps. We studied the effect of having different latency than if we had used a GEO, and found that had negligible effect.

## 2.5 Reducing the Local Errors

In Equations (2.3.1) to (2.3.4), multipath effects and receiver thermal noises are specific to the reference receivers and they corrupt the pseudorange measurements. The

first step in the processing is to mitigate these errors in order to obtain cleaner measurements for the generation of WAAS error corrections. Furthermore, tropospheric delays are not part of WAAS corrections because the troposphere is the lowest layer in the atmosphere and therefore its delays are considered local errors to the users. Therefore, the WMS must use tropospheric delay models to eliminate these errors from its reference measurements as much as possible.

### 2.5.1 Tropospheric Delay Modeling

The tropospheric delay in the GPS microwave frequency range is on the order of several meters. Most of this delay can be modeled quite accurately using temperature, pressure and relative humidity. As shown in the work of Smith and Weintraub [1953] and Hopfield [1971], the delay introduced by the troposphere can be divided into dry (hydrostatic) and wet parts. The dry part makes up about 85-90% of the total delay. This dry delay can be modeled to an accuracy of 1% by deriving it from the perfect gas law with the measurements of surface temperature and pressure. However, the wet delay, caused mainly by water vapor in the air, is usually treated as a stochastic process because of local variations in water vapor content. Currently, only the *average* value of the wet delay can be calculated with surface meteorological measurements, especially relative humidity. The unmodeled part of wet delay needs to be treated as stochastic process [Black, 1978, Black & Eisner, 1984, Janes et al., 1991].

Each WRS has a meteorology station to measure the surface temperature, pressure and relative humidity for calculating the tropospheric delay. The GPS tropospheric delay at any elevation angle can be expressed as

$$T = T_{d,z} \cdot M_d + T_{w,z} \cdot M_w, \quad (2.5.1)$$

where

$T_{d,z}$  is the dry delay in the zenith direction,

$T_{w,z}$  is the wet delay in the zenith direction, and

$M_d$  and  $M_w$  are the mapping functions from the local zenith direction to the LOS direction for dry and wet delays, respectively (both are functions of satellite elevation angle).

The tropospheric model used by Stanford WMS is summarized in Appendix C.

### 2.5.2 Dual-frequency Carrier Smoothing of Pseudoranges and Ionospheric Delays

Since the carrier phase contains much smaller measurement errors than the pseudoranges (both multipath and receiver noise) and contains almost the same information (except ionospheric “advance”), the carrier phase can be used to smooth the pseudorange to reduce the measurement noise. We chose a Hatch filter [Hatch, 1982] with some modification as the smoothing filter because of its simplicity. From our experience, this filter converges faster and is more robust under different multipath situations than the dual-frequency Kalman-filter approach (see, for example, the algorithm proposed by Goad [1992]). Appendix D presents the detail of this smoothing algorithm.

The smoothing filter is implemented using the three ionospheric measurements from the dual-frequency observables. From this approach, the filter has the advantage of detecting and fixing carrier cycle slips more easily because of the slow variation characteristic of the ionosphere. The dual frequency smoothing also avoids the “ionospheric divergence” problem between the pseudorange and carrier phase measurements. As a result, this implementation allows a very long smoothing time constant, and hence better performance.

Using the idealized frequency-dependency relationship (neglecting the interfrequency biases), ionospheric delay measurements can be derived from linear combinations of the GPS L1 and L2 pseudorange and carrier-phase observables:

$$I_{L1,PR} \equiv \frac{PR_{L2} - PR_{L1}}{\gamma - 1} = I_{L1} + v_{PR} \quad (\text{from PRs}) \quad (2.5.2)$$

$$I_{L1,\phi} \equiv \frac{\phi_{L1} - \phi_{L2}}{\gamma - 1} = I_{L1} + Amb + v_{\phi} \quad (\text{from carrier phases), and} \quad (2.5.3)$$

$$I_{L1,L1} \equiv \frac{PR_{L1} - \phi_{L1}}{2} = I_{L1} - \frac{N_1 \lambda_1}{2} + v_{L1} \quad (\text{from L1 PR and carrier phase}) \quad (2.5.4)$$

where  $I_{L1}$  is the ionospheric delay at the L1 frequency; the extra subscripts represent the observables used in the combination;  $Amb$  represents the combination of ambiguities

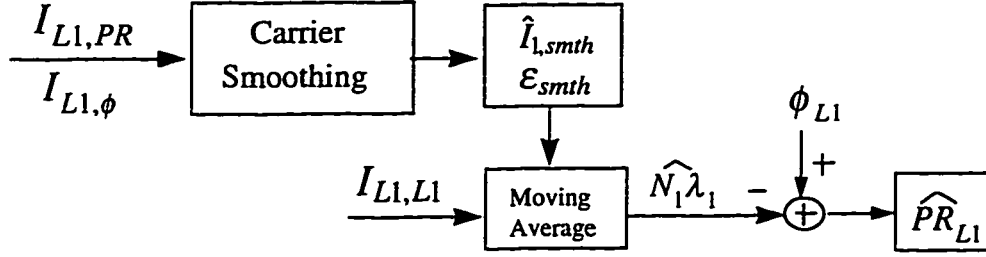


**Figure 2.5.1 Dual-frequency Smoothing of Ionospheric Delays and Pseudoranges**

from the L1 and L2 carrier phases; and the magnitude of noises are  $v_{PR} > v_{L1} > v_{\phi}$ . Note that Chapter 3 and 4 will expand these measurements to include the interfrequency biases and will present error analysis of WAAS ionospheric modeling.

The inputs to the filter are the three ionospheric delay measurements. As shown in Figure 2.5.1, the filter estimates the smoothed ionospheric delay  $\hat{I}_{1,smth}$  and ionospheric-free pseudorange,  $\hat{PR}_{L1}$ . The first step in the implementation is to smooth  $I_{L1,PR}$  by the low-noise  $I_{L1,\phi}$  and produce  $\hat{I}_{1,smth}$  and its confidence. Then combining  $\hat{I}_{1,smth}$  and Equation (2.5.4), we can estimate the constant  $N_1\lambda_1$  by moving average. Finally, substituting  $\hat{I}_{1,smth}$  and  $N_1\lambda_1$  into the L1 carrier phase, Equation (2.3.3), we obtain the estimate of smoothed ionosphere-free pseudorange  $\hat{PR}_{L1}$ . Figure 2.5.2 presents one of the typical smoothing results.

The dual-frequency smoothing technique has two significant advantages over single-frequency smoothing:

- ◆ The ionospheric divergence between code-phase and carrier-phase measurements is completely avoided. Therefore, the smoothing process can employ a long time constant. As the filter converges with time, the multipath problem will be reduced.
- ◆ Cycle slips can be easily detected and patched because of the slow variation of the physical ionosphere. Since the smoothing is performed at 1 Hz data rate and the ionospheric delay variation is very small between measurements, the Stanford WMS simply patches the integer ambiguity if cycle slips occur and increases slightly the smoothing variance. Note that with SA on, the single frequency smoothing is harder to patch the ambiguity.

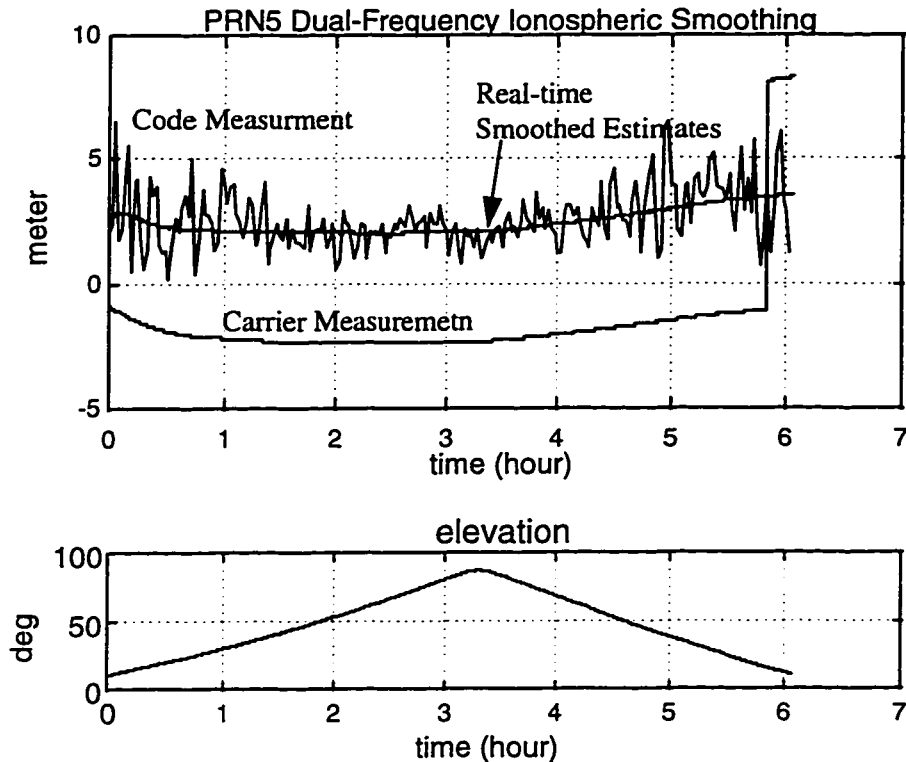


**Figure 2.5.2 Dual-frequency Smoothing Result**

This figure demonstrates the effectiveness of the dual-frequency smoothing: 1) reduction of measurement error 2) very long time constant, and 3) easy handling of cycle slips. After 15 to 20 minutes, the filter converges and the noise level of the smoothed result can be reduced to less than 10-cm. In the upper plot, the carrier measurement is biased and is presented close to zero in order to view easily. The jump of the carrier phase is not an exact integer but are adjusted to fit into the plot to show the existence of cycle slips. The lower plot is the history of satellite elevation angle.

## 2.6 Satellite Location and Clock Corrections

As described before, the corrections of satellite location error and satellite clock bias are main parts of the WAAS. Satellite location errors arise from the errors in the broadcast satellite ephemerides, which are generated by the GPS control segments. The deliberate Selective Availability is the major part of the satellite clock error. There are at least two approaches for providing satellite location corrections: 1) estimate the errors in the broadcast satellite ephemeris over a short time period and 2) estimate the full orbit using dynamic models, including gravity and orbital disturbance forces.

At Stanford's WMS, we chose the first approach for its simplicity of implementation, and we emphasized the integrity monitoring of the satellite orbit correction and the user's



positioning accuracy. As the test results show (Chapter 5), this approach is adequate for positioning accuracy, and substantially reduces programming complexity relative to the dynamic approach.

The Stanford WAAS orbital error determination methodology begins after the local errors are reduced, as described in the previous section. At this point, WMS obtains the so-called ionosphere-free, troposphere-free and smoothed pseudorange:

$$\begin{aligned} PR_{i, \text{smoothed}, \text{iono-free}, \text{trop-free}}^j &= PR_i^j - \hat{I}_{L1,i}^j - \hat{T}_i^j \\ &= \rho_i^j + b_i - B^j + v_i^j \end{aligned}$$

where  $v_i^j$  is the additive noise to account for the residual errors in 1) smoothing, 2) IFB calibration, 3) tropospheric corrections and 4) ionospheric corrections. When expressed in terms of broadcast ephemeris, one can easily see the error,  $\Delta \mathbf{r}^j$ , in the broadcast ephemeris:

$$PR_{i, \text{smoothed}, \text{iono-free}, \text{trop-free}}^j = (\bar{\rho}_i^j + \Delta \mathbf{r}^j \cdot \mathbf{1}_i^j) + b_i - B^j + v_i^j \quad (2.6.1)$$

where  $\bar{\rho}_i^j$  is the range between satellite  $j$  and receiver  $i$  calculated using the broadcast ephemeris. Taking out the range  $\bar{\rho}_i^j$ , we have the *pseudo-range residual* or  $\delta PR$  for each satellite:

$$\delta PR_i^j = b_i - B^j + \Delta \mathbf{r}^j \cdot \mathbf{1}_i^j + v_i^j \quad (2.6.2)$$

This  $\delta PR$  residual, containing the reference station receiver clock bias ( $b$ ), satellite clock bias ( $B$ ) and satellite location 3-dimensional error ( $\Delta \mathbf{r}$ ), is the basic measurement for the satellite orbit and clock estimation. Note that  $\delta PR$  is both satellite and receiver dependent. One approach is to solve for the  $\Delta \mathbf{r}$  and  $B$  in Equation (2.6.1) together with the receiver clock bias,  $b$ . This method is originally used in Kee's implementation and is referred to as the full-vector approach [Kee et al., 1991]. However, this method requires a large matrix inversion since the estimation state vector contains all the parameters from both GPS satellites and WRS receivers. In order to simplify the approach and reduce the complexity for real-time data processing, we invented the following procedures, including

and a single-difference algorithm, and a Common View Time Transfer (CVTT) algorithm to separate the receiver clock biases from the measurement and make it only satellite dependent,. This approach has been awarded a U.S. patent [Enge et al., 1997].

### 2.6.1 Common View Time Transfer

We use the Common View Time Transfer algorithm to remove the reference station receiver biases relative to a master receiver. This procedure is also referred to as “synchronization” of WRS clocks. Note that all the satellite clocks have already been synchronized to GPS time, although we still need to correct for the satellite SA effect (See Section 2.6.3).

Based on the single-difference between the  $i^{th}$  receiver and the master receiver in the network, the  $i^{th}$  receiver clock bias can be estimated and removed from Equation (2.6.2). This process can be written as

$$\begin{aligned}\hat{b}_{i,M} &= b_i - b_M \\ &\approx E[\delta PR_i^j - \delta PR_M^j] = \frac{1}{\sum_{j=1..K} w_{i,M}^j} \sum_{j=1}^K \{(\delta PR_i^j - \delta PR_M^j) \cdot w_{i,M}^j\}\end{aligned}\tag{2.6.3}$$

where  $K$  is the total number of common satellites viewed by both receiver  $i$  and the master receiver,  $w_{i,M}^j = 1/(v_i^{j2} + v_M^{j2})$  is the weighting for the pseudoranges combination, which is dependent on the measurement noises of the pseudorange residuals. The master receiver can be chosen for convenience and is generally the one collocated at the Stanford WAAS Laboratory. Since the projection  $\Delta \mathbf{r}^j \cdot (\mathbf{1}_i^j - \mathbf{1}_M^j)$  is small and the rate of change of ephemeris error is slow, the accuracy of  $\hat{b}_{i,M}$  is better than half a meter. This is referred to as the “snap-shot” solution since it is obtained by an average of data from one point in time.

To prevent jumpiness, the snap-shot estimated  $\hat{b}_{i,M}$  is further smoothed by a kinematic two-state Kalman filter. The process model for step  $k$  is

$$x_{k+1} = Ax_k + Bw_k\tag{2.6.4}$$

where  $x = [b_{i,M}, \dot{b}_{i,M}]^T$ ,  $A = \begin{bmatrix} 1 & 1 \\ 0 & 1 \end{bmatrix}$  for a discrete kinematic model, and  $B = I_{2 \times 2}$ . The process covariance is calculated using  $W = E[ww^T]$ . Since  $\hat{b}_{i,M}$  itself is the difference between two reference station Rubidium clocks, it is very slowly varying and predictable. Therefore, the uncertainty in the rate  $\dot{b}_{i,M}$  (i.e.  $W$ ) can be very small. This smoothing Kalman filter is designed to have a time constant of 200 to 300 sec.

Using the CVTT algorithm, the pseudorange residuals are synchronized to a common master clock and can be expressed as

$$\delta PR_{i,M}^j = \delta PR_i^j - (\hat{b}_{i,M}) = b_M - \underbrace{B^j}_{\text{scalar}} + \underbrace{\Delta \mathbf{r}^j}_{3 \times 1 \text{ vector}} \cdot \mathbf{1}_i^j + v_{i,M}^j \quad (2.6.5)$$

where  $B^j$  is the fast-varying SA error,  $\Delta \mathbf{r}^j$  is the broadcast ephemeris error, and  $v_{i,M}^j$  includes errors from the kinematic model and the error from the projection  $\Delta \mathbf{r}^j \cdot (\mathbf{1}_i^j - \mathbf{1}_M^j)$ . Note that this synchronized pseudorange residual contains only satellite dependent information which makes it easier to estimate the satellite location and clock errors.

## 2.6.2 Single-Difference Snap-shot Satellite Location Determination

The synchronized pseudorange residual, Equation (2.6.5), contains the slowly varying satellite location error ( $\Delta \mathbf{r}$ ) and the satellite clock error ( $B$ ), mainly SA. SA varies at around 20 cm/sec and its WAAS correction is referred to as the fast correction. In contrast, orbital error varies at around 0.1 cm/sec and its WAAS correction is referred to as the slow correction. It is important to separate the fast and slow errors correctly because of the limited WAAS data rate. That is, WMS needs to send the fast corrections every several seconds but can send the slow correction every 2 min to save the scarce data channel capacity.

Solving the satellite location and clock bias using fixed WRSs is an inverted GPS positioning situation; We need four or more WRSs to track a satellite in order to solve for the four unknowns (three location errors and one clock bias) in a least-squares sense. However, the original Stanford West Coast WAAS Testbed had only three WRSs (Chapter 5); a minimum-norm method was used in this underdetermined case (three

measurement equations but four unknowns). Unfortunately, the minimum-norm approach has difficulty separating the slow and fast correction reliably; that is, it mixes the satellite clock error (SA) together with the location errors (see the simulation in Figure 2.6.2). Therefore we developed single-difference pre-processing to circumvent this situation. Note that even in a large network, such as the FAA's National Satellite Testbed, which has more than twenty WRSs, the underdetermined situation still occurs. For example, in a situation of a rising satellites at low elevation tracked by fewer than four WRSs, the minimum-norm solution is still required (to enhance availability, WAAS must correct as many low elevation satellites as possible).

For example, to estimate the errors for satellite  $j$  (which is tracked by WRSs  $i$ ,  $k$  and  $l$ ), two single-differences are formed between WRSs, i.e.,  $i$  and  $k$ , and  $i$  and  $l$ . As shown in Equation (2.6.6), the single difference between  $i$  and  $k$  has the satellite clock error ( $B$ ) completely canceled and WMS can calculate the minimum norm estimate of  $\Delta \mathbf{r}^j$  using this measurement:

$$\Delta PR_{i,k}^j = \delta PR_{i,M}^j - \delta PR_{k,M}^j = \Delta \mathbf{r}^j \cdot (\mathbf{1}_i^j - \mathbf{1}_k^j) + v_{i,k}^j \quad (2.6.6)$$

$$\Delta PR_{i,l}^j = \delta PR_{i,M}^j - \delta PR_{l,M}^j = \Delta \mathbf{r}^j \cdot (\mathbf{1}_i^j - \mathbf{1}_l^j) + v_{i,l}^j \quad (2.6.7)$$

Note that this single-difference pre-processing is necessary for the geometry based approach, both for the snap-shot solution or Kalman filtering, to ensure the separation of the slow and fast correction. As shown in the real-time implementation [Tsai et al., 1995], the single-difference can help the Kalman filter estimation to converge much faster than the Kalman filter alone.

To illustrate the necessity of using this method, I simulated satellite location and clock bias errors and compared the minimum norm solutions with and without the single-difference pre-processing. The simulation contains three Stanford West Coast WAAS Testbed reference stations and a GPS satellite. No measurement noise was added in this simulation. As shown in Figure 2.6.1, the satellite clock bias variation was simulated to be five times as fast as the variation of the location errors. The magnitude of the clock bias was 50 m and the location error had 5 m errors in all three axes (x, y and z). As the estimation results show in Figure 2.6.2 (b), the minimum-norm solution alone generated

estimates with mixed magnitude and frequency in all four parameters. The combined single-difference and minimum-norm solutions gave much more accurate estimates. Therefore, this method is suitable and necessary for the generation of slow and fast corrections in real-time WAAS.

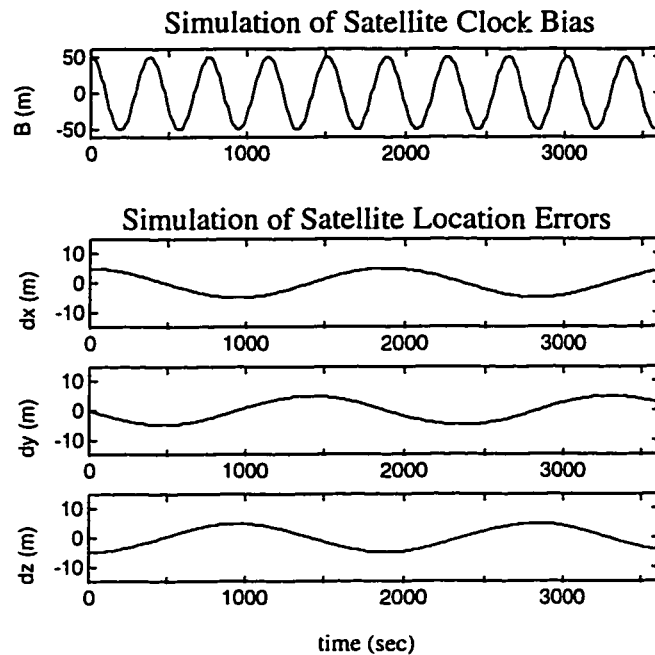


Figure 2.6.1 Simulation of Satellite Fast (SA) and Slow (Location) Errors

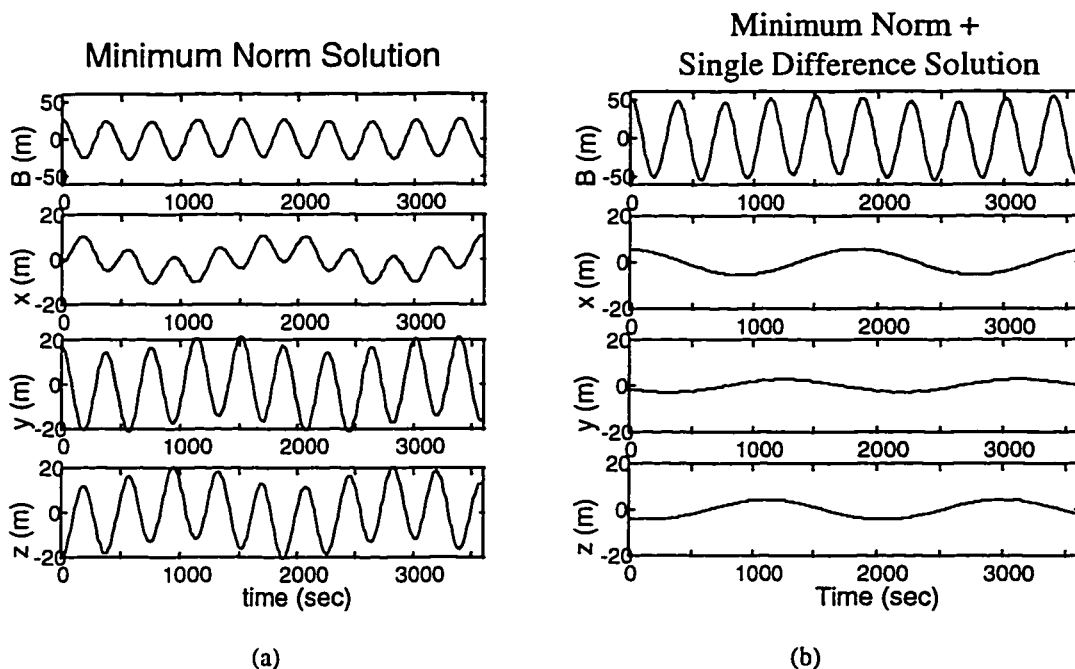


Figure 2.6.2 Separation of Slow/Fast Solutions

### 2.6.3 Satellite Clock Bias Estimation

With the estimates of satellite location errors, the calculation of satellite clock bias ( $B$ ) is straightforward. The location error estimates are inserted into Equation (2.6.5) and averaged over all the WRSs with the  $j^{th}$  satellite in view. That is, the  $j^{th}$  satellite's clock bias is

$$\hat{B}^j - b_M = -E\{\delta PR_{i,M}^j - \Delta \mathbf{r}^j \cdot \mathbf{l}_i^j\}, \text{ or} \quad (2.6.8)$$

$$\hat{B}^j = -E\{(\delta PR_{i,M}^j - \Delta \mathbf{r}^j \cdot \mathbf{l}_i^j) - \hat{b}_M\} \quad (2.6.9)$$

where  $E\{\cdot\}$  is the averaging operator over all the WRSs that observe satellite  $j$ .

Note that even though Equation (2.6.9) has a bias,  $b_M$ , in the satellite clock bias estimate, this bias will not affect the user navigation solution since it is a common bias for all the satellites from the master WRS clock. However, because of the limited numerical range WAAS has in broadcasting the satellite clock error ( $\pm 256$  m), the master clock bias needs to be eliminated to fit in the range of the WAAS fast correction message format.

### 2.6.4 Master Receiver Clock Estimation

The estimation of the master receiver clock bias,  $b_M$ , is a difficult task because all the measurements are contaminated by satellite SAs. Fortunately, the estimate does not require very high accuracy since it is a common bias for all satellites and should not affect the WAAS user position accuracy.

We implemented a combined recursive weighted least squares and moving-average algorithm to perform this estimation, using the broadcast satellite User Range Accuracy (URA) as weights. After about 30 min convergence time, this implementation can result in a better than 5 meter estimate of  $b_M$ . The algorithm is shown in detail in Appendix E.

### 2.6.5 Further Improvement on Satellite Clock/Location Estimation

The estimation of satellite location errors and clock biases can be further improved from this snap-shot solution to more smoothed solutions. Tsai et al. [1995] have incorporated a Kalman filter with a kinematic model in the estimation based on the

algorithm mentioned above, and have demonstrated improved results, especially under conditions of WRS outage and/or satellites at low elevations. For more than four tracking stations, the overdetermined solution is implemented with *a priori* orbital location error information. Research on this topic is still progressing; examples include study on using Hill's equations in the Kalman filter as well as the possible use of the carrier-phase as higher accuracy measurements.

The generation of User Differential Range Error (UDRE), is also an important task in the satellite slow/fast correction. The UDRE is the confidence of the projected satellite clock and location corrections at user's line-of-sight. Since the user employs a weighted navigation algorithm (see section 2.8), UDRE will impact the user's navigation solution.

## 2.7 Ionospheric Corrections

The ionospheric delay observables used by WAAS are derived from the dual-frequency measurements. The details of the generation of the WAAS ionospheric correction model will be discussed in Chapters 3 and 4. This section only briefly describes the model in the WAAS MOPS. The idea is to model the ionosphere using all the dual-frequency measurements from the network. Specifically, the grid model estimates the ionospheric vertical delay at each pre-specified 5-degree or 10-degree latitude and longitude intersections, i.e. grid points. Figure 2.7.1 presents an example of results from this grid model. After receiving this grid-based ionospheric correction, WAAS users will use a pre-specified interpolation algorithm to calculate the appropriate corrections. Finally, users will apply both the satellite clock/orbit and ionospheric corrections to implement the weighted navigation solution.

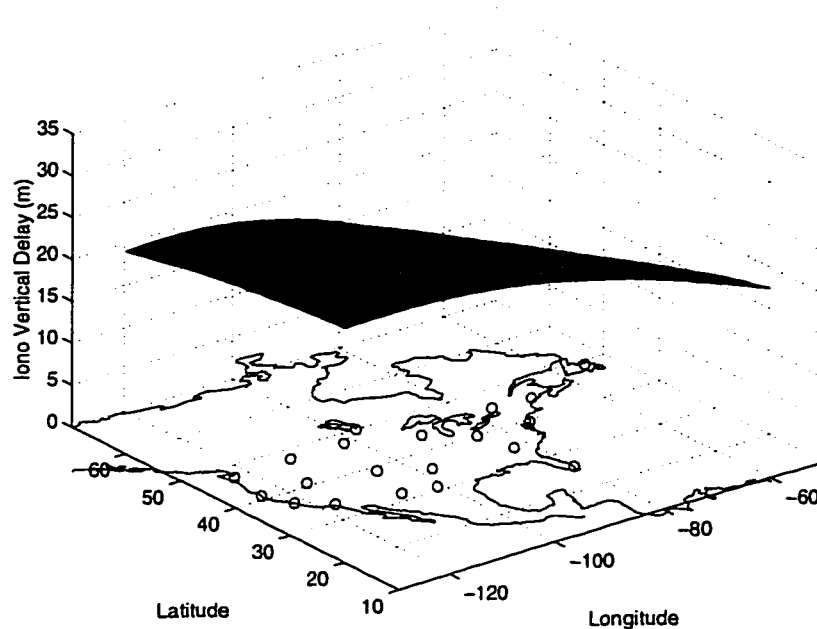


**Figure 2.7.1 WAAS Ionospheric Vertical Delay Grid Model**

The grid model estimates the ionospheric vertical delay at each pre-specified 5-degree or 10-degree latitude and longitude intersections, i.e. grid points.

## 2.8 WAAS Weighted Navigation Solutions

According to the WAAS Minimum Operational Performance Standard for precision approach, WAAS users are required to employ weighted navigation for improving position accuracy. As the WAAS master station tracks each GPS satellite and calculates corrections, it will encounter many situations that need to be taken into account. The master station must generate an estimate of the confidence level for each correction to reflect the most up-to-the-second WAAS network tracking conditions. The weighted navigation algorithm makes use of the confidence number to weight each WAAS correction differently. These master station generated confidences include not only different levels of accuracy of corrections, but also the integrity flag for each correction to deliver integrity warning. The resulting levels in the user's position solutions and the integrity information provide the last level of integrity monitoring in the WAAS.

Examples of conditions that will affect the accuracy of corrections are:

- ◆ A rising satellite may have more smoothing uncertainty than other satellites in view as multipath effects are worse for low elevation satellites.



- ◆ The obliquity factor for converting ionospheric line-of-sight delay observations to vertical measurements has larger modeling errors at lower satellite elevation angles.
- ◆ Cycle slips may interrupt the smoothing process and cause additional errors.
- ◆ The orbit estimation process may not have fully converged when tracking a rising satellite.

The WMS estimation process will yield its error variances along with the filter states. Upon receiving the corrections, the WAAS users will employ the correction error variance to perform a weighted navigation solution. This weighted algorithm allows the system to handle the marginal situations mentioned above more robustly because the weights reflects the qualities of WAAS correction.

The linearized weighted least-squares navigation solution can be expressed as

$$\hat{x} = (G^T W G)^{-1} G^T W y \quad (2.8.1)$$

and the covariance matrix,  $P$ , is

$$P = (G^T W G)^{-1} \quad (2.8.2)$$

where  $x$  is the user position and clock error state vector,  $\hat{x}$  is the least-squares solution of  $x$ ,  $y = Gx + e$  is the linearized observation residual vector,  $G$  is the observation matrix, and  $W$  is the weighting matrix and is the inverse of the measurement covariance matrix or  $R$ .

According to the WAAS MOPS, the master station must generate the 99.9% confidence bounds for the broadcast corrections. Two quantities are used in this document to specify these bounds: User Differential Range Error (UDRE) denotes the bound for satellite location and clock error correction and Grid Ionospheric Vertical Error (GIVE) represents the bound for ionospheric error correction. Note that this requirement has evolved into newer definitions proposed by Walter [Walter et al., 1997]. Basically, both UDRE and GIVE are required to work with the Vertical Protection Level (VPL) equation defined in their study instead of the currently specified 99.9% to protect integrity. All of the corrections and confidences will be included in the WAAS broadcast orbit, clock and ionosphere messages.

The user's differential range error variance,  $\sigma_{range}^2$ , constitutes the diagonal elements of the measurement covariance matrix  $R$  and  $W = R^{-1}$  in Equation (2.8.1). This differential range error is a combination of the WAAS orbit and clock variance ( $\sigma_{UDRE}^2$ ), WAAS ionospheric vertical error variance ( $\sigma_{UIVE}^2$ ), and the user's own local ranging error variance ( $\sigma_{local}^2$ , including receiver multipath effects and thermal noises). That is,

$$\sigma_{range}^2 = \sigma_{UDRE}^2 + (OF \cdot \sigma_{UIVE}^2)^2 + \sigma_{local}^2 \quad \text{meter}^2 \quad (2.8.3)$$

where  $OF$  is the obliquity factor that converts the WAAS ionospheric vertical delay correction at the user's ionosphere pierce point (IPP) to the line-of-sight delay. More details concerning the determination of  $\sigma_{local}^2$  are in Appendix D.

It is possible to meet the requirements that UIVE and UDRE bound 99.9% of errors by simply increasing their values so that they are excessively large. The large confidence limits, however, result in a large  $\sigma_{range}^2$ . This in turn will result in a large position covariance matrix,  $P$  in Equation (2.8.2). Especially for the vertical component, the variance will be more likely to exceed the Category I precision approach accuracy requirement. In this case, the user will not be able to perform the approach with enough confidence if the decision height remains at 200 ft. Thus, this approach generates bounds which are too conservative and can seriously affect the WAAS integrity and availability. For this reason, designing an estimation process that can generate accurate confidence limits of WAAS corrections is one of the most important problems to be studied for WAAS. Furthermore, a Receiver Autonomous Integrity Monitoring (RAIM) specifically designed for the WAAS user's weighted navigation solution is implemented for the final line of defense algorithm [Walter et al., 1995]. Chapter 4 also discusses the detection of an ionospheric local anomaly from real-time measurements as well as ionospheric correction confidences.

## 2.9 WAAS Data Format and Messages

The WAAS MOPS message format divides the wide-area corrections into fast corrections for satellite clock errors, slow corrections for satellite location errors, and grid corrections for ionospheric delays. The data format defined in WAAS MOPS for real-time message broadcast is shown in Figure 2.9.1. The message is limited to 250-bits-long broadcasts at a one second rate. The first 8-bit preamble is used for synchronizing the messages with the GPS time. The last 24-bit cyclic redundant parity check is to validate the message contents. The message body is in the 212-bit data field. The message types that are defined in WAAS MOPS are summarized in Table 2.9.1.

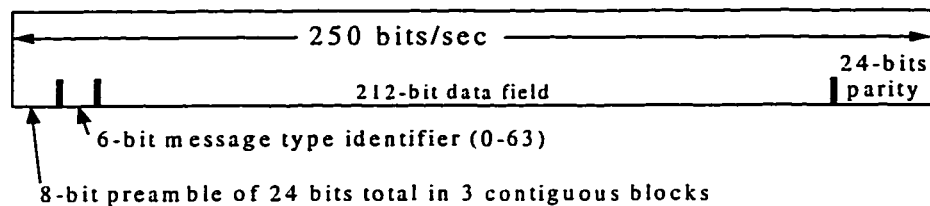


**Figure 2.9.1 Basic WAAS data block format**

Each message is 250 bits long

The most important messages used in Stanford's real-time implementation are

- ◆ **Masks** Type 1 and Types 18-19: a mask is an ordered bit field in which each bit indicates if data is provided for the corresponding satellite. The PRN mask is given in message Type 1. It consists of 210 ordered slots. This Type 1 mask is to designate which satellite belongs to which slot in the message Types 2, 24 and 25 so that the satellite identification need not be sent with every correction message, therefore reducing data traffic. Types 18 and 19 serve a similar purpose: they are used to designate which ionospheric vertical correction in Type 26 belongs to which pre-defined grid point.
- ◆ **Fast and Slow Satellite Corrections** Type 2 and Types 24-25: Type 2 is used to correct the fast variation errors, mostly satellite SA, in the pseudoranges. Each type can transmit 13 fast corrections, which take 16 bits. Type 25 contains the slow variation error components, i.e., the satellite's 3-dimensional location errors (Type 25

can also contain satellite velocity components). Furthermore, to be more efficient, Type 24 is designed to transmit mixed slow/fast data type if there are six or fewer satellites in the PRN mask or if six or fewer satellites remain to fill in Type 2. Note that only corrections for the satellite clock biases themselves are sent; no bias rates are included. The corrections for pseudorange between the messages are calculated by linear extrapolation as part of the user's navigation algorithm, that is,

$$\zeta_{t+\Delta t} = \zeta_t + \Delta t \cdot \dot{\zeta}_t \quad (2.9.1)$$

where  $\zeta_{t+\Delta t}$  is the linear prediction of the pseudorange fast correction at  $t + \Delta t$  using the correction at time  $t$  and its rate,  $\dot{\zeta}_t$ .

From the studies of Chao [1993] and Hegarty [1993], this prediction calculated by the users is satisfactory in short time intervals. The prediction results in tremendous savings in data transmission as the message must be sent out at least once every six seconds.

- ♦ **Ionospheric correction Type 26:** the ionospheric corrections will be broadcast in a discrete pre-defined grid over the area covered by WAAS. The grid size is a 5° square at low and mid latitudes and a 10° square at greater than 55° latitude regions (see Section 4.1.1). Again, no rate correction of the ionosphere is in the message, and users are not expected to do any predicting because the characteristics of the ionosphere vary slowly. However, the WAAS MOPS does specify that four consecutive messages must be sent once WMS detects any fast change or integrity risk in the ionosphere to ensure the timely user integrity alerts.

Note that even though Stanford's WAAS is using a local UHF data link at a much higher rate, 4800 bit/sec, Stanford's WMS uses Type 63, a null message, to fill in the empty slots. This ensures that different messages are broadcast only at the frequency expected for the operational WAAS. That is, the messages conform to the specifications in the MOPS which are listed in Table 2.9.1.

**Table 2.9.1 WAAS Message Types**

Type	Contents	Max. Update Rate	Used at Stanford
0	Do not use GEO for anything	60 sec	No
1	PRN mask assignments	60 sec	Yes
2	Fast pseudorange error estimates	6 sec	Yes
3-8	Reserved for future messages		No
9	GEO navigation message (x, y, z, time, etc.)	100 sec	No
10-11	Reserved for future messages		No
12	WAAS Network/UTC offset parameters	5 min	No
13-16	Reserved for future messages		No
17	GEO satellite almanacs	5 min	No
18-22	Ionospheric pierce point mask 1-5	5 min	Yes (18, 19)
23	UDRE zone radii and weights		No
24	Mixed fast/long-term satellite error estimates	6 or 60 sec	Yes
25	Long-term satellite error estimate	60 sec	Yes
26	Ionospheric delay error estimate	5 min	Yes
27	WAAS Service Message		No
28-62	Reserved for future messages		No
63	Empty message	N/A	Yes

## Chapter 3

# Ionospheric Measurements and Interfrequency Bias Calibrations

The ionosphere is the upper region of the atmosphere where the atmosphere's gas molecules are ionized. This region extends from approximately 60 km to more than 1000 km above the earth's surface. During the day, the sun shines on the ionosphere and causes more molecules to be ionized and therefore increases the free electron density. At night, the ions recombine and the free electron density is lowered.

### 3.1 Ionospheric Measurements

When the GPS signal travels through the ionosphere, it is delayed by the effect of free electrons. The total time delay by the ionosphere in the pseudorange ( $PR$ ) is proportional to the path integral of the free electron density ( $N_e$ ) in the line-of-sight (LOS) direction from the receiver to the satellite. This integral is called Total Electron Content or TEC. The delay is inversely proportional to the carrier frequency squared and can be expressed

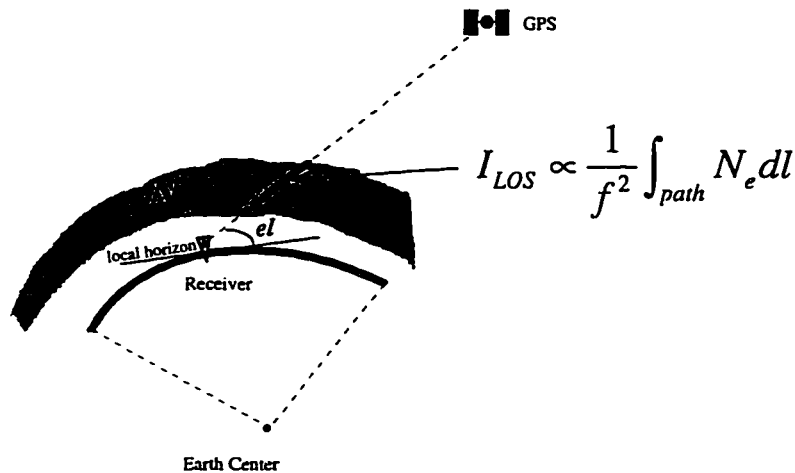


Figure 3.1.1 GPS Ionospheric Line-of-Sight Delay

as

$$I_{LOS} \propto \frac{1}{f^2} \int_{path} N_e(\lambda, \phi, z) dl \quad (3.1.1)$$

where the electron density,  $N_e$ , is a function of longitude ( $\lambda$ ), latitude ( $\phi$ ) and altitude ( $z$ ) above the earth's surface. From electromagnetic theory, the resulting ionospheric delay is given by [Hargreaves, 1992]

$$\Delta t_{iono} = \frac{8.44 \times 10^{-7}}{2\pi \cdot f_{carrier}^2} \times TEC \text{ (seconds), or} \quad (3.1.2)$$

$$I_{LOS} = \Delta t_{iono} \cdot C = \frac{40.3}{f_{L1}^2} \times TEC \text{ (meters)} \quad (3.1.3)$$

where  $f_{L1}$  is the GPS L1 frequency (1575.45 MHz), and  $TEC$  is in units of electrons/m<sup>2</sup>.

The electron density,  $N_e$ , is mainly affected by the activities of the sun and the variation of the geomagnetic field. A daily variation of profiles of  $N_e$  is shown in Figure 3.1.2. These profiles can be demonstrated by using an empirical ionospheric model (the International Reference of Ionosphere from year 1990 (IRI90) [Blitza, 1990] was used for this figure). The profiles show the electron density distribution covers altitudes from 60 to 1000 km at a given latitude of 40° North.  $N_e$  is much higher in the day than at night and reaches its daily maximum between local noon and 2 PM local time primarily due to solar radiation. The centroids of the profiles are also shown, and are about 350 to 400 km.

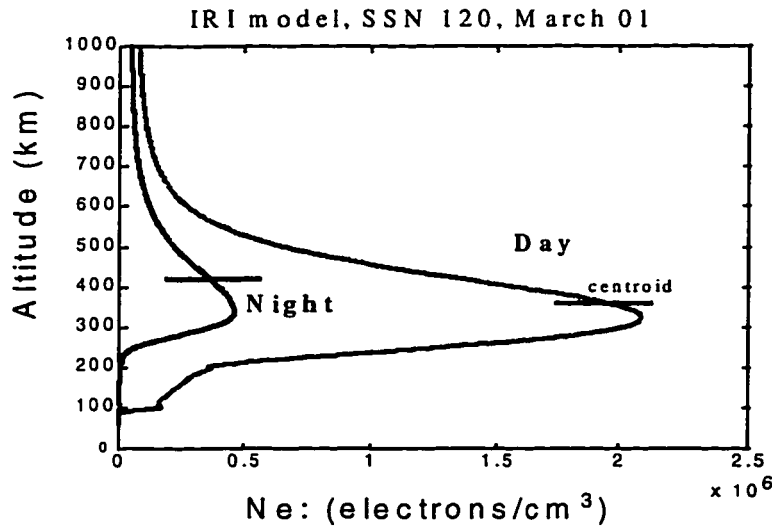
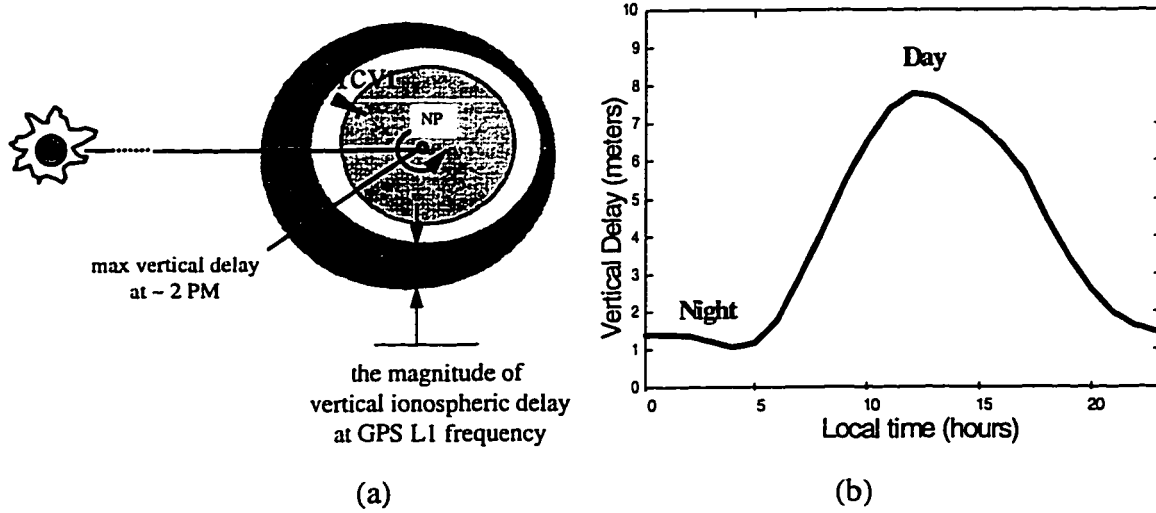


Figure 3.1.2 Ionospheric Free Electron Density Profiles



**Figure 3.1.3 Ionospheric Diurnal Variation at L1**

(a) Illustration of the magnitude of ionospheric vertical delay with the position of the sun relative to the earth (b) Day-night diurnal variation of ionospheric vertical delay. This plot is generated using IRI-90 model with parameters: SSN 120, March 01 and Latitude 40 degrees North.

This diurnal variation of the ionosphere is also clearly shown in the resulting ionospheric delays. Using the profiles of  $N_e$  from the IRI90 model, one can simulate a user who measures the  $90^\circ$  elevation angle LOS ionospheric delays for 24 hours. The delays at GPS L1 frequency can be calculated using Equation 3.1.2 and are shown in Figure 3.1.3.

In the  $PR$  measurement, as in Equation 1.2.1, the ionospheric delay is usually denoted by  $I_i^j$  for the  $i^{th}$  receiver and  $j^{th}$  satellite. Because the delay is inversely proportional to the square of the frequency, the delay of the GPS L2 pseudorange equals a scale factor times that of the GPS L1 frequency  $PR$ . This relation is shown in Equations (3.1.4)-(3.1.6):

$$PR_{L1} = \tilde{\rho} + I_{L1} + \varepsilon_{L1} \quad (3.1.4)$$

$$PR_{L2} = \tilde{\rho} + \gamma \cdot I_{L1} + \varepsilon_{L2}, \text{ and} \quad (3.1.5)$$

$$\gamma = (L1 / L2)^2 = (77 / 60)^2 \cong 1.647 \quad (3.1.6)$$

where  $\tilde{\rho}$  contains the geometrical range, tropospheric delay and other errors.



For most GPS dual-frequency receiver applications, a so-called “ionosphere-free  $PR$ ” measurement is calculated to eliminate the ionospheric delay to at least first order. This measurement is given by

$$PR_{iono-free} = \frac{\gamma \cdot PR_{L1} - PR_{L2}}{\gamma - 1} = \tilde{\rho} + \varepsilon_{iono-free} \quad (3.1.7)$$

Note that  $\varepsilon_{iono-free} = (\gamma \cdot \varepsilon_{L1} - \varepsilon_{L2}) / (\gamma - 1)$  and is roughly three times the error at  $L1$ .

Conversely, for the purpose of observing and modeling the ionosphere, the ionospheric delay can be estimated using dual-frequency  $PR$ s by the following calculation:

$$I_{L1} = \frac{PR_{L2} - PR_{L1}}{\gamma - 1} + \frac{\varepsilon_{L2} - \varepsilon_{L1}}{\gamma - 1} \quad (3.1.8)$$

This ionospheric delay measurement has about twice the error as the basic  $PR$  measurement. WAAS uses a carrier-smoothed version of this measurement as the input for generating the ionospheric corrections.

In addition, the carrier phase will also be affected by the ionosphere. The effect is a so-called “carrier advance,” and it can be shown to be equal but opposite in sign to that experienced by the  $PR$ s. When linearly combined to form the ionospheric measurement, this low-noise measurement is usually used for carrier-aided smoothing of the  $PR$  (A detailed derivation based on first principles of ionospheric delays on code and carrier phase measurements is shown in Appendix F).

### 3.2 Ionospheric Thin Slab Model

The ionospheric measurement in Equation (3.1.8) is the total ionospheric delay in the receiver-satellite LOS direction and is elevation angle dependent. To make the ionospheric measurement independent of the LOS elevation angle, such that it will be more general and convenient to use, a vertical delay model has been proposed for this purpose [Klobuchar, 1986]. In Klobuchar’s work, the ionosphere is modeled as a

condensed thin slab at a 350 km height above the earth's surface. At the intersection of the thin ionosphere shell and the LOS, the slant delay can be converted to the vertical delay using the "obliquity factor" ( $OF$ ). This intersection is denoted as the "Ionospheric Pierce Point" or IPP. The  $OF$  can be derived from the slant-vertical geometric relationship and is a function of elevation angle. Equation 3.2.1 is the formula for  $OF$ :

$$OF = \frac{\text{slant delay}}{\text{vertical delay}} = \sec\left\{\sin^{-1}\left[\frac{R_e}{R_e + h} \cos(el)\right]\right\} \quad (3.2.1)$$

where  $R_e$  is the radius of the Earth ( $=6378.137$  km),  $h$  ( $=350$  km) is the height of the ionosphere layer, and  $el$  is the GPS LOS elevation angle. Figure 3.2.1 shows the concept of the thin slab model and the  $OF$  as a function of the elevation.

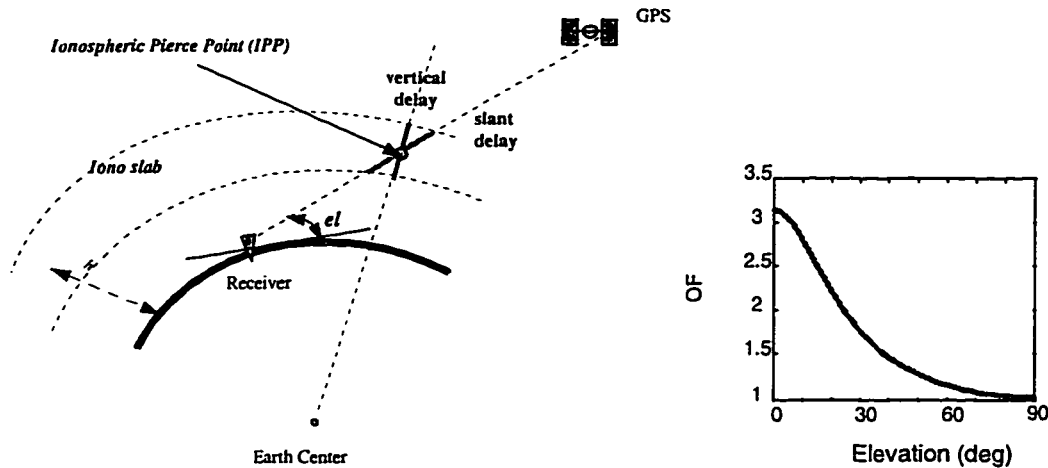


**Figure 3.2.1 Ionospheric Thin Slab Model and Obliquity Factor.**

Currently, GPS is broadcasting the parameters of the Klobuchar model for single-frequency users' ionospheric corrections. This broadcast thin slab model uses eight parameters to describe the spatial and time variation of the ionosphere. It assumes a constant minimum delay at night, and uses a cosine function to represent the delay in the day time. The original paper [Klobuchar, 1986] claims that the model has a 50% reduction of ionospheric rms errors while requiring a minimum of coefficients and user computational time. The implementation of this model and the derivation of the IPP location and  $OF$  are also provided in Appendix F.

### 3.3 Interfrequency Bias Calibration

Until now, we have discussed only the ideal slant ionospheric delay measurements. In a real receiver using dual-frequency *PR*-derived measurements, one needs to consider multipath effects and receiver thermal noise errors. The dual-frequency carrier-smoothing algorithm in Chapter 2 and Appendix D can mitigate these errors to better than 10 cm after 15 to 20 minutes. This filter, in particular, avoids the pseudorange and carrier-phase “divergence” problem and can employ a long smoothing time constant.

Furthermore, there is another error in the slant delay measurement, which is caused by the difference between the frequency response of filtering the GPS L1 and L2 signals. The different frequency response results in a time-misalignment of the L1 and L2 *PR*s and can be treated as a measurement systematic bias. The interfrequency biases existing in both the satellites and the receivers are labeled  $T_{gd}$  and  $R$ , respectively. Figure 3.3.1 illustrates possible sources of the interfrequency biases and the symbols used in this study.

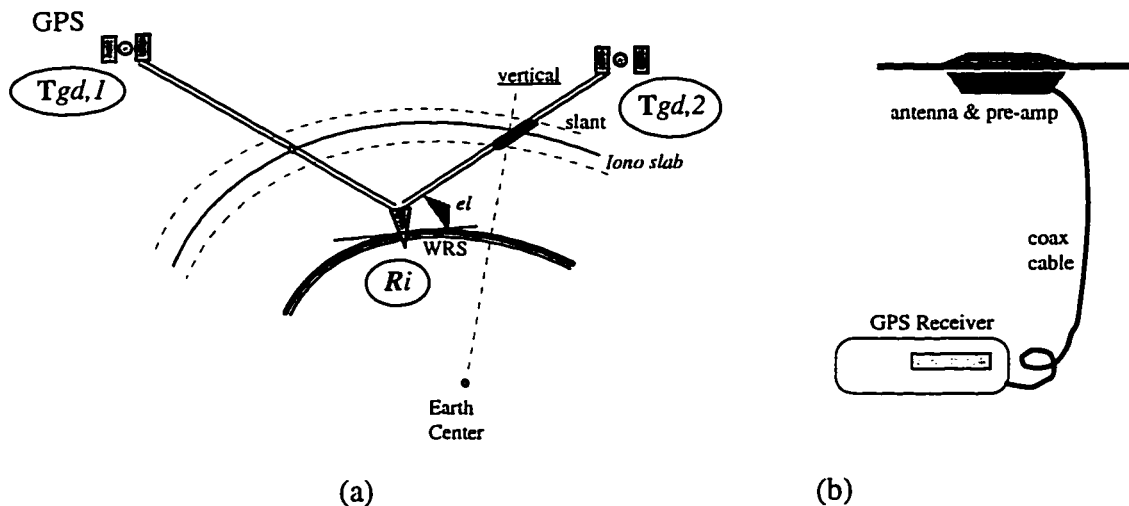


**Figure 3.3.1 Interfrequency Bias Nomenclature and Sources**

(a) The  $T_{gd}$ 's are from the satellites and are satellite dependent (indicated by subscripts 1 and 2). The  $R$ 's are from the receivers and different receivers have their own biases (indicated by subscript  $i$ ). (b) Possible sources of interfrequency biases include the antennas, cables and filters used in GPS satellites and receivers.

Using these symbols, the GPS measurement equations can be re-written as follows:

$$PR_{L1,i}^j = \tilde{\rho} + I_{L1} + T_{gd}^j + M_{PR1} + E_{PR1} \quad (3.3.1)$$

$$PR_{L2,i}^j = \tilde{\rho} + \gamma \cdot I_{L1} + \gamma \cdot T_{gd}^j + R_i + M_{PR2} + E_{PR2} \quad (3.3.2)$$

$$\phi_{L1,i}^j = \tilde{\rho} - I_{L1} + T_{gd}^j + N_1 \lambda_1 + m_{\phi 1} + \varepsilon_{\phi 1} \quad (3.3.3)$$

$$\phi_{L2,i}^j = \tilde{\rho} - \gamma \cdot I_{L1} + \gamma \cdot T_{gd}^j + R_i + N_2 \lambda_2 + m_{\phi 2} + \varepsilon_{\phi 2} \quad (3.3.4)$$

where

$\tilde{\rho}$  is the pseudorange, including tropospheric delay, receiver and satellite clock bias and all other elements common to all four observables in Equations (3.3.1) - (3.3.4),

$N_1 \lambda_1$  and  $N_2 \lambda_2$  are the integer ambiguities in the carrier-phase observables,

$T_{gd}^j$  is the actual (as opposed to the broadcast) transmitter interfrequency bias in code-phase on L1 for the  $j^{th}$  satellite (According to ICD GPS-200, the control segment monitors the satellite timing so that the  $T_{gd}$  will be completely canceled when receivers calculate the ionosphere-free measurements. This is the reason why the satellite interfrequency bias is  $T_{gd}$  at L1 frequency, but  $\gamma \cdot T_{gd}$  at L2 frequency),

$R_i$  is the receiver differential interfrequency bias on L2 for the  $i^{th}$  receiver. Because the timing of the GPS receivers depends on the L1 C/A code, the interfrequency bias on L1 is, by definition, zero. This is different from the modeling of satellite's  $T_{gd}$ ,

$M_{PR}$  and  $m_{\phi}$  are the multipath effects and  $E_{PR}$  and  $\varepsilon_{\phi}$  are the receiver measurement noise in the pseudorange and carrier-phase observables, respectively. Note that

$M_{PR} \gg m_{\phi}$  and  $E_{PR} \gg \varepsilon_{\phi}$ , and

$$\gamma \equiv (L1 / L2)^2 = (77 / 60)^2.$$

From the above measurements, the ionospheric slant measurements at L1 frequency can be calculated as

$$I_{L1,PR} \equiv \frac{PR_{L2} - PR_{L1}}{\gamma - 1} = I_{L1} + (T_{gd}^j + \frac{R_i}{\gamma - 1}) + v_{PR} \quad (3.3.5)$$

$$I_{L1,\phi} \equiv \frac{\phi_{L1} - \phi_{L2}}{\gamma - 1} = I_{L1} + Amb + v_{\phi} \quad (3.3.6)$$

$$I_{L1,L1} \equiv \frac{PR_{L1} - \phi_{L1}}{2} = I_{L1} - \frac{N_1 \lambda_1}{2} + v_{L1} \quad (3.3.7)$$

where  $I_{L1}$  is the ionospheric delay at L1 frequency, the extra subscripts in each equation represent the different measurements used in the combination,  $Amb$  represents the combination of ambiguities from the L1 and L2 carrier phases. Note that each of the measurements suffers from different biases. Because of the biases,  $T_{gd}^j + R_i / (\gamma - 1)$ , and the large noise in the  $I_{L1,PR}$ , it is necessary to calibrate and carrier-smooth the measurements before converting them into vertical measurements to generate the WAAS ionospheric model

For our purpose, the combined bias is defined and will be referred to in the following discussion as

$$\text{Interfrequency Bias or } IFB_i^j \equiv T_{gd}^j + \frac{R_i}{\gamma - 1} \quad (3.3.8)$$

Using this definition, Equation (3.3.5) becomes

$$I_{L1,PR} \equiv \frac{PR_{L2} - PR_{L1}}{\gamma - 1} = I_{L1} + IFB_i^j + v_{PR} \quad (3.3.9)$$

That is, the  $PR$ -derived ionospheric delay has a bias that is a combination of interfrequency biases from satellite  $T_{gd}$  and receiver  $R$ . Note that the  $T_{gd}$ 's are satellite dependent and the  $R$ 's are receiver dependent. In other words, each receiver and each satellite in the WAAS network has a unique interfrequency bias. This large number of unknowns certainly adds more complexity to the measurement calibration process.

These biased ionospheric measurements will not only degrade accuracy of WAAS corrections but will also stress the WAAS ionosphere integrity monitoring (Chapter 4 presents the breakdown of ionospheric error sources). The following sections describe a software algorithm that reduces the systematic IFB errors and achieves the measurement accuracy necessary for implementing the integrity monitoring.

### 3.4 IFB Estimation Methodology

In Equation 3.3.9, both the IFB and the ionospheric delay are assumed to vary quite slowly and are therefore very hard to separate directly. The approach used in this study is to create a model for the ionospheric vertical delay. From the variation of the obliquity factor over time, the IFBs will become observable.

The idea of this methodology is presented in Figure 3.4.1 and a summary follows while detailed description of the algorithm is contained in Appendix G. This use of elevation-dependent variation was first explored by Cohen for estimating the ionosphere from the carrier phase measurements [Cohen et al., 1992].

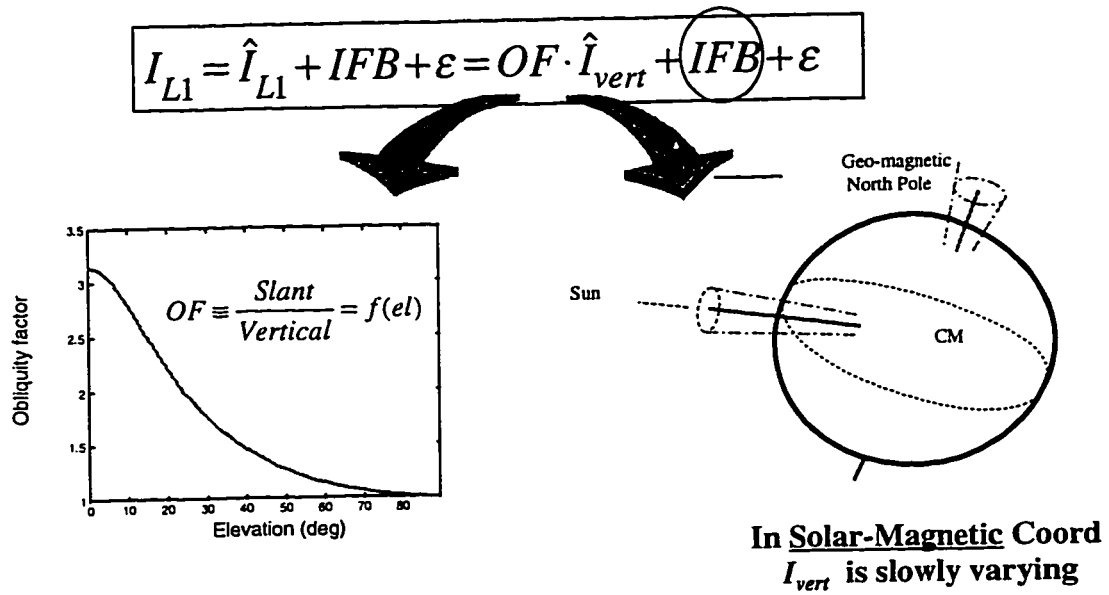


Figure 3.4.1 IFB Estimation Methodology

Since the solar and the geomagnetic field activities dominate the states of the ionosphere, we can model very well the ionospheric vertical delay in the so-called solar-magnetic frame [Jursa, 1985] (Appendix G). In the implementation, the ionospheric vertical delay is modeled and expanded by spherical harmonics, i.e.

$$\hat{I}_{vert} = \sum_{n=0}^2 \sum_{m=0}^n \{C_{nm} \cos(m\lambda) + S_{nm} \sin(m\lambda)\} P_{nm}(\sin(\phi)) \quad (3.4.1)$$

The system and measurement equations in discrete state space are

$$x_{k+1} = F x_k + w_k, \text{ and} \quad (3.4.2)$$

$$z_k = H x_k + v_k \quad (3.4.3)$$

where  $x_k$  is the state vector with  $n$  elements. The state vector comprises the spherical

harmonic coefficients, the IFBs of the master receiver  $T_{gd}^j + \frac{R_M}{\gamma-1}; j = 1 \dots SV$ , and the

IFBs of the reference receivers relative to the master receiver  $\frac{R_i - R_M}{\gamma-1}; i = 1 \dots TRS-1$  or

$$x_k = \left[ \text{spherical harmonics coeff.} \mid T_{gd}^j + \frac{R_M}{\gamma-1}; j = 1 \dots SV \mid \frac{R_i - R_M}{\gamma-1}; i = 1 \dots TRS-1 \right]^T$$

For the slowly varying ionosphere, the system is modeled as a random walk process, i.e.,

$F = I_{n \times n}$ . Since the maximal variation rate of the ionospheric vertical delay variation is

less than 0.2 m per 2 min [Klobuchar et al., 1993, Sardon, 1992], the process noise is:

$$Q = E[w^2] \cdot \Delta t = \left(\frac{0.2}{120}\right)^2 \cdot 120 = 3.3 \times 10^{-4} \text{ (m}^2\text{/sec)} \quad (3.4.3)$$

The model of measurement is  $y = I_{slant}$  and

$$H = [OF \cdot (Model) \mid 0 \dots 0 \overset{j^{th}}{\underbrace{1}} \mid 0 \dots 0 \mid 0 \dots 0 \overset{i^{th}}{\underbrace{1}} \mid 0 \dots 0] \quad (3.4.4)$$

$\underbrace{T_{gd}^j + \frac{R_M}{\gamma-1}} \qquad \underbrace{\frac{R_i - R_M}{\gamma-1}}$

Because of the large number of unknowns that need to be estimated, a Square Root

Information Filter (SRIF) is used to ensure the numerical stability [Bierman, 1977].

Appendix G presents the details of this IFB estimation algorithm.

Figure 3.4.2a shows an example of the IPP ground track and Figure 3.4.2b presents one of the estimation results of the ionospheric spherical harmonics model. Figure 3.4.3 compares the Stanford WAAS Testbed navigation vertical accuracy with and without IFB calibration. Clearly, both the average and the distribution of the vertical positioning error have been improved.

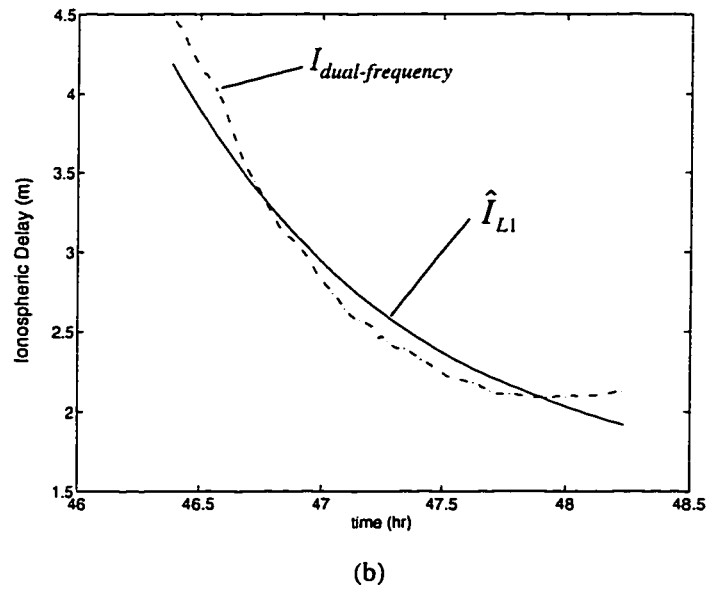
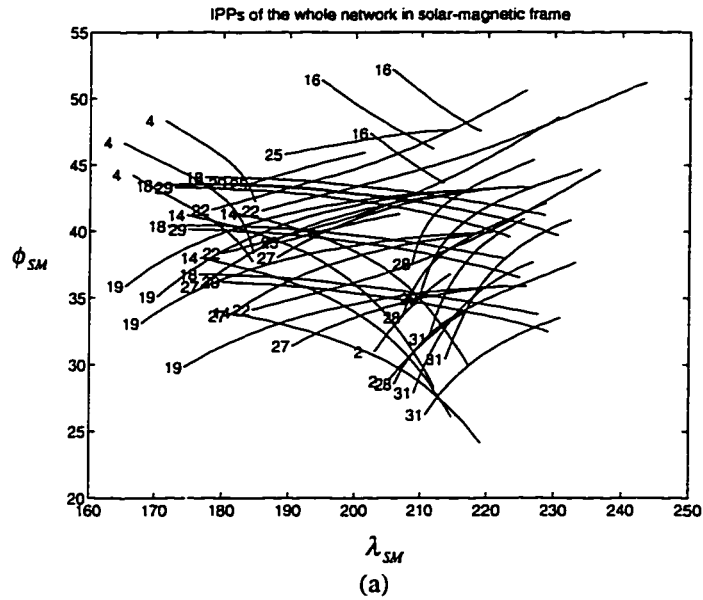
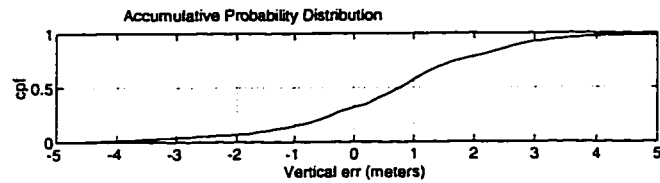
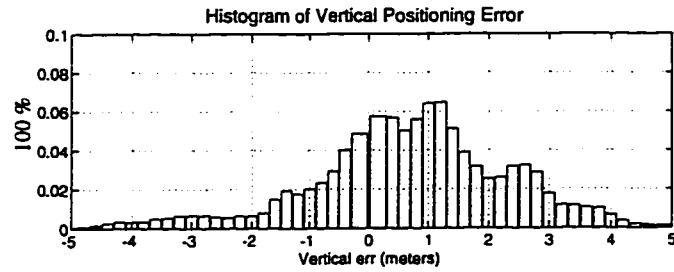


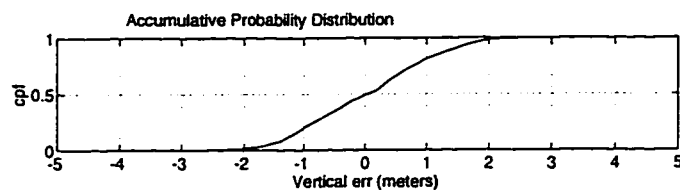
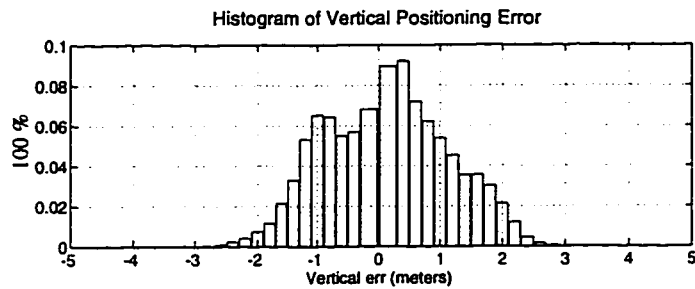
**Figure 3.4.2 Stanford Testbed IPP Distribution and IFB Estimation Results**

Part (a) shows the ground tracks of ionospheric pierce points in the solar-magnetic frame ( $\lambda_{SM}, \phi_{SM}$ ). A total of 43 satellite-receiver pairs from the four original Stanford West Coast Testbed receivers have been included in this run. Part (b) is an example of the comparison of the spherical harmonics expanded ionospheric delay  $\hat{I}_{L1}$  (solid) and dual-frequency measurement (dotted) with adjusted interfrequency bias. The fact that these two curves agree to the 30 cm level most of the time is a good demonstration of the self consistency of this estimation scheme. Note that because the second order spherical harmonic is a relatively smooth function, it can model the large scale behavior of the ionosphere but cannot follow the small variation, as shown in part (b).





(a) before IFB calibration



(b) after IFB calibration

**Figure 3.4.3 Effect of IFB on WAAS Navigation Errors**

Comparisons are made between navigation errors (a) before and (b) after the estimated inter-frequency biases are adjusted. According to these histograms, the IFB calibration not only improved the mean of the error distribution, but also reduced the distribution of the errors, especially with regard to the distribution of the tails at the two ends. The data has total of 50287 samples from 14-hour real-time data collection.

Table 3.4.1 summarizes the estimated results of relative receiver biases in the Stanford WAAS Testbed. The improvements in the position are shown in Table 3.4.2 in terms of 95 and 99.9 percentiles.

From the accumulated IFB-calibrated navigation test results at Stanford, we can clearly see that 1) IFB calibration developed by the methodology presented is consistent at better than half a meter and 2) IFB calibration not only improves the mean of WAAS navigation errors but also reduces the width of the error distribution by a significant amount. This improvement on the measurement and therefore the navigation solution is very important because it increases the WMS's ability to implement the integrity monitoring efficiently (the latter is discussed in Chapter 4).

$\frac{R_i - R_M}{\gamma - 1}$	mean (m)	std (m)	H/W calibrated values (m)
Arcata - Stanford	1.86	0.44	1.40
Elko - Stanford	5.68	0.49	4.54
San Diego - Stanford	3.09	0.33	3.19

**Table 3.4.1 Statistics of Relative Receiver IFBs in Stanford WAAS Testbed**

Results are from single-differences between receivers of estimated interfrequency biases using common satellites. For comparison, the two-year-old hardware calibration results are also listed in the last column. There are apparent changes in these IFB values (Before being shipped to the Stanford WAAS Laboratory, the receivers are calibrated against a precalibrated Turborogue receiver at the laboratory of Stanford Telecommunication)

Percentile	no IFB correction between		with IFB correction between	
95%	-4.7 m	6.7 m	-1.85 m	2.4 m
99.9%	-5.0 m	7.2 m	-2.8 m	2.8 m

**Table 3.4.2 95% and 99.9% of the Stanford WAAS Vertical Error**

Comparison of the errors with and without IFB calibration. IFB calibration reduced the width of the error distribution by more than a factor of two. The statistics are based on a 14-hour data run on August 26, 1995, 54000 epochs.

### 3.5 Temperature Dependence of the IFBs

Before being shipped to the Stanford WAAS Laboratory, the receivers are calibrated against a precalibrated Turborogue receiver at the laboratory of Stanford

Telecommunication. When we first began to develop the Stanford WAAS algorithms, these IFBs needed to be calibrated at most every month. However, as we gained experience with the data and improved the data processing and estimation procedures, we noticed a gap between the IFB estimation results obtained using daytime data and nighttime data. The differences observed were on the order of 30 to 50 cm.

An example of the difference is shown in Figure 3.5.1. When presenting this phenomenon to receiver engineers at Trimble Navigation Ltd., we conjectured that it was due to the ambient temperature variation of the receivers and antennas and resulting electronics and bandpass filter variations. Since the receivers process GPS signals at a lower radio frequency (after down conversion), the IFB contributed by the receiver's frequency response is more sensitive to temperature changes than that from antenna and pre-amplifier.

To verify this conjecture, I deliberately heated up the Stanford Trimble receiver by about 30° F and collected data for estimation. The result is shown in Figure 3.5.2. The relative receiver IFBs changed by about 60 cm and the Stanford master IFBs (including satellite  $T_{gd}$ ) also changed by the same amount for different satellites. For comparison, the day-night temperature change in Figure 3.5.1 is about 13°C or 23°F, and the IFBs changed about 30 to 50 cm. This experiment confirmed that the IFBs are temperature dependent and need to be monitored more carefully and frequently since none of the

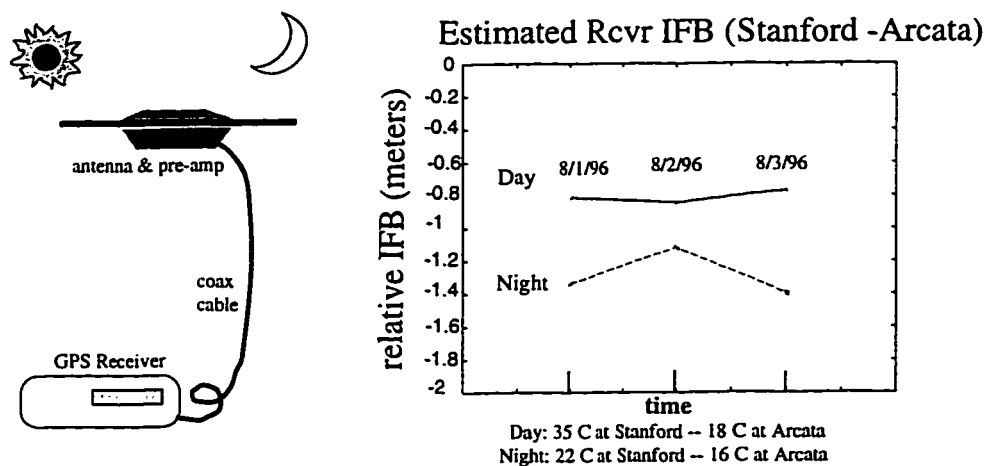


**Figure 3.5.1 Temperature Dependency of IFBs**

This figure shows the variation of relative IFB between Stanford and Arcata receivers due to different temperatures of day and night.

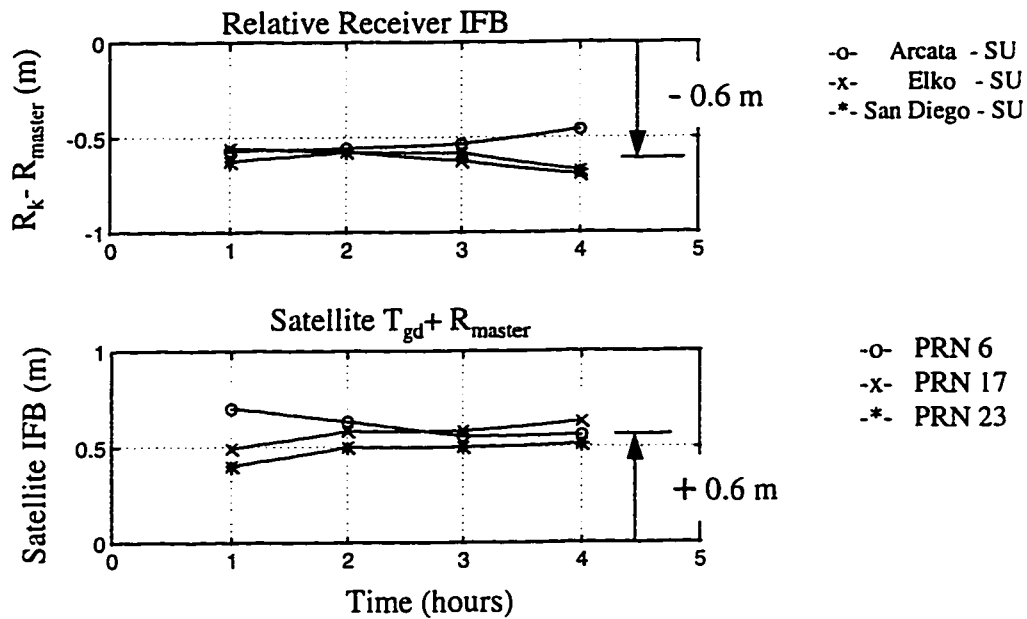


**Figure 3.5.2 Estimation Results of IFB Temperature Dependence Experiment**

The upper plot shows the change of relative receiver IFBs and the lower plot shows the combined satellite and master receiver IFBs. The fact that they change by almost the same amount, 60 cm, but in opposite directions confirmed the temperature dependence of the IFBs.

receivers in the National Satellite Testbed network are in a temperature-controlled environment.

Therefore, it is desirable to estimate the IFBs along with the WMS processing to track their variation. Currently, we are investigating the efficiency of estimating the IFBs in real time. Section 4 in Appendix G presents the current IFB estimation program. Currently, the program is integrated into the TMS project and is under test to estimate the IFBs as the main program progress.

### 3.6 Difficulty in Estimating the IFBs with Assumed Slab Height

The approach of estimating the IFBs presented in this chapter is to my knowledge the only existing way of implementing software calibrations. This approach uses the variation of obliquity factor to separate the IFBs from a modeled ionospheric vertical delay. Even though the results of this estimation are promising, it still has an intrinsic difficulty: the vertical delay model itself. While this model greatly reduces the

calculation complexity, it also introduces modeling errors, especially errors related to the obliquity factor conversion and the assumption of the ionospheric slab's position at a fixed height of 350 km above the earth's surface.

This height of 350 km in the GPS single-frequency ionosphere model has been widely used as a constant. However, an empirical ionosphere model, such as IRI90 mentioned earlier, posits that the mean height is actually varying daily and is dependent on the latitude and sun spot number, etc. [Komjathy et al., 1996]. The 24 hour mean-height variation derived from the IRI model for an SSN of 30 is shown in Figure 3.6.1.

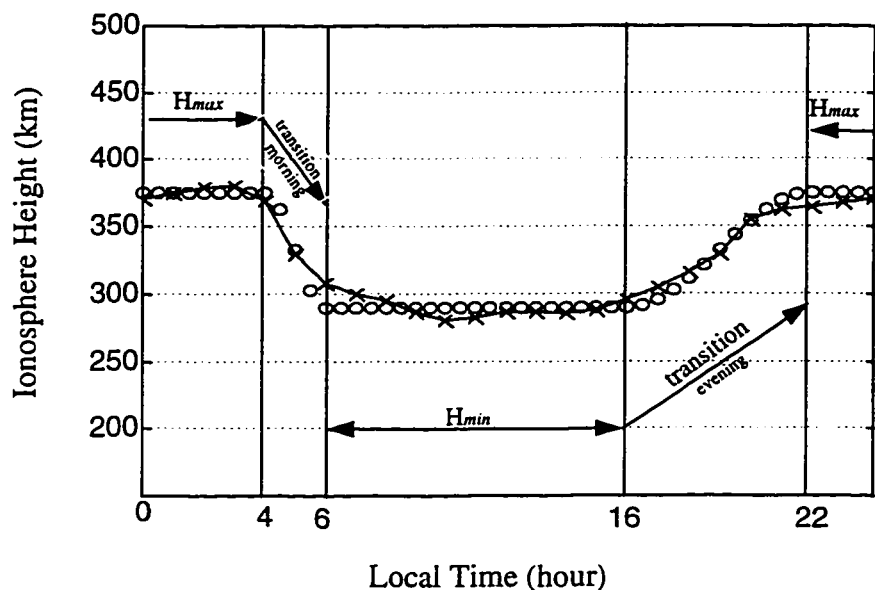


**Figure 3.6.1 Ionospheric Mean Height Variation**

The curve is generated from the IRI 90 model for July 1st, latitude  $40^\circ$ , longitude  $270^\circ$ , SSN 30. The circles form four piecewise-continuous curves to approximate the variation. The maximal height is 430 km for this plot from 10 PM to 4 AM local time. The minimal height is about 290 km from 6 AM to 4 PM local time. The transition in the morning is modeled as a two-hour interval and is faster than that of the evening, six hours, since the excitation of the ionosphere by the sun occurs faster and the recombination of ions is usually slower.

The mean height is higher at night and lower in the day and the transition is fastest in the morning, when the sun first hits on the ionosphere. In the evening, the transition is slower as the ions gradually recombines. This curve can be easily modeled by four piecewise-continuous curves, i.e., constant heights for day and night and two sinusoidal curves for the transition intervals as shown in the same figure.

Originally, we hoped that this modeling would improve the estimation of the IFBs since it can affect both the calculation of the obliquity factor and the location of the IPPs. However, when this height variation was incorporated in the IFB estimation, no apparent improvement was observed. This might be due to other errors introduced by the simplification of the slab model. An attempt to model the ionosphere as three layers, that with 25% of the ionosphere at 200 km height, 50% at 350 km and 25% at 500 km, has also been tried. Again, no apparent improvement was observed.

There is certainly an accuracy limit in this 2-dimensional model for the ionosphere. Further improvement of modeling accuracy may have to employ 3-D modeling techniques, such as real-time ionosphere tomography [Raymund et al., 1990, Hansen, 1996, Howe, 1997].

## Chapter 4

# Modeling and Integrity Monitoring of the Ionospheric Grid Model

**T**he WAAS ionospheric grid model is one of the most important aspects of WAAS in terms of both accuracy and integrity monitoring. In the coming solar maximum around the year 2000, the ionosphere is expected to be more active than it currently is, and this activity will probably introduce both larger pseudorange (*PR*) errors and more disturbances. This chapter describes the approaches for the estimator design and the integrity monitoring schemes that we developed for the Stanford WAAS real-time implementation.

### 4.1 WAAS Ionospheric Vertical Delay Grid Model

One of the tasks of WAAS is to use all of the vertical delays from ionosphere pierce points (IPPs) to form an ionospheric model for the wide area corrections. The MITRE Corp. proposed a grid model for generating WAAS ionospheric corrections so that the parameters of the model can be sent to users for wide area ionospheric correction. The format of this model has been adopted by the WAAS Minimum Operation Performance Standard (MOPS) for real-time applications.

One benefit of this grid-type implementation is that the wide area master station (WMS), using a pre-defined grid, needs only to send out alerts quickly and efficiently for the grid points related to the region affected by ionospheric disturbances while keeping other parts in the WAAS coverage working normally.

#### 4.1.1 Grid Model Implementation

Figure 4.1.1 shows this grid model pictorially. First of all, the WMS will convert all the ionospheric slant measurements to the vertical delays at IPP locations from the reference station network by using the obliquity factors ( $OF_r$ ). The resulting vertical delays are indicated as small circles in the figure.

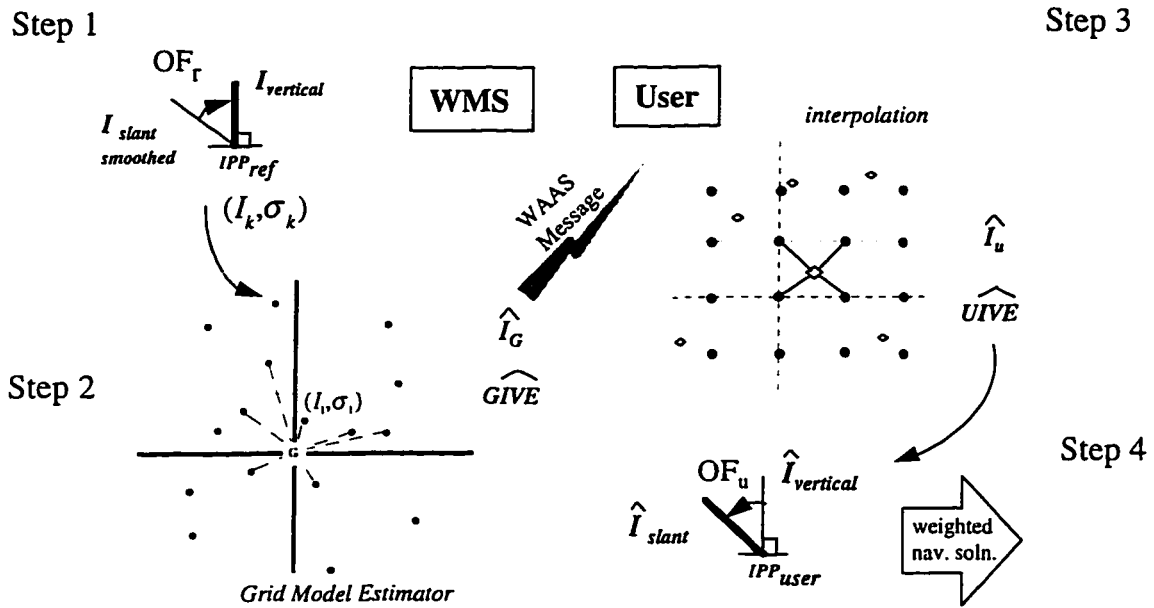


Figure 4.1.1 Data Flow of WAAS Ionospheric Vertical Delay Grid Model

The next and most important step is to create a vertical delay model from all the IPP measurements to estimate the ionospheric vertical delay ( $\hat{I}_G$ ) and its confidence, the Grid Ionospheric Vertical Error or GIVE, for each grid point. These grid points are predefined in the WAAS MOPS and are at  $5^\circ$  or  $10^\circ$  latitude and longitude intersections. The main difficulty of designing this estimator is that all the measurements are spatially scattered. It will therefore be challenging to determine the confidence level of the estimation, particularly during the occurrence of ionospheric disturbances.

Meanwhile the WAAS users will also calculate their IPP locations. After the whole grid model has been broadcast to WAAS users, they will interpolate the grid model for their IPPs' ionospheric vertical delays. This interpolation algorithm is currently



defined in the WAAS MOPS and basically uses the four surrounding grid points to interpolate the IPP between them.

From the interpolation, users obtain the ionospheric vertical delay correction ( $I_u$ ) and the user ionospheric vertical error (UIVE) for every satellite in view. All the vertical delay corrections and confidences will be converted to the slant delays using the user's obliquity factors ( $OF_u$ ) for calculating the final weighted navigation solutions. An example of the grid that covers the continental U.S. is shown in Figure 4.1.2

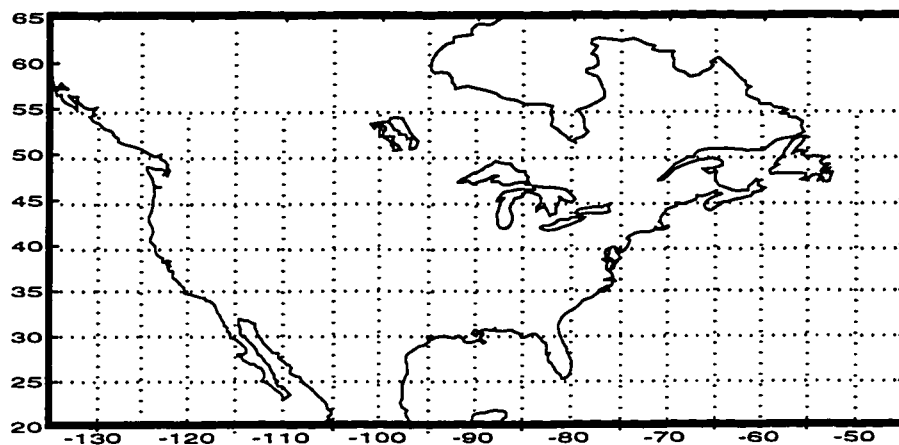


**Figure 4.1.2 WAAS Ionospheric Grid for the Continental U.S.**

#### **4.1.2 Challenges of the WAAS Grid Model**

The challenges of this grid model come from the WAAS requirements and integrity threats in the ionosphere. The initial WAAS system specification requires that the GIVE of each grid point covers 99.9% of ionospheric errors, and is less than 2 meters. In other words, the real-time implementation needs good data processing and estimation design to meet the requirements. Furthermore, a fast-decorrelated ionospheric “bubble” has been speculated as a potential threat to the system accuracy and integrity monitoring [Pullen, et al., 1996].

Such a fast-varying ionosphere may become reality at the turn of this century because of the expected high solar activity during the solar maximum. Therefore, a detection

algorithm for such a disturbance is necessary. For the grid model, WAAS MOPS also provides tools for the integrity warning information. They are:

- ◆ Different levels of confidence for the ionospheric delay estimates, i.e., GIVE.
- ◆ Use/Don't Use flags. They will be raised if the WMS cannot guarantee the accuracy that GIVE predicts (situation arises mainly because of ionospheric disturbances).
- ◆ Not Monitored flags. They will indicate the grid points without enough measurement information or IPPs for generating the estimates.

## 4.2 Grid Model Error Components

The first step in generating the grid model is to analyze the error components in our ionospheric measurements in such a way that we can either eliminate the errors beforehand or include them and propagate them throughout data processing appropriately for generating the estimation confidences.

For the ionospheric vertical delay processing, we have experienced the following error sources:

- ◆ False lock on L2 signals. Because the P-code on L1 and L2 has been replaced by the encrypted Y-code and most of dual-frequency receivers track the signal on L2 using a cross-correlation technique, the signal to noise ratio of L2 tracking is significantly lower than the direct tracking of C/A code on L1. We found that in practice, the process is more likely to experience false lock on L2 signals [Van Dierendonck, 1994]. The results of the false locks can be unreasonable values for  $PR_{L2}$ . These bad measurements can yield incorrect dual-frequency ionospheric measurements and affect all downstream data processing.
- ◆ Multipath effects in the code-measurements and cycle slips in the carrier-phases, which when severe, can lead to poor or biased ionospheric delay estimates. Cycle slips cause problems when a large number of them occur in a short time period and can significantly affect the estimated smoothing variances.
- ◆ L1/L2 interfrequency bias (IFB) estimation errors from the modeling assumptions.

- ◆ **Obliquity conversion errors.** Because of the simplification of assuming an ionospheric thin slab at a mean height of 350 km, the conversion from slant to vertical delay introduces errors. This is largely caused by the gradients in the ionosphere. The larger the gradient is, the greater the error is in the conversion.

A data processing procedure has been developed for the Stanford WMS. First of all, the WMS checks the data consistency using the interfrequency bias calibration results and the information about the maximal ionospheric spatial gradient. Then the WMS propagates the error components using the knowledge obtained from the system error analysis (Section 4.3). Finally, the WMS generates the grid model and its confidence with feedback information to ensure that GIVE covers 99.9% of ionospheric errors statistically. Figure 4.2.1 summarizes this procedure:

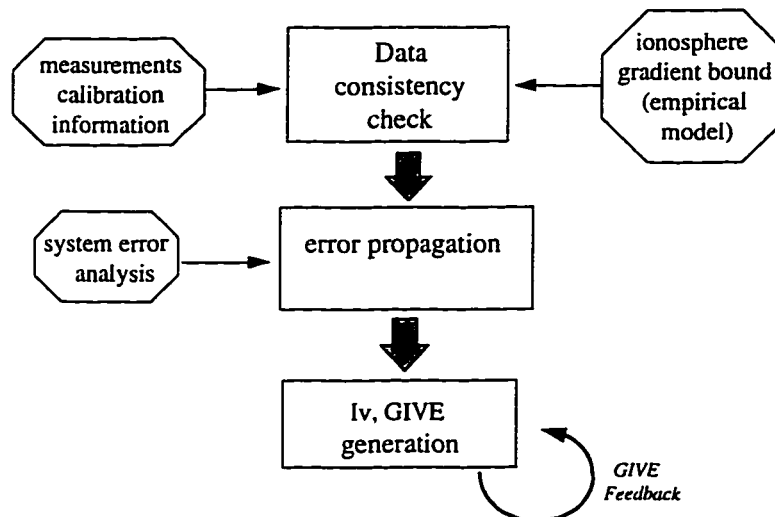


**Figure 4.2.1 Stanford WAAS Grid Model Processing Procedures**

### 4.3 Error Propagation

It is important to have a detailed error analysis in order to understand the problem at hand and perform the best estimation through efficient error propagation. This section details the error analysis mentioned in the previous section and in Figure 4.2.1.

### 4.3.1 Data Screening

To exclude the erroneous data that originated from a possible false lock on L2 or from multipath and other effects, we first explored the maximal spatial gradient of an empirical ionospheric model. The model we chose was the IRI 90 because of its simplicity and availability. Using this model, we could generate the electron density from 60 to more than 1000 km above the earth's surface at different latitude, longitude, local time and sun-spot-number (SSN) conditions. A result is shown in Figure 4.3.1.

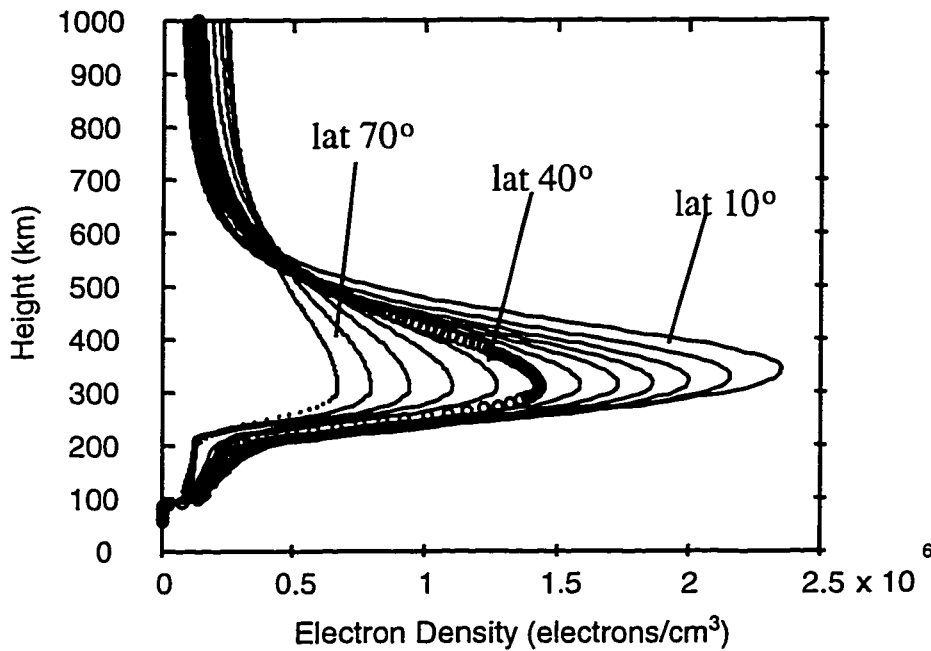


**Figure 4.3.1 Ionosphere variation gradient investigation**

Curves were generated from IRI 90 Model with input SSN=120, Longitude= 270, at 2 PM local time

Then we computed the vertical time delay from the path-integrated total electron contents (TECs) as

$$\Delta t_{iono} = \frac{8.44 \times 10^{-7}}{2\pi \cdot f_{L1}^2} TEC \text{ (seconds)} \quad (4.3.1)$$

where  $f_{L1}$  is the GPS L1 frequency (1575.45 MHz) and  $TEC$  is in units of electrons/m<sup>2</sup> [Hargreaves, 1992].

By examining different locations on the earth and different solar activities, we found that the largest ionospheric spatial gradient occurs at low latitude and high sun spot numbers (SSNs). This maximal gradient is about 1 m per 5° at 10° north latitude and SSN 200. (200 is the largest yearly sun spot number which has ever been observed, the 1996 average SSN was from 20 to 30, which are the minimal SSNs). A 2 m per 5° criterion can therefore be established for data screening purposes while not removing useful data. Future investigation using the National Satellite Testbed's large data base will establish more statistical information about the variation of the ionosphere and better define the bounds of the variation with time. This work shall help us to develop more efficient data screening process.

#### 4.3.2 IFB Errors

The IFB calibration also includes estimation errors. The confidence of IFB calibration derives from the modeling residuals in the IFB estimation process. Typically, the confidences about the relative receiver IFBs, i.e.,  $R_i - R_M$ , are better, roughly 10 cm. This is due to a cancellation of common mode errors between the  $i^{th}$  WRS and the master WRS (defined in IFB estimation). The errors in the satellite IFBs are usually bigger (30 cm) and take a longer time to converge (about one hour).

#### 4.3.3 Obliquity Errors

Another error component results from the vertical delay model itself. This simplified model describes the ionosphere as a thin slab at an assumed mean height and uses an obliquity factor (OF) to convert the measured slant delays to vertical delays. This conversion introduces an error because of the assumptions of height and constant thickness of the ionosphere. This error is especially significant where the ionosphere has a large gradient, for example at low latitudes or at the day-night termination periods. To quantify this error, we set up two LOSs with electron density profiles again simulated using the IRI 90 model, as shown in Figure 4.3.2. Because the gradient in the ionosphere from the model at a give particular SSN is most significant in the North-South direction,

the simulation had Receiver #1 looking at GPS #1 with LOS due north, and a second receiver looking at GPS #2 with LOS due south. After comparing the vertical delays from path integrals through the slant LOSs and converting via the obliquity factor with those from direct 90 degree elevation angle path integrals, we found the following results:

- ◆ At low solar activity, SSN 30, the conversion introduces less than a 7% error in the vertical delays.
- ◆ However, at very high solar activity, SSN 200, the conversion can introduce more than a 15% error.

Again, SSN 200 is approximately the highest SSN that has been observed in past solar peaks [US NGDC NOAA, 1997]. For the solar minimum, 1996, the average SSN was only 20 to 30. Table 4.3.1 lists the SSN for the last five solar maxima.

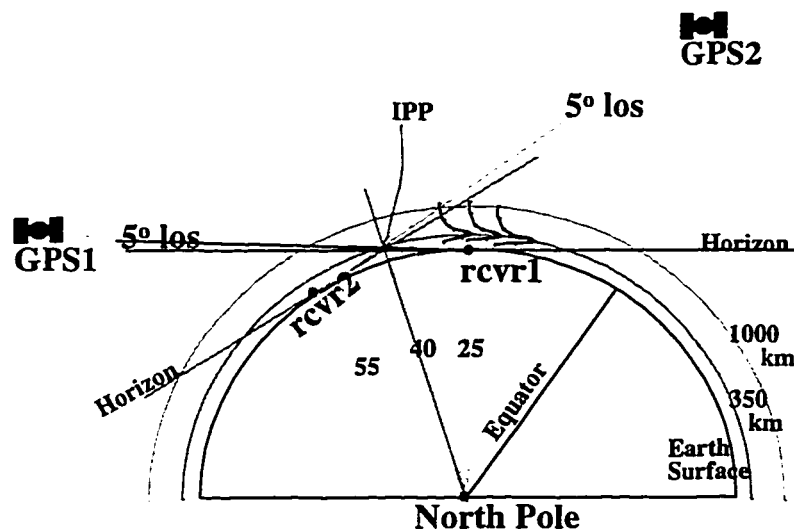


Figure 4.3.2 Obliquity Factor Errors Calculation.

Table 4.3.1 Maximal Sunspot Numbers (SSNs) for the Last Five Solar Maxima

Solar Max Year	1947	1957	1968	1979	1989
Max SSN	150	196	110	160	160

#### 4.3.4 Error Propagation of Grid Vertical Delay Model

Equation 4.3.1 and Figure 4.3.3 summarize the error propagation for modeling. The final vertical delay measurement variance is contributed by the IFB calibration, carrier-smoothing and the obliquity conversion:

$$\sigma_{meas}^2 = \frac{(\varepsilon_{smth}^2 + \varepsilon_{IFB}^2)}{OF^2} \cdot \{1 + 0.3 \exp[-(el / 40)^2]\} \quad (4.3.1)$$

where  $\sigma_{meas}^2$  is the vertical delay measurement variance and is the summation of the variances from smoothing ( $\varepsilon_{smth}^2$ ), IFB calibration ( $\varepsilon_{IFB}^2$ ), and OF scaling. The exponential function in the bracket,  $\{1 + 0.3 \exp[-(el / 40)^2]\}$ , accounts for the OF conversion error at the low elevation angle. Note that the values  $\varepsilon_{IFB}^2$  used in this study are pre-estimated using recent data sets as opposed to the values from early hardware calibration (a real-time version is under development). After the modeling process, a quantization error from the WAAS message is also added to form the final GIVE.

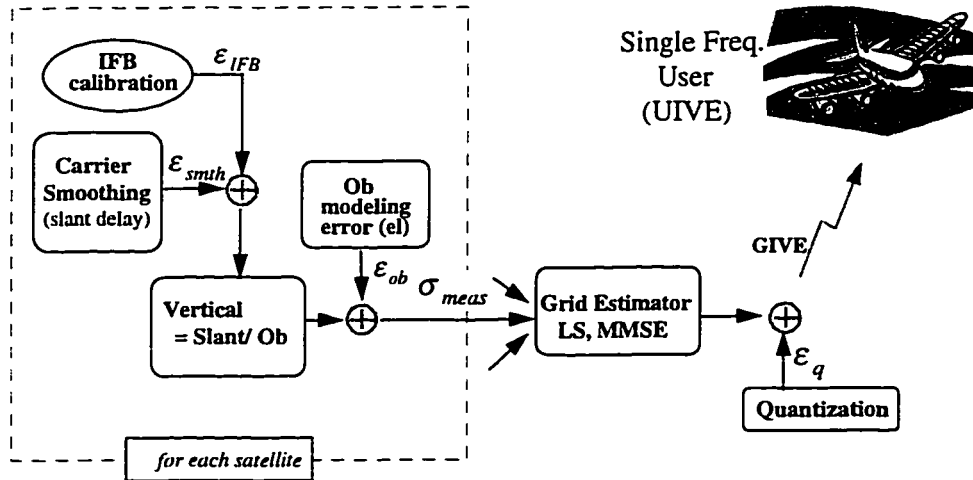


Figure 4.3.3 WAAS Ionosphere Grid Model Error Propagation.

#### 4.4 Grid Modeling Estimators

We derived two estimators for the ionospheric grid model, which we implemented to estimate the vertical delay and its confidence, grid point by grid point, eventually

completing the whole grid. The biggest benefits of this point-by-point approach are that we can better monitor the local disturbance and the integrity monitoring is therefore more robust. The two estimators were derived from the theories of Weighted Least Squares (WLS) and Minimum Mean Square Errors (MMSE). Figure 4.4.1 illustrates the generation process of the grid model.

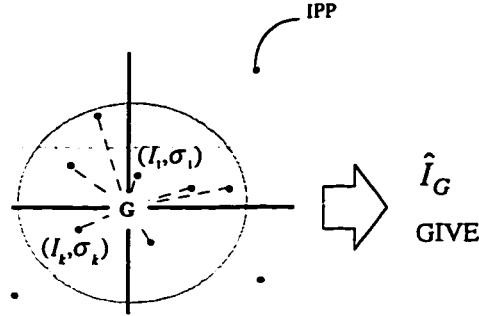


Figure 4.4.1 Illustration of Grid Model Generation

#### 4.4.1 Weighted Least-squares Estimator

The weighted least-squares, or WLS, estimator generates an estimate of  $\hat{I}_G$  and its confidence GIVE by the following weighted least-squares algorithm :

$$\hat{I}_G = \frac{\sum_{i=1}^K \left( I_i \cdot \frac{1}{\sigma_i^2} \right)}{\sum_{i=1}^K \left( \frac{1}{\sigma_i^2} \right)} \quad (4.4.1)$$

$$GIVE = 3.29 \bigg/ \sum_{i=1}^K \left( \frac{1}{\sigma_i^2} \right) \text{ for } 99.9\% \quad (4.4.2)$$

where  $\sigma_i$  is the  $i^{\text{th}}$   $\sigma_{meas}^2$  in the Equation (4.3.1). If all the IPP measurements were collocated at the grid point, then the WLS would use the inverse of the measurement variances as the weights of the IPP measurements to create the model. However, the IPPs are, in general, scattered around and we need an algorithm to transport those in the vicinity to the location of the grid point. This transportation algorithm must take the spatial shape of the general ionospheric diurnal variation when we move the IPPs. This concept can be written as the expression given in the following equation:



$$I_i = I_i \cdot \frac{I_{\text{Nominal},G}}{I_{\text{Nominal},i}} \quad (4.4.3)$$

The measurement error has to be increased to account for the error in the nominal model:

$$\varepsilon_i = \frac{\sigma_i}{\Delta} \quad (4.4.4)$$

where  $\Delta$  depends on the correlation distance of the ionosphere.

Using this approach, Equations (4.4.1) and (4.4.2) become

$$\hat{I}_G = \hat{I}_{\text{Nominal},G} \cdot \left\{ \frac{\sum_{k=1}^K \left( \frac{I_i}{I_{\text{Nominal},i}} \right) \cdot \frac{1}{\varepsilon_i^2}}{\sum_{k=1}^K \left( \frac{1}{\varepsilon_i^2} \right)} \right\}, \text{ and} \quad (4.4.5)$$

$$GIVE = 3.29 / \sum_{i=1}^K \left( \frac{1}{\varepsilon_i^2} \right) \quad (4.4.6)$$

That is, we can scale the measurements using a nominal model to transport the measurement from the IPP location to the location of the desired grid point through the relationship of latitude and longitude dependence provided by the nominal model. Currently, the Stanford WMS is using the GPS single frequency Klobuchar ionospheric model, shown in Figure 4.4.2, as the nominal model.

The distance correlation parameter  $\Delta$ , which is used to increase the measurement noise, is calculated using archived National Satellite Testbed data over the whole continental U.S. This correlation function of the ionosphere is shown in Figure 4.4.3 as function f1. To account for possible faster decorrelation in the ionospheric delays in the coming solar maximum, a second curve, denoted as function f2 in Figure 4.4.3, is actually used in the estimator. The second function decays much faster than the first one. Therefore, it will estimate the correlation between ionospheric delays more conservatively.

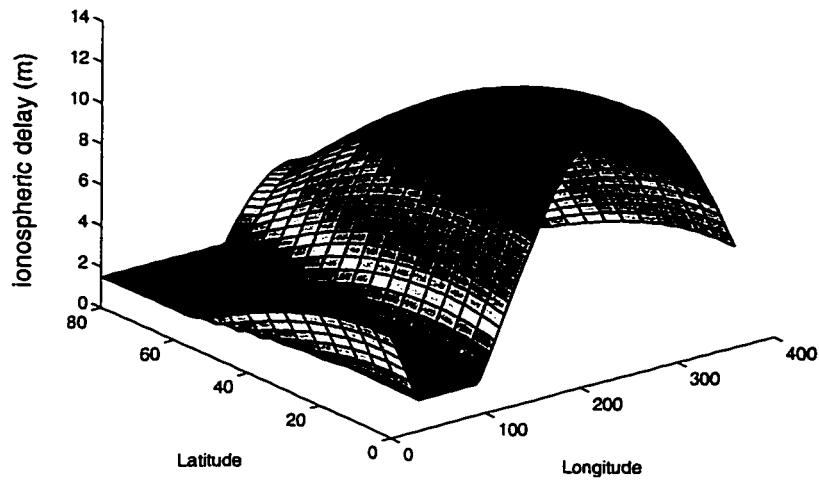


**Figure 4.4.2 Nominal Ionospheric Model: Klobuchar Model**

The ionospheric delay (z-axis, in meters) is shown in the geodetic coordinate system.

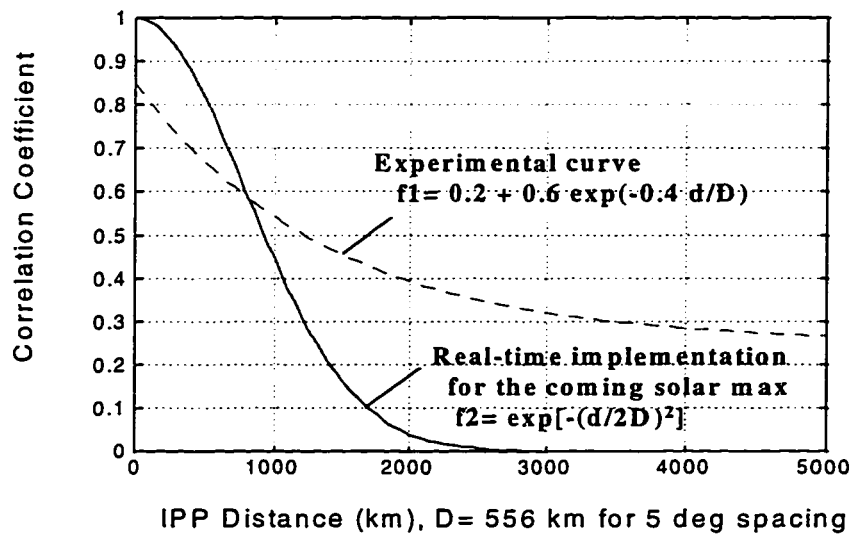


**Figure 4.4.3 Ionospheric Distance Correlation Functions**

The dotted line is the experimental curve derived from archived data in March 1996. The more conservative correlation function, solid line, is actually implemented to account for possible faster decorrelation in the coming solar maximum.

The augmentation parameter  $\Delta$ , in Equation (4.4.4), is then the function f2 in the figure, or

$$\Delta = \exp[-(d / 2D)^2],$$

where  $d$  is the distance between the IPP and the grid point and  $D$  is the distance of  $5^\circ$  separation on a great circle of the Earth.

Note that a first-order Kalman filter has been implemented to smooth the WLS snapshot estimation results. This filter smoothes the discontinuous measurements, especially that due to the outage of reference stations and can be designed to cause negligible filtering lag. The time constant of this filter is about 30 seconds.

#### 4.4.2 Minimum Mean Square Error Estimator

While the least-squares estimator assumes no prior information about the state  $\mathbf{I}_G$ , the minimum mean square error (MMSE) [Leon-Garcia, 1994] estimator utilizes prior knowledge of the nominal ionosphere model and of the possible deviation of  $\mathbf{I}_G$  from the nominal model. The same algorithm has been used for the simulation of WAAS ionospheric integrity monitoring [Pullen, 1996].

In particular, the MMSE generates the ionospheric vertical delay estimate at each grid point

$$\Delta \mathbf{I}_G = \mathbf{P}_{Gy} \cdot \mathbf{P}_y^{-1} \cdot (\Delta \mathbf{I}), \text{ and} \quad (4.4.6)$$

$$GIVE = 3.29 \times \{ E[\Delta \mathbf{I}_G^2] - \mathbf{P}_{Gy} \cdot \mathbf{P}_y^{-1} \cdot \mathbf{P}_{Gy}^T \} \quad (4.6.7)$$

where  $\Delta \mathbf{I} = [\Delta I_1, \dots, \Delta I_K]^T$  is the *deviation* of the IPP measurements from the nominal Klobuchar model,  $\mathbf{P}_{Gy} = E[\Delta \mathbf{I}_G \Delta \mathbf{I}_i]$ ,  $i = 1 \dots K$ , and  $\mathbf{P}_y = E[\Delta \mathbf{I}_i \Delta \mathbf{I}_j]$ ,  $i = 1 \dots K$ ,  $j = 1 \dots K$  are covariance matrices between the grid point and the measurement and between measurements themselves, respectively.  $K$  is the total number of IPPs used to estimate this grid point. The covariance matrices are generated using the measurement noise and the correlation coefficient, function f2 in Figure 4.4.3. In practice, they are full matrices.

For the current low ionospheric activity, a value of  $1.8 \text{ m}^2$  is used for  $E[\Delta I_G^2]$ . In general, the MMSE estimator takes more computational effort than WLS because of the matrix inversion involved. Furthermore, the performance of MMSE is very sensitive to the estimation of the distance correlation function, and therefore is not as robust as that of the WLS estimator

#### 4.4.3 GIVE Feedback Algorithm

Even with the above algorithm-generated estimation of GIVE, it is still desirable to check whether the GIVE can cover the ionospheric error up to 99.9% statistically. This check can at minimum be done for the available reference station ionospheric measurements. To implement this idea, I designed a feedback algorithm as shown in Figure 4.4.4. First of all, the WMS reconstructs an estimate of vertical delay and its confidence for each IPP measurement using the just generated grid model (the same formula from the user's algorithm in the next section is used to calculate  $\hat{I}_{model}$  and the

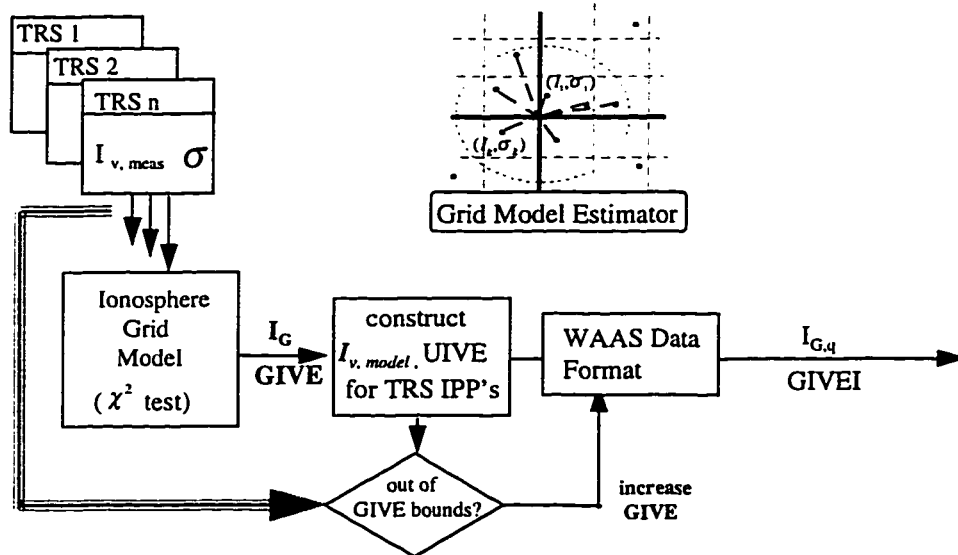
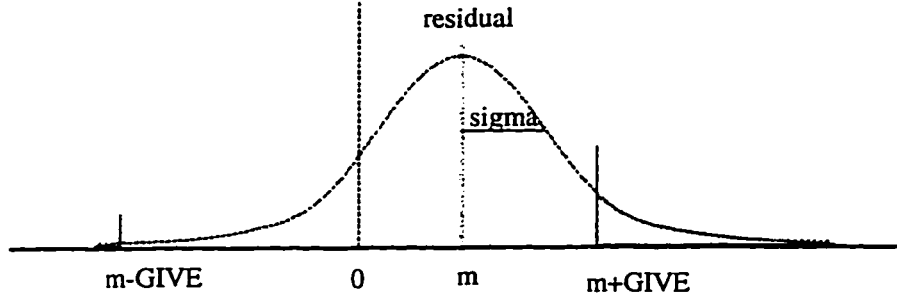


Figure 4.4.4 Feedback Algorithm for GIVE Generation



**Figure 4.4.5 GIVE to Cover 99.9% Ionospheric Error**

$m (=I_{meas} - \hat{I}_{model})$  is the ionospheric measurement residual from the grid model and  $\sigma$  is the measurement confidence (after carrier smoothing). The area at both ends under the curve (outside of the  $m+GIVE$  and  $m-GIVE$  bounds) should be less than or equal to 0.1% since GIVE has to cover 99.9% of ionospheric delay.

confidence User Ionospheric Vertical Error, or UIVE). Then the WMS can determine if UIVE covers the modeling residual,  $I_{meas} - \hat{I}_{model}$  with  $\sigma_{meas}$  up to 99.9% statistical certainty. If not, the WMS must increase the GIVEs of the four grid points surrounding that IPP measurement. After checking all the IPPs from the entire network, the amount to increase GIVE for each individual grid point is the maximum of the increment.

Figure 4.4.5 illustrates the method for making the GIVE adjustment. Note that finding the GIVE in this way is an iterative process which may not converge. Fortunately, as shown in the estimation result in the next section, the measurement residuals are quite small (better than 30 cm most of time), and the process of GIVE adjustment can be simplified by setting the mean of the measurement residual,  $m$  in the figure, to zero.

#### 4.4.4 Grid Correction Algorithm for WAAS Users

When the users decode WAAS messages, the ionospheric correction for each user IPP is constructed by interpolation. This interpolation uses the four surrounding grid points ( $I_{1..4}$ ) to compute both the ionospheric delay and the user ionospheric vertical error (UIVE) at the user's IPP location. WAAS MOPS provides formulas for the interpolation [Appendix H]:

$$I_v = \sum_{i=1}^4 w_i \cdot I_i \quad \text{and} \quad UIVE = \sum_{i=1}^4 w_i \cdot GIVE_i \quad (4.4.9)$$

where the shape of the interpolation weighting,  $w_i$ , is shown in Figure 4.4.6 (b). Figure 4.4.6 shows the interpolation and the weighting function.

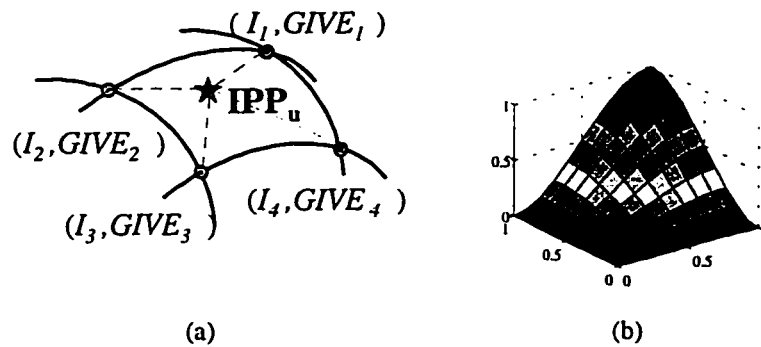


**Figure 4.4.6 User Ionospheric Grid Model Algorithm (WAAS MOPS)**

Figure 4.4.7 presents one of the grid correction results. The result shows very good modeling accuracy and UIVE covers the modeling error sufficiently. According to the accumulated statistics of the corrections, the estimation error is better than half a meter. Furthermore, UIVE covers the user ionospheric error with only 0.3% exception and most of the exceptions occur in the initial smoothing converging period. With the exception of the violations in the initial smoothing converging period, we can conclude that this estimation result satisfies the GIVE requirement. Further work has to be done for collecting large data under different conditions, especially for the coming solar maximum around year 2000.

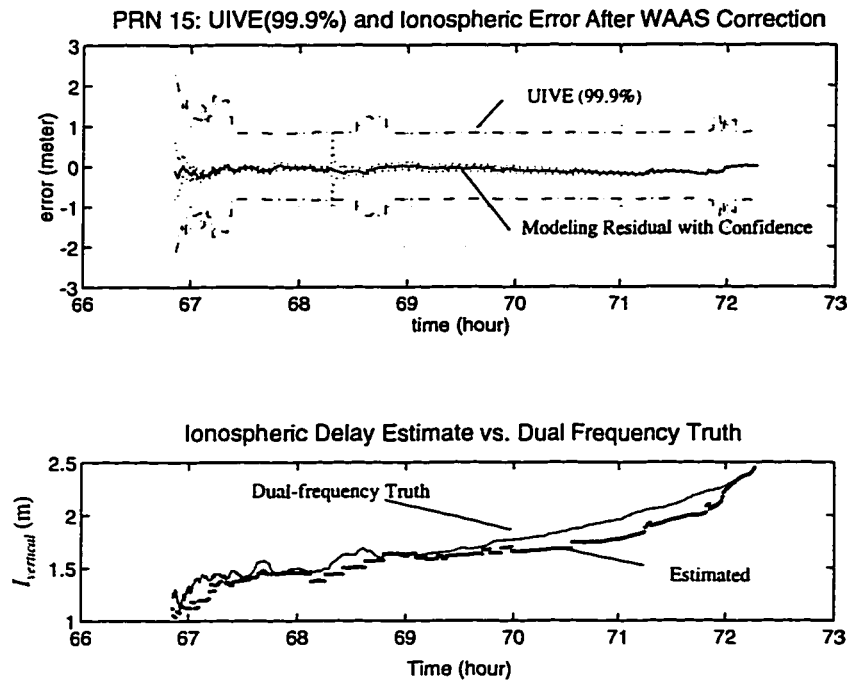


**Figure 4.4.7 WAAS Grid-derived User Ionospheric Correction Error and UIVE Bound**

Result is from the WLS grid estimator for a user's ionospheric correction of PRN 15. The lower curve presents the comparison between the grid-derived ionospheric correction and dual-frequency derived true ionospheric delay. The upper curve plots the correction error and the UIVE  $\pm 99.9\%$  bounds. This plot is generated from one of the NSTB data sets for a static user collocated at Stanford WMS.

## 4.5 Integrity Monitoring

A simulation has shown that a local fast-decorrelated ionospheric disturbance is a possible threat to WAAS accuracy and integrity [Pullen et al., 1996]. In the simulation, fast-variation ionospheric "bubbles" of different radii, from 500 km to over 1000 km, were created and superimposed on top of a nominal ionosphere model as part of the entire WAAS covariance analysis. As shown in Figure 4.5.1, it is clear that such a fast spatial-decorrelated ionospheric disturbance can degrade the WAAS correction accuracy over the entire coverage area. It is therefore important to develop a detection scheme for such fast-variation disturbances in real-time. Note that this fast decorrelation disturbance was chosen for the simulation because it is believed to be difficult to detect and not because of it is known to occur.

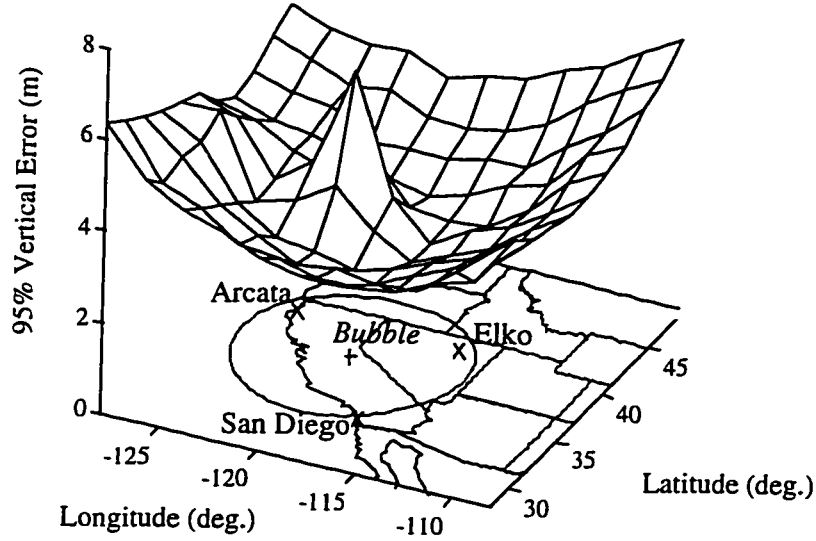


**Figure 4.5.1 Fast Decorrelated Ionospheric “Bubble”**

The user's vertical accuracy is degraded by the existence of a fast-decorrelated ionospheric disturbance. The shape of the disturbance is simulated as a bubble shown in the figure (from [Pullen et al., 1996]).

In the development of the detection scheme, the  $\chi^2$  parameter was found very useful as an event indicator. The  $\chi^2$  is a statistically valuable parameter, and is usually used in the evaluation for the goodness-of-fit in estimation theory [for example, Press et al., 1992]. Specifically, the  $\chi^2$  used in the grid estimation can be expressed as

$$\chi_i^2 = \sum_{k=1}^N \left( \frac{I_k - \hat{I}_{G,i}}{\varepsilon_k} \right)^2 \quad (4.5.1)$$

where  $\chi_i^2$  is for the  $i^{th}$  grid point,

$\hat{I}_G$  is the estimate of grid point vertical delay,

$I_k$  is the IPP measurement after the nominal model transportation,

$\varepsilon_k$  is the IPP measurement noise, the same as in Equations (4.4.4) to (4.4.6), i.e., the measurement noise used in the grid generation estimator with adjustment from the distance correlation function in Figure 4.4.3.

$N$  is the total number of IPPs used for the  $i^{th}$  grid point.



In words,  $\chi^2$  is the summation of all the IPP measurement residual squares that were used for the  $i^{th}$  grid point, where all the residuals have been *normalized* by their measurement noise. For a good fit, the ratio in Equation (4.5.1) is approximately equal to one and the  $\chi^2$  will therefore be approximately equal to its degree of freedom (DOF). As we are only estimating the grid vertical delay from  $N$  pierce point measurements,  $DOF = N-1$  for this case.

Several possible ionospheric grid measurement distributions are presented in Figure 4.5.2. The figure illustrates possible fitting conditions for estimating the grid vertical delay  $\hat{I}_G$ . In the figure, the IPP measurements are drawn with their measurement error confidence bars. A horizontal line is also shown to represent the grid estimate result for each situation. Figure 4.5.2(a) shows a desirable situation where all the measurements are lined up within their error bar ranges and the resulting confidence of  $\hat{I}_G$  is high. In the mean while, the value of  $\chi^2$  in this case will be approximately equal to its DOF for the reason stated in the previous paragraph. Note that DOF is dependent on the number of IPPs used.

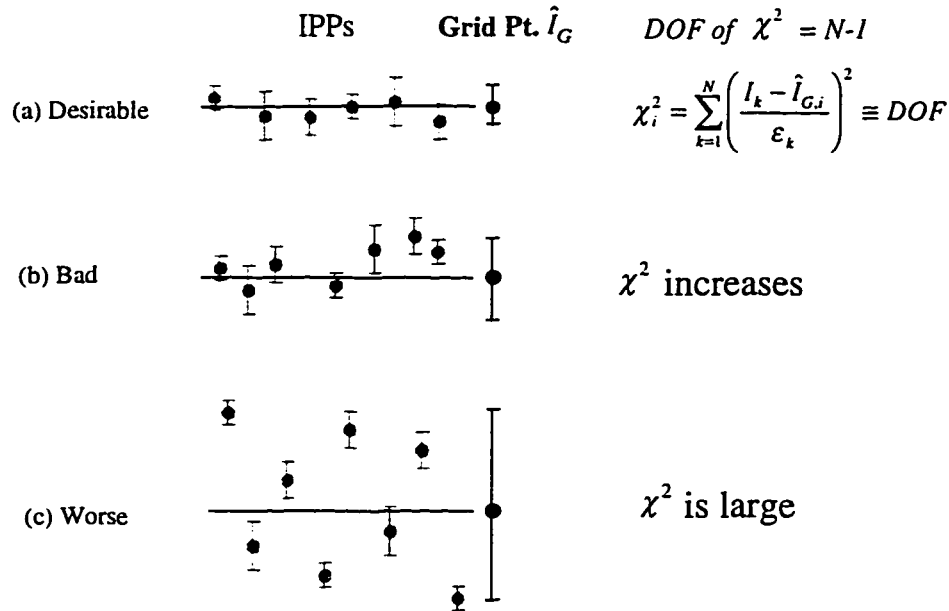


**Figure 4.5.2.  $\chi^2$  and Measurement Consistency**

DOF of  $\chi^2$  used in the ionospheric grid model is equal to the total number of IPPs used minus one.

Part (b) of Figure 4.5.2 shows a poor measurement distribution in the sense that it is not covered by the predicted measurement noise. This situation can be attributed to either fast ionospheric variation or uncalibrated measurement systematic biases. As a result,  $\hat{I}_G$  will certainly be less confident and  $\chi^2$  will increase and depart from the DOF to reflect the wide measurement distribution. As disturbances increase, Part (c), the IPP measurements are distributed more widely and with less consistency. In the last situation, we certainly have to decrease the confidence level of  $\hat{I}_G$  using the method described in the previous section. At the same time,  $\chi^2$  can provide us with information as to situation severity and could possibly be used as a disturbance indicator.

Therefore, we recorded the ionospheric  $\chi^2$  histogram using the NSTB data over CONUS for both WRS and the selected user sites. Applied to the real data, the  $\chi^2$  histogram is plotted in Figure 4.5.3 for DOFs 20 and 21 (these plots are typical for different DOFs and different WRSs or users). This figure shows the distribution of collections of  $\chi^2$  for those grid points that have the DOFs in the NSTB CONUS region for more than 13 hours. Using data from 18 WRSs and four selected users in the NSTB network (currently NSTB has 22 WRSs), many grid points that have 22 or 21 pierce point measurements are used for estimating  $\hat{I}_G$ . The  $\chi^2$  are calculated and put into the histogram bins for each instance.

The histograms clearly show that all the measurements fall into the desirable situation shown in Part (a) of Figure 4.5.2. This is actually predictable since we are now in the minimal solar activity period and therefore almost no ionospheric disturbance occurs. Furthermore, the data processing algorithm, especially the IFB calibration, has shown good estimation results in previous sections. On the other hand, the  $\chi^2$  are also bound in the processing of the no-disturbance measurements and estimation, and they provide us with a possible bound for detecting the fast-decorrelated ionospheric disturbances. From different  $\chi^2$  histograms for different DOFs, we see that we can use 3 times DOF as the  $\chi^2$  threshold for detecting the possible disturbances in the future and thus providing integrity information about the ionospheric model.

Clearly, this 3 times the DOF threshold may need some adjustments in the case of real disturbances. In this case, the wide coverage NSTB network will be very useful for collecting long term data for the ionospheric events. Note that our estimates of IPP measurement noises,  $\sigma_k$  in the denominator of Equation (4.5.1), tend to be conservative. Also in the current implementation, for the situation in which too few measurement points ( $< 3$ ) near the grid point are available, that grid point will be marked as “Do Not Use” and the user IPP can not use this grid point in the ionospheric correction and that satellite can not be used in the user’s position calculation. This is because only two IPP measurements make it difficult to detect an anomaly or a measurement outlier.

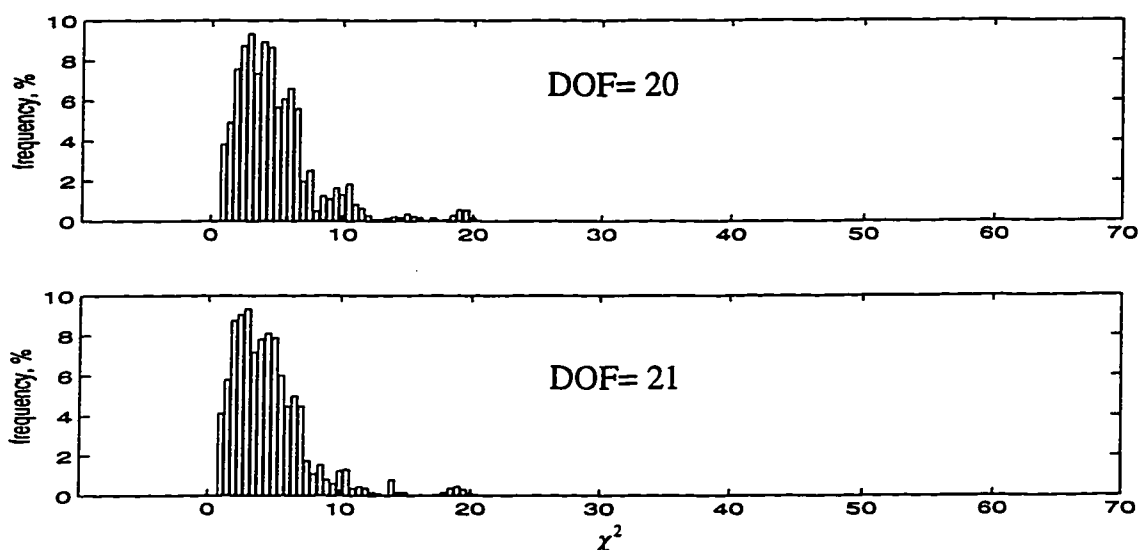


Figure 4.5.3 Histogram  $\chi^2$  for the real ionospheric data

## 4.6 Difficulty in Using GIVE

This chapter presents an algorithm for generating ionospheric correction for the WAAS grid model. Together with the IFB calibration, the WMS is able to reduce the chances of false alarm, increase the credibility of detecting disturbances, and alert the users of problems in real time.

However, there is a difficulty in using GIVE. It comes from the fact that it is designed to serve two purposes simultaneously. That is,

1. GIVE is part of the weighting algorithm (Section 2.8).

2. GIVE has to cover 99.9% ionospheric error in the grid model (Section 4.1).

The difficulty is that the user position covariance, which is directly affected by the weighting matrix, will be used to decide whether the WAAS is providing enough accuracy for Category I landings. However, in order to cover 99.9% ionospheric error, the GIVE has to be increased. This increased GIVE can easily diminish the advantage of the weighting algorithm for satellites that have been observed for a longer time and therefore have better smoothing and less noise. This is especially true in a situation of high ionospheric disturbance.

Therefore, it makes sense to split the current GIVE into two numbers, one representing the 99.9% error and one used for weighting algorithms with one sigma value. This concept needs more study, especially under the data bandwidth constraint. Note that it is not necessarily true that the magnitude of the 99.9% bound is 3.29 times that of one sigma value if the distribution is not Gaussian.

## Chapter 5

# Stanford WAAS Test Results

In order to test the real-time system and develop algorithms, the Stanford WAAS Laboratory built a testbed for the WAAS on the West Coast in 1993. Within a year, our flight test results satisfied the accuracy requirement of Category I precision approaches. Currently, we are part of the FAA National Satellite Testbed development and are continuously improving the real-time accuracy and integrity monitoring. This chapter describes the systems that we are using and presents the static and flight test results.

### 5.1 Stanford WAAS Testbed

Stanford started the WAAS program in the summer of 1993. We built four reference stations on the West Coast to form a mini-WAAS. Three of the active reference stations

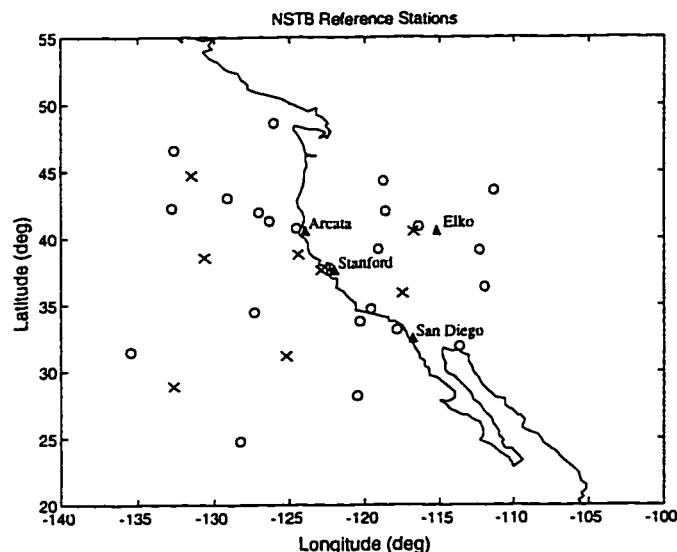
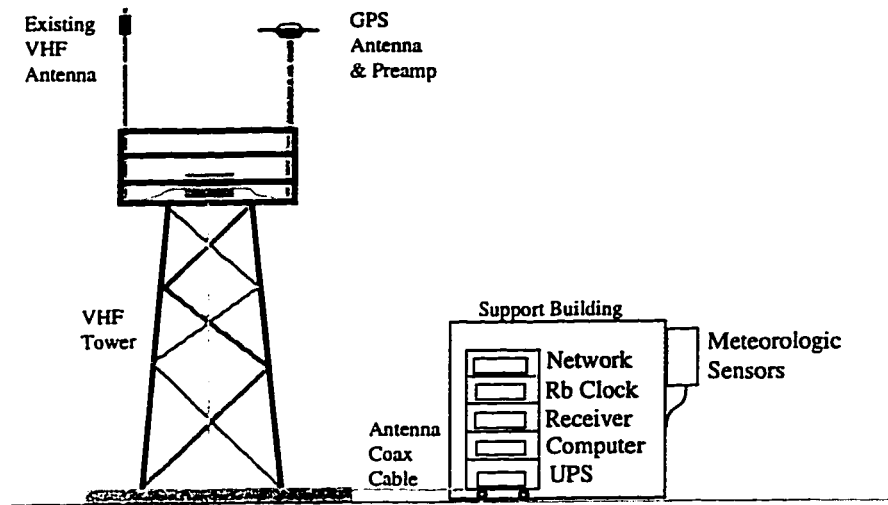


Figure 5.1.1 Stanford WAAS Testbed

Also shown are the IPP from the three reference stations (o) and from Stanford passive user (x) for a sample satellite configuration.



**Figure 5.1.2 Wide Area Reference Station Setup**

are at FAA facilities in Arcata, California, Elko, Nevada and San Diego, California (see Figure 5.1.1). The fourth reference station is located at the Stanford WAAS Laboratory to serve as a passive static WAAS user for checking the WAAS results. This station does not participate in the WAAS correction generation.

We chose Trimble 4000 SSE receivers for the reference stations, and the system consists of the receivers plus weather stations, rubidium oscillators and phone line connections. One of the reference station configurations is shown in Figure 5.1.2. Stanford's reference station contains a Trimble 4000 SSE dual-frequency receiver, a meteorological station, a computer for data collection, a Rubidium oscillator, an uninterruptible power supply, and a phone connection for transmitting the data. All the antennas were carefully placed at approximately the highest point in the vicinity to reduce the multipath effect. The positions of antenna phase centers were calculated by the Stanford Geophysics Department using GIPSY software developed by the Jet Propulsion Laboratory, CA and the U.S. Defense Mapping Agency's precise orbits.

In order to test the system's real-time accuracy and robustness, we flight tested it using Professor Powell's Piper Dakota, a single engine 4-seat aircraft. The tests occurred at Palo Alto, Livermore and Lake Tahoe. By comparing our test results with surveyed runways and with truth trajectories provided by centimeter-level accuracy Stanford

Integrity Beacon Landing System data [Cohen et al., 1994, Lawrence et al., 1996], we have consistently demonstrated better than 4 meters vertical accuracy 95% of the time over the past three years [Walter et al., 1994, Tsai et al., 1995].

## 5.2 National Satellite Testbed

To facilitate the WAAS development, FAA also initiated the National Satellite Testbed (NSTB) project. Figure 5.2.1 presents the testbed reference station network. This project, which started producing data in the summer of 1996, serves as an R & D testbed for future WAAS development. As of January 1997, the NSTB consists of a total of 22 stations across the continental U.S., including reference stations in Canada. Each testbed reference station contains equipment similar to that of the Stanford WAAS Testbed, that is, a dual-frequency receiver with a Rubidium clock as a time reference, a meteorological station and a dedicated network connection. However, the reference station will be augmented with multiple threads of receivers from different manufacturers to prevent potential common errors in a single receiver brand and to serve for multiple data validation.

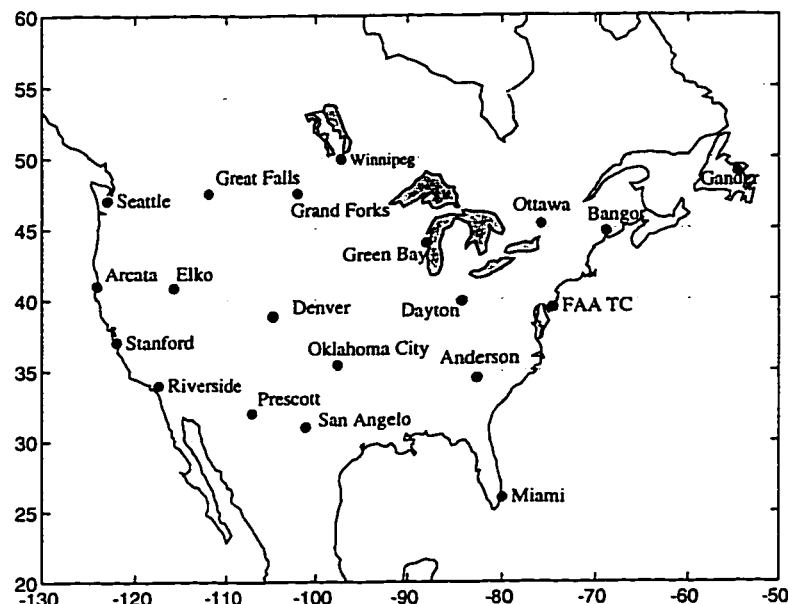


Figure 5.2.1 FAA National Satellite Testbed

Multiple testbed master stations, including the FAA Technical Center and the Stanford WAAS Laboratory, have been set up in this testbed for independent research and development. Each master station has a Digital Equipment Corp.'s Alpha computer for high-speed data processing and storage. All the master and reference stations are connected through a dedicated large-capacity network to guarantee the reduction of the data latency and to meet the time-to-alarm requirement. Currently, all data are sent to the FAA Technical Center first and routed to Stanford via a fast dedicated link (called a T1 line) at 1.544 Mbps data rate.

### 5.3 Stanford WAAS Data Flow

To develop the real-time WAAS research and to validate the WAAS MOPS message types under the data constraints, Stanford started building both the hardware and software of the WAAS under FAA grants. Figure 5.3.1 shows the data processing at the Stanford's master station. Both the raw receiver and weather station data are transmitted back to the master station through a network connection. The master station uses these measurements to calculate the ionospheric delay and smoothed pseudo-range residuals:

- ◆ The meteorological sensors provide relative humidity, pressure and temperature of each WRS and this meteorological information is used to calculate the tropospheric delay correction to the pseudorange for each WRS. The modified Hopfield model [Appendix C] is used to calculate the tropospheric delays.

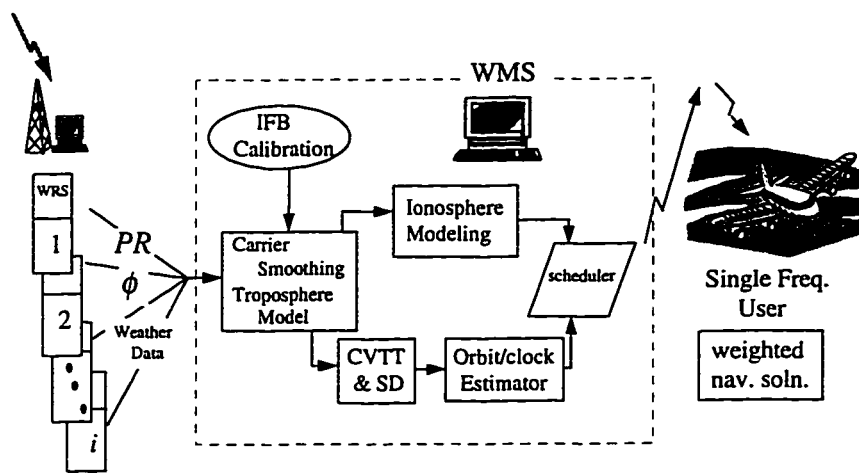


Figure 5.3.1 The Stanford WAAS Data Processing Flow



- ◆ The dual-frequency pseudoranges are used to calculate the ionospheric delays and the carrier-phases are used for the carrier-aided smoothing.
- ◆ Both the ionospheric and tropospheric delays were used to form the ionosphere-free, troposphere-free smoothed pseudorange residuals for each satellite. In the meanwhile, the pre-computed interfrequency bias values are calibrated out of the measurements.

Using the ionospheric delay measurements and the pseudorange residuals, TMS creates an ionospheric vertical delay model and estimate the satellite orbit/clock, respectively. The next step is to encode the corrections and integrity warnings into WAAS 250 bps message formats and transmit to the users [Tsai et al., 1995, Lawrence et al., 1996].

## 5.4 Test Results

As already mentioned, we have flight tested our real-time WAAS data frequently in past years. Figure 5.4.1 shows the test vehicle, a Piper Dakota. The on-board computer contains user software and a Novatel GPS 12-channel receiver. Without access to the GEO satellite link at 250 bps data rate, we implemented the flight tests at the Palo Alto airport with a local ultra-high frequency data link in touch-and-go patterns. In the early stages of development, the surveyed runway coordinates, accurate to 30 cm, were used to

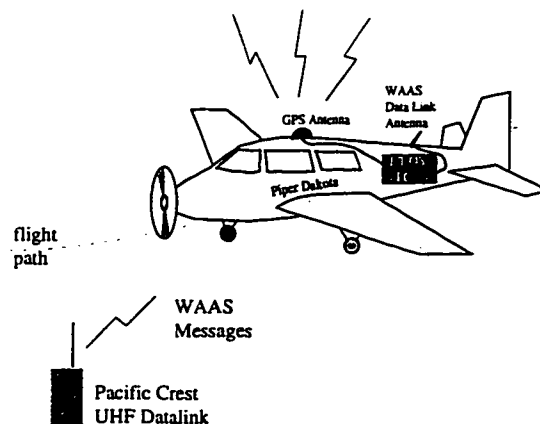


**Figure 5.4.1 Flight Test Using Piper Dakota and Local Data Link**

provide the vertical positioning truth of our flight tests while the aircraft was on the runway.

Beginning in 1996, we converted the WAAS user computer to run under the real-time operating system LYNX. This operating system allows for multi-thread processing and facilitates running both the Stanford Integrity Beacon Landing System (IBLS) and WAAS processes in parallel. IBLS, a real-time centimeter level GPS carrier-derived positioning system, provides WAAS with real-time truth-in-the-air data [Lawrence et al., 1996].

Figure 5.4.2 presents typical flight test results obtained in July 1996. This figure shows the WAAS positioning errors in the east, north and vertical directions in meters. The flat lines at the center show the WAAS results. The GPS-alone results are also plotted for comparison. Although this is only an example of our flight test results, our accumulated dynamic and static test results consistently show that Stanford WAAS provides better than the vertical guidance requirement of Category I landing over the CONUS. The 95% positioning errors of horizontal and vertical are about 2.0 meters and 3.5 meters, respectively.

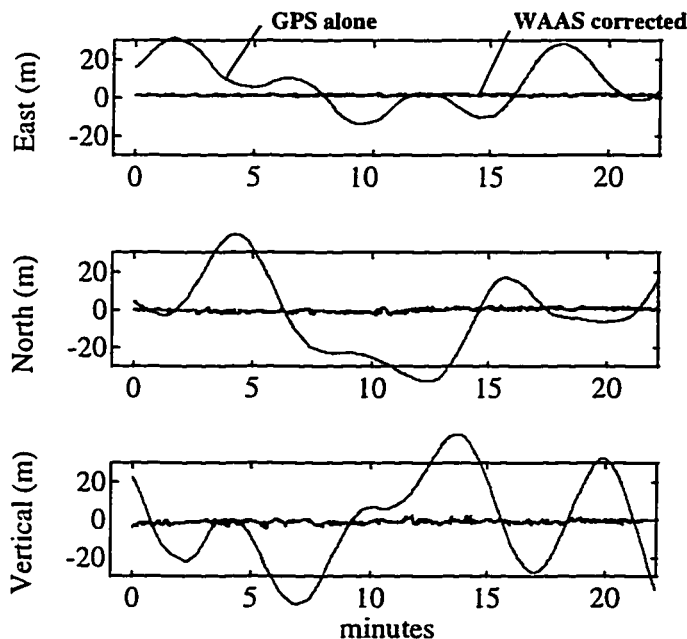


**Figure 5.4.2 WAAS Airborne User Positioning Errors**

Due the imperfect local data link, the outliers strictly due to the data link problem have been taken out for fair comparison. Currently, considerable effort is being directed to the improvement of the data link, including application for dedicated frequency from the FCC.

Furthermore, Figure 5.4.4 shows the improved velocity information derived from WAAS correction. These velocity errors are calculated from a static receiver using WAAS corrected Doppler measurements (the RMS values are 5 cm/sec in three dimensions). Note that these range rate corrections were inferred from pseudo-range corrections. Simulation results have shown that this highly accurate velocity can also be applied to enhance on-board display information for pilots.

The recent NSTB positioning accuracy histograms for Stanford and the FAA Technical Center, which served passive users in the processing to verify the WAAS solutions, are presented in Figure 5.4.5 for east, north and vertical directions. Again, as summarized in the graph, the 95 percentile in all three directions for both sites are well within the Category I approach 7.6-m accuracy requirements. To illustrate the distribution of outliers, the 99.9 percentile is also presented for the tails in the histograms. According to the accumulated statistics, these 99.9% errors are also within the bound of 7.6 meters. Table 5.4.1 summarizes the results of this data set.

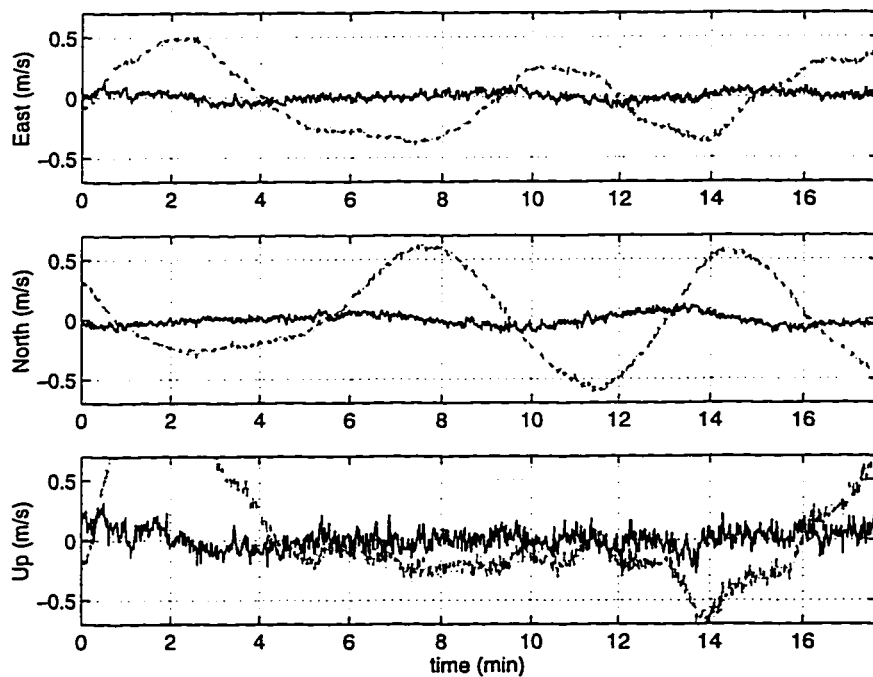
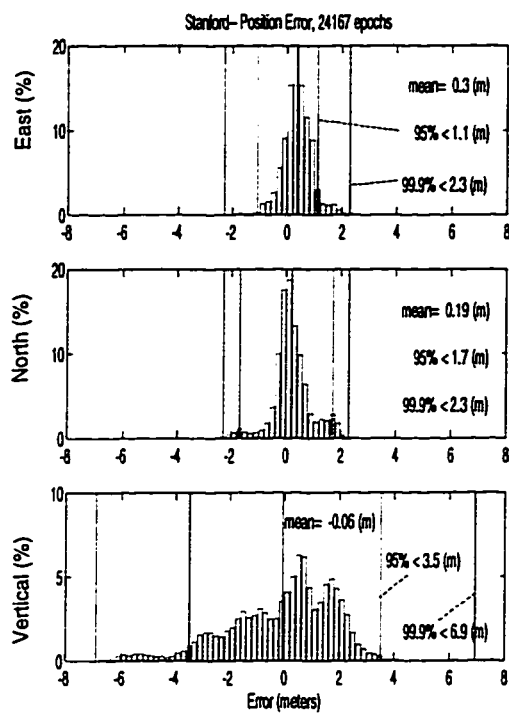
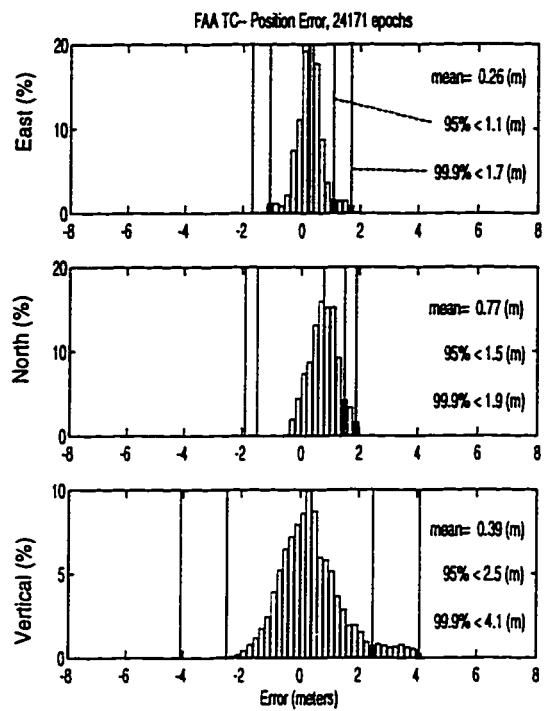


**Figure 5.4.3 WAAS Static User Velocity Errors**

Velocity solutions were derived from Doppler measurements and WAAS inferred pseudorange rate corrections. Solid darker line is the WAAS corrected velocity solution and the dotted line is the GPS-alone solution (Data is from NSTB).



(a)



(b)

**Figure 5.4.4 WAAS Static User Positioning 3-D Error Histogram**

Data is from NSTB for more than 10 hours, October 15th, 1996. (a) Stanford User (b) FAA Technical Center User.

**Table 5.4.1 Summary of 3-D Error Histogram**

Station Name	Stanford			FAA Tech Center		
	East	North	Vertical	East	North	Vertical
mean (m)	0.3	0.2	-0.1	0.3	0.8	0.4
95% (m)	1.1	1.7	3.5	1.1	1.5	2.5
99.9% (m)	2.3	2.3	6.9	1.7	1.9	4.1

## Chapter 6

# Conclusions

**W**AAS has been designed to be the primary aircraft navigation system all over the country with flexible extension internationally. With WAAS navigation accuracy and integrity, more than one thousand airfields in the continental U.S. (CONUS) can immediately have access to the Category I precision approach capability without any local navigation ground equipment installation. WAAS has attracted a great deal of attention internationally in recent years because of its wide coverage and cost-effectiveness.

There are more than 1000 airfields in CONUS equipped with Instrument Landing Systems (ILSs) today. When the time comes to retire the ILS, these airports will be ready for and benefit from the next generation navigation system, WAAS. For the rest of the small airfields (estimated at over 5000 in CONUS), even with the WAAS accuracy, still need to add landing lights and special patterns painted on the runway surface to be qualified to perform the Category I precision approach. However, these airports can enjoy vertical guidance to decision height above 200 ft the new lights installed and patterns painted.

### 6.1 Summary of Contributions

In Chapters 3 and 4 of this thesis, I described the essential elements of generating the ionospheric corrections and integrity monitoring for the WAAS grid model. The following is a summary of contributions described in the previous chapters.

- ♦ *I developed and calibration algorithm for the interfrequency biases (IFBs) between the L1 and L2 measurements. The broadcast satellite IFB values are not monitored and were shown to be in error by up to several meters. The biases in the receivers can also be several meters. Even with precalibration, these biases can still deviate*

from the calibrated value by more than one meter because of the variation of receiver ambient temperature and other factors. The accuracy of the bias calibration has been demonstrated up to 30 cm. Using this calibration for these systematic biases, not only are the biases of the WAAS users' vertical positioning errors reduced, but the distribution is narrowed as well. Most importantly, this calibration reveals the accuracy that is necessary for further system error analysis and integrity monitoring.

From the real-time data processing experience, we found that the IFB calibration has to be done more frequently than we first thought. Because of the temperature dependent characteristics and the possible ambient temperature variation around the receivers at each WRS, we recommend estimating the IFB on-line. Test results of this approach demonstrate improvements. The IFB estimator is currently merged with the master station process to perform the on-line calibration.

- ◆ Using a ionospheric modeling estimator based on a grid algorithm, I demonstrated the accuracy of the WAAS ionospheric grid modeling over the Continental U.S., and the feasibility of integrity monitoring of the grid ionospheric vertical model. In particular, I formalized the modeling approach using a Weighted Least-squares (WLS) algorithm with ionospheric spatial correlation function. The accuracy of this estimator is better than half a meter. This spatial correlation function was experimentally determined from archived NSTB March 1996 data. To account for the possible faster ionospheric decorrelation in the coming maximum solar cycle, which is around the turn of the century, I implemented a more conservative curve in a real-time algorithm for the system robustness. This modeling procedure also includes an error propagation procedure and error analysis, which has been proved to be effective in the real-time data processing.
- ◆ *I developed an information feedback algorithm for generating grid ionospheric vertical error (GIVE).* This algorithm guarantees GIVEs can offer 99.9% statistical reliability in covering the ionospheric error. Test results support this approach well.
- ◆ This study also proposed integrity monitoring mechanism for the detection of ionospheric disturbance in the grid ionospheric vertical delay model. This scheme

uses  $\chi^2$  to calculate the goodness-of-fit in the modeling process. From real-time data processing results, a threshold is set using the degree-of-freedom of the  $\chi^2$  parameter to detect ionospheric fast-decorrelated disturbances.

In addition, the Stanford WAAS development team, of which I have been a member since its formation, has demonstrated the accuracy of the Category I precision approach using a three-station mini-WAAS Testbed on the West Coast since 1993. We developed both hardware and software for real-time implementation, and we have flight-tested the system at Palo Alto and the Truckee, Lake Tahoe areas. At the time of writing, we are showing the same level of accuracy (4 meters in vertical and 2 meters in horizontal, 95% of the time) in real time using the data from the 20 reference stations of National Satellite Testbed.

Specifically, we developed a real-time algorithm for separating the slow and fast WAAS corrections with the 250 bit/second data constraint and validated the message types described in the WAAS MOPS. That is, our algorithm effectively separated the satellite clock errors (fast), the satellite orbital errors (slow), and ionospheric delays (also slow). For the real-time data processing:

- ◆ I developed an efficient clock filter for estimating the free-running receiver Rubidium oscillator under the effect of satellite SA, and
- ◆ With the Common View Time Transfer method, I proposed and implemented a single-difference snap-shot estimator for separating the satellite clock and orbital errors which is part of the claims in the patent of Enge, Walter and Chao [Enge et al., 1997].

## 6.2 Conclusions

WAAS is steadily progressing to deliver the primary navigation system service. The research and development work at the Stanford WAAS Laboratory, in particular, has consistently demonstrated and met the strict test of the vertical 7.6-m guidance

requirement for Category I landings. The current estimated 95% capability is 4 meters from Stanford WAAS.

The integrity monitoring required in this navigation service is still the most important task for the signal-in-space WAAS. Because of the nature of the ionosphere, the ionospheric disturbances are especially difficult to detect. The integrity monitoring of the ionospheric corrections is therefore one of the most significant challenges in the quest to achieve the full capabilities of WAAS.

At Stanford, we have started the first steps toward the ionospheric modeling. Although the grid vertical delay model is simple to implement, it has weakness in the modeling accuracy. However, we have demonstrated the feasibility of reaching the desired accuracy and integrity monitoring capability of this approach. Certainly, the multiplication parameter used in setting up the  $\chi^2$  threshold will need to be further verified or fine-tuned from a larger data base. This work should focus on the data at solar maximum.

### 6.3 Recommendations of Future Work

Much work still has to be done to realize our main goal of developing a primary navigation system. For example, with respect to the ionospheric modeling, the following research is very important:

- ◆ NSTB provides us with an unprecedented tool to observe and model the ionosphere in real-time. We need to take advantage of the large coverage provided by the NSTB to collect long-term data and to capture possible disturbances. This will certainly enhance our background knowledge of the ionosphere and provide more information about monitoring it.
- ◆ With more understanding of the ionosphere and by investigating historically recorded ionospheric storm data, we should be able to make the  $\chi^2$  disturbance threshold more realistic for the coming solar maximum.
- ◆ Hardware simulation of the receiver and investigation of the interfrequency bias variations may explain the temperature dependence of the biases more clearly, and



may help us in making progress in the reduction of the biases from receivers.

However, this work will greatly depend on the specific receiver design.

- ◆ Real-time ionospheric tomography is an emerging technology that has great potential for improving the ionospheric integrity. Further investigation of this approach is worthwhile and some progress has already been made at the Stanford WAAS Laboratory.
- ◆ Study about ionospheric scintillation, especially in the low and high latitude regions, is necessary in order to expand WAAS to Hawaii, Alaska, and eventually to the entire globe. This study should also include improvement of receiver tracking capability under the ionospheric scintillation condition.

## **6.4 A Final Remark**

A navigation system needs not only accuracy but also reliable integrity monitoring. It seems WAAS can meet the accuracy requirement with the current effort. In the future, turning the SA off will relieve the data communication bandwidth constraint and will allow the master station to send more ionospheric information to the users. Furthermore, the measurement error will be smaller without SA and the system will become more robust to WAAS communication data link outage. Another interesting development is the assignment of the second civilian frequency, known as L5, which may be available in the next generation of GPS satellites. This might actually change the direction of the ionospheric study for WAAS.

Finally, we still need to develop a more detailed concept and algorithm to detect data outliers and to monitor the system integrity in order to make this signal-from-space navigation system work for the future.

# Appendix A

## Position and Velocity from GPS

This appendix presents the GPS snap-shot point positioning and velocity solutions. Figure 1.2.2 demonstrates the non-differential position result, and Chapter 5 shows the WAAS corrected test results.

### A.1 GPS Position Solution

To find their positions and time, GPS users must have at least four satellites in view. The least-squares solution is presented below:

**[Known]:** Satellite position  $X^j, Y^j, Z^j$  in World Geodetic System-84 (WGS-84) coordinate, and satellite clocks bias  $B^j$  with respect to GPS time ( $j=1..N, N \geq 4$ , and  $N$  is the number of satellites in view). All of this information is included in the GPS broadcast messages. Note that satellite broadcast parameters for calculation of  $B^j$  does not include Selective Availability (SA).

**[Unknown]:** User position  $X_u, Y_u$  and  $Z_u$  and receiver clock bias  $b_u$ , or state vector

$$R_u = [X_u \ Y_u \ Z_u \ b_u]^T \quad (\text{A.1.1})$$

**[Measurement]:** Pseudoranges ( $PR$ ) between satellite  $j$  and the user  $u$ , i.e.,

$$PR_u^j = \rho_u^j + b_u - B^j + \varepsilon_u^j, \quad \text{or} \quad (\text{A.1.2})$$

$$PR_u^j + B^j = \sqrt{(X_u - X^j)^2 + (Y_u - Y^j)^2 + (Z_u - Z^j)^2} + b_u + \varepsilon_u^j \quad (\text{A.1.3})$$

where  $\varepsilon_u^j$  contains all the error sources in the  $PR$  measurement. For example, it contains the SA, ionospheric and tropospheric delays, multipath and receiver thermal noise in non-differential model. However, in the differential GPS mode, the error,  $\varepsilon_u^j$ , is greatly reduced by corrections.

**[Solution]:** Because the number of measurements is greater than the number of states ( $N \geq 4$ ) and the  $PR$  measurements are nonlinear in terms of the state vector  $[X_u, Y_u, Z_u, b_u]$ , the GPS positioning is an overdetermined nonlinear problem. A commonly

used technique is to linearize the measurement with respect to an initial guess,  $\bar{\rho}_u^j$  and  $\bar{b}_u$ , and to estimate the solution iteratively using the least squares approach. For the specific problem at hand, the linearized measurements can be expressed in state-space form as

$$z_u^j = \delta PR_u^j = PR_u^j + B^j - \bar{\rho}_u^j - \bar{b}_u = H^j r_u + v_u^j \quad (\text{A.1.4})$$

where

$$\begin{aligned} H^j &= \begin{bmatrix} \frac{\partial PR_u^j}{\partial X_u} & \frac{\partial PR_u^j}{\partial Y_u} & \frac{\partial PR_u^j}{\partial Z_u} & 1 \end{bmatrix}_{4 \times 1} \\ &= \begin{bmatrix} \frac{(X_u - X^j)}{\rho_u^j} & \frac{(Y_u - Y^j)}{\rho_u^j} & \frac{(Z_u - Z^j)}{\rho_u^j} & 1 \end{bmatrix}_{4 \times 1} \end{aligned} \quad (\text{A.1.5})$$

and  $r_u$  is the deviation from best estimate of the previous iteration step. After accumulating over all satellites in view, we have the full matrices,

$$H = \begin{bmatrix} H^1 \\ \vdots \\ H^N \end{bmatrix}_{N \times 4} \quad \text{and} \quad z = \begin{bmatrix} z_u^1 \\ \vdots \\ z_u^N \end{bmatrix}_{N \times 1} \quad (\text{A.1.6})$$

where  $N$  is the total number of satellites in view.

The overdetermined least-squares solution is  $\hat{r}_u = H^+ z$ , where  $H^+ = (H^T H)^{-1} H^T$  is the pseudo-inverse of  $H$ , or

$$\hat{r}_u = (H^T H)^{-1} H^T z \quad (\text{A.1.7})$$

and the best estimate is found iteratively as  $\hat{R}_{u,k+1} = \hat{R}_{u,k} + \hat{r}_{u,k}$  where  $k$  represents the  $k^{\text{th}}$  iteration step until the magnitude of the update,  $\|\hat{r}_k\|_2$ , smaller than a criterion.

Notes:

- ◆ Because of all the ones at the last column of the observation matrix  $H$ , the solutions of receiver clock error is the common part (i.e. the average) of  $PR$ s. That is, anything common to all the  $PR$  measurements will be absorbed into the receiver clock bias estimate without affecting the accuracy of user's position.

- ◆ From processing experience, the convergent rate of this iteration is fast, usually less than three to five iterations, to reach the convergent criterion  $\|\hat{r}_k\|_2 = 1 \text{ cm}$ .
- ◆ A weighted least-squares solution of  $\hat{r}_{\text{weighted}} = (H^T W H)^{-1} H^T W z$ . From the Best Linear Unbiased Estimation Theory (BLUE), the weighting matrix is  $W = V^{-1}$ , where  $V$  is the measurement noise covariance matrix. In this weighted form, the covariance matrix of the estimated state is  $P = (H^T W H)^{-1}$  [Franklin et al., 1990].
- ◆ If all the noises in  $PR$ s are the same, i.e.,  $V = \text{diag}[\sigma_{PR}^2]_{N \times N}$ , then the position covariance can be expressed as  $P = \sigma_{PR}^2 \cdot (H^T H)^{-1}$ . In other words, the variances of the states are the products of the measurements variance and the respective diagonal elements of the matrix  $(H^T H)^{-1}$ . These diagonal elements are usually referred to as Dilution of Positions (DOPs) and are related to the satellite geometry. From this relationship, we want the DOPs to be as small as possible. This roughly means that the distribution of satellite positions in the sky is as uniform as possible.
- ◆ For an underdetermined case ( $N < 4$ ), such as the orbit estimation problem discussed in Chapter 2, the pseudo-inverse of  $H$  can be shown to be  $H^+ = H^T (H^T H)^{-1}$ . This is also referred to as the minimum-norm estimation.
- ◆  $H$  is a  $N \times 4$  and can consume more computational memory if  $N$  (number of satellites in view) is large. However, for solving navigation position, we need only to form the fixed-size  $4 \times 4$  matrix  $(H^T W H)_{4 \times 4}$  and the  $4 \times 1$  vector  $(H^T W z)_{4 \times 1}$ . To avoid allocating a large array in the program, the following equations can be used for uncorrelated measurement noises where the weighting matrix  $W$  is diagonal:

$$H^T W H = \sum_{i=1}^N (H_i^T W_i H_i)_{4 \times 4} \quad (\text{A.1.8})$$

$$H^T W z = \sum_{i=1}^N (H_i^T W_i z_i)_{4 \times 1} \quad (\text{A.1.9})$$

So one must only allocate a  $4 \times 4$  matrix and a  $4 \times 1$  for the accumulations in the above expression.

## A.2 Velocity Estimation

This section describes a least-squares solution of the user velocity using Doppler measurements.

**[Known]:** The satellite 3-D velocity in WGS-84 and satellite clock bias rate

$\dot{X}^j, \dot{Y}^j, \dot{Z}^j$  and  $\dot{b}^j$ . These parameters can be calculated from broadcast navigation information.

**[Unknown]:** The user's velocity and the drift rate of the clock error, that is, the state

$$\text{vector } \dot{R} = [\dot{X}_u \quad \dot{Y}_u \quad \dot{Z}_u \quad \dot{b}_u]^T \quad (\text{A.2.1})$$

**[Measurement]:** The range rate  $\dot{\rho}$  can be calculated from the GPS Doppler measurement:

$$f_r = f_s \cdot (1 - \frac{\dot{\rho}}{C}) \text{ then } \dot{\rho} = \frac{C}{f_s} (f_s - f_r) \quad (\text{A.2.2})$$

where  $f_s$  is the frequency of the source and  $f_r$  is the received frequency affected by the relative motion between the receiver and the satellite.

**[Solution]:** The range rate between satellite  $j$  and user  $u$ ,  $\dot{\rho}_u^j$ , can be written as

$$\begin{aligned} \dot{\rho}_u^j &= \hat{\mathbf{1}}_{u,LOS}^j \cdot (\mathbf{V}^j - \mathbf{V}_u) + \dot{b}_u + \varepsilon_u^j \\ &= \frac{X^j - X_u}{\rho_u^j} (\dot{X}^j - \dot{X}_u) + \frac{Y^j - Y_u}{\rho_u^j} (\dot{Y}^j - \dot{Y}_u) + \frac{Z^j - Z_u}{\rho_u^j} (\dot{Z}^j - \dot{Z}_u) + \dot{b}_u + \varepsilon_u^j \end{aligned} \quad (\text{A.2.3})$$

The measurement can be written as

$$z_u^j = \dot{\rho}_u^j - \hat{\mathbf{1}}_{u,LOS}^j \cdot \mathbf{V}^j = -\hat{\mathbf{1}}_{u,LOS}^j \cdot \mathbf{V}_u + \dot{b}_u + \varepsilon_u^j \quad (\text{A.2.4})$$

In the state-space format,

$$z_u^j = H^j \cdot \dot{R}_u + \varepsilon_u^j$$

where

$$H^j = \begin{bmatrix} -\frac{X^j - X_u}{\rho_u^j} & -\frac{Y^j - Y_u}{\rho_u^j} & -\frac{Z^j - Z_u}{\rho_u^j} & 1 \end{bmatrix}_{4 \times 1} \quad (\text{A.2.5})$$

Then the weighted least-squares solution of velocity is

$$\hat{\dot{R}} = (H^T W H)^{-1} H^T W z \quad (\text{A.2.6})$$

where  $H$  and  $z$  are the accumulated observation matrix and measurement vector (same notation as in Equation A.1.6). The weighting function used is

$$W = \begin{bmatrix} SNR_1^2 & & 0 \\ & \ddots & \\ 0 & & SNR_N^2 \end{bmatrix} \quad (A.2.7)$$

Note that

- ◆ The velocity estimation presented above is linear provided the position is known, therefore no iteration is involved. Furthermore, although the weighting scheme is simple, it has sufficiently de-weighted the low elevation satellites and the test results are found satisfactory.
- ◆ A Kalman filter can also be constructed to estimate both user position and velocity simultaneously with  $PR$  and Doppler as measurements. However, as in many estimation problems, the filtering process will introduce delays. This delay will be more apparent when the aircraft maneuvers. A third order process model including the acceleration may be used to minimize the latency. However, this third order model significantly increases the complexity of the estimation. Since the method presented above yields satisfactory results (as shown in Chapter 5), we use this “snap-shot” estimator presented in this appendix for our flight tests.
- ◆ Satellite velocity is calculated from the differentiation of broadcast satellite orbital elements in ECEF coordinates. To simply calculate velocity from orbital elements without differentiation is *NOT* appropriate since the orbital plane is not a constant plane under the perturbations.
- ◆ For WAAS users,  $PR$ s are corrected for satellite location error, SA and ionospheric delays. The range rate measurements can be corrected from the inferred  $PR$  correction rate, i.e. SA rate and satellite velocity in the user LOS. We also correct the range rates by the change rate of ionospheric and tropospheric delay which are mainly caused by the changing of LOS elevation angles.

## Appendix B

# Covariance Analysis of Satellite Location

## Error for LADGPS and WADGPS

This appendix describes the covariance analysis for differential correction error in the pseudorange caused by the satellite location error for both LADGPS and WADGPS techniques. The variances of errors are used as the simulation presented in Section 2.1.

### B.1 LADGPS Correction Error Analysis

The reference station generates the local area correction for the nearby user. For the satellite location error and clock bias, the error in the differential correction for the pseudorange between satellite  $j$  and user  $u$  (due to spatial decorrelation) can be calculated as:

$$\begin{aligned}\varepsilon_L &= (\Delta \mathbf{r}^j \cdot \hat{\mathbf{l}}_u^j - B^j + v_u^j) - (\Delta \mathbf{r}^j \cdot \hat{\mathbf{l}}_r^j - B^j + v_r^j) \\ &= \Delta \mathbf{r}^j \cdot (\hat{\mathbf{l}}_u^j - \hat{\mathbf{l}}_r^j) + v_u^j - v_r^j\end{aligned}\quad (\text{B.1.1})$$

where  $\hat{\mathbf{l}}_u^j$  and  $\hat{\mathbf{l}}_r^j$  are the line of sight (LOS) unit vector from the user (subscript  $u$ ) and reference station (subscript  $r$ ) to the satellite (superscript  $j$ ), respectively. Note that the satellite clock  $B^j$  is perfectly canceled and the error is caused by different projection onto the two LOSs.  $v_u^j$  and  $v_r^j$  account for the user and reference station measurement errors, respectively. Figure B.1.1. shows the LADGPS geometry.

Since  $\hat{\mathbf{l}}_u^j = \bar{\mathbf{r}}_u^j / \|\bar{\mathbf{r}}_u^j\|$  and  $\hat{\mathbf{l}}_r^j = \bar{\mathbf{r}}_r^j / \|\bar{\mathbf{r}}_r^j\|$ , Equation (B.1.1) can also be expressed as

$$\varepsilon_L = \Delta \mathbf{r}^j \left( \frac{\bar{\mathbf{r}}_u^j}{\|\bar{\mathbf{r}}_u^j\|} - \frac{\bar{\mathbf{r}}_r^j}{\|\bar{\mathbf{r}}_r^j\|} \right) + v_u^j - v_r^j \quad (\text{B.1.2})$$

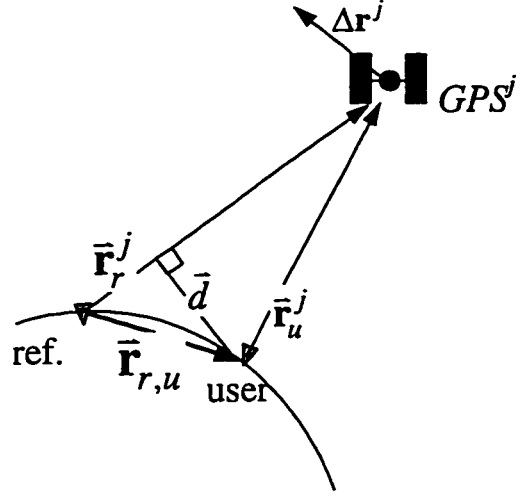


**Figure B.1.1 Geometry of LADGPS**

From the geometry,  $\bar{\mathbf{r}}_u^j$  and  $\bar{\mathbf{r}}_r^j$  are related by

$$\bar{\mathbf{r}}_u^j = \bar{\mathbf{r}}_r^j - \bar{\mathbf{r}}_{r,u} \quad (\text{B.1.3})$$

by expanding the expression, we have

$$\begin{aligned} \|\bar{\mathbf{r}}_u^j\|^2 &= \|\bar{\mathbf{r}}_r^j\|^2 + \|\bar{\mathbf{r}}_{r,u}\|^2 - 2 \bar{\mathbf{r}}_r^j \cdot \bar{\mathbf{r}}_{r,u} \\ &\approx \|\bar{\mathbf{r}}_r^j\|^2 \left( 1 - 2 \frac{\bar{\mathbf{r}}_r^j \cdot \bar{\mathbf{r}}_{r,u}}{\|\bar{\mathbf{r}}_r^j\|^2} \right), \text{ neglecting the higher order term} \end{aligned} \quad (\text{B.1.4})$$

Then using the relationship  $\sqrt{1-2x} \approx 1-x$ , if  $x$  is small, we have

$$\|\bar{\mathbf{r}}_u^j\| = \|\bar{\mathbf{r}}_r^j\| \left( 1 - \hat{\mathbf{r}}_r^j \cdot \frac{\bar{\mathbf{r}}_{r,u}}{\|\bar{\mathbf{r}}_r^j\|} \right) \quad (\text{B.1.5})$$

or

$$\frac{1}{\|\bar{\mathbf{r}}_u^j\|} = \frac{1}{\|\bar{\mathbf{r}}_r^j\|} \left( 1 + \hat{\mathbf{r}}_r^j \cdot \frac{\bar{\mathbf{r}}_{r,u}}{\|\bar{\mathbf{r}}_r^j\|} \right) \quad (\text{B.1.6})$$

Substitute this expression into Equation (B.1.2), the error of LADGPS correction is

$$\varepsilon_L = \Delta \mathbf{r}^j \cdot \left\{ \frac{\bar{\mathbf{r}}_u^j}{\|\bar{\mathbf{r}}_r^j\|} + \frac{\bar{\mathbf{r}}_u^j}{\|\bar{\mathbf{r}}_r^j\|} (\hat{\mathbf{r}}_r^j \cdot \frac{\bar{\mathbf{r}}_{r,u}}{\|\bar{\mathbf{r}}_r^j\|}) - \frac{\bar{\mathbf{r}}_r^j}{\|\bar{\mathbf{r}}_r^j\|} \right\} + v_u^j - v_r^j \quad (\text{B.1.7})$$



$$\begin{aligned}
&\approx \Delta \mathbf{r}^j \cdot \frac{1}{\|\bar{\mathbf{r}}_r^j\|} \left\{ -\bar{\mathbf{r}}_{r,u} + (\hat{\mathbf{l}}_r^j \cdot \bar{\mathbf{r}}_{r,u}) \hat{\mathbf{l}}_r^j \right\} + v_u^j - v_r^j \\
&= -\frac{\Delta \mathbf{r}^j \cdot \bar{\mathbf{d}}}{\|\bar{\mathbf{r}}_r^j\|} + v_u^j - v_r^j
\end{aligned}$$

where  $\bar{\mathbf{d}}$  is the projection of  $\bar{\mathbf{r}}_{r,u}$  onto the reference station LOS (see Figure B.1.1).

Therefore the error of LADGPS correction due to the satellite location error is proportional to the vector  $\bar{\mathbf{d}}$ . The worst case ranging error occurs when the unit vector to the satellite is perpendicular to the baseline vector ( $\bar{\mathbf{d}} = \bar{\mathbf{r}}_{r,u}$ ) and the satellite ephemeris error vector is parallel to the baseline vector ( $\Delta \mathbf{r}^j \cdot \bar{\mathbf{d}} = |\Delta \mathbf{r}^j| |\bar{\mathbf{d}}|$ ). For a 10 meter ephemeris error, the worst case ranging error for 100 km and 200 km baselines are 5 cm and 10 cm, respectively.

To find the variance of the error, we assume

$$E[\Delta \mathbf{r}^j] = 0 \quad (\text{B.1.8})$$

$$\text{Var}[\Delta \mathbf{r}^j] = W \quad (\text{B.1.9})$$

$$\text{Var}[v_u^j] = \text{Var}[v_r^j] = V \quad (\text{B.1.10})$$

Finally the variance of the local area differential correction variance due to errors in the satellite location can be expressed as

$$\text{Var}[\varepsilon_L] = E[\varepsilon_L^2] = \frac{E[(\Delta \mathbf{r}^j \cdot \bar{\mathbf{d}})^2]}{\|\bar{\mathbf{r}}_r^j\|^2} + 2V = \frac{W}{2 \|\bar{\mathbf{r}}_r^j\|^2} \|\bar{\mathbf{d}}\|^2 + 2V \quad (\text{B.1.11})$$

where the factor 2 in the denominator accounts for the statistical expectation value of the inner product  $\Delta \mathbf{r}^j \cdot \bar{\mathbf{d}}$ . Equation (B.1.11) is the one used for LADGPS covariance analysis in Chapter 2.

## B.2 WADGPS Correction Error Analysis

The WADGPS actually estimates the satellite location and sends it to the user. Therefore, the error in the WADGPS correction for a pseudorange between satellite  $j$  and user  $u$  can be expressed as

$$\begin{aligned}\varepsilon_w &= (G_u x^j + v_u^j) - G_u \hat{x}^j \\ &= G_u (x^j - \hat{x}^j) + v_u^j\end{aligned}\tag{B.2.1}$$

where  $x^j = [\Delta r^j \ B^j]^T$  is the vector containing true satellite location error ( $\Delta r^j$ ) and clock bias ( $B^j$ ), and  $\hat{x}^j$  is the wide area estimation of  $x^j$ .  $G_u$  is the observation matrix that projects the error or the estimate to the user's line-of-sight,  $G_u = [\hat{\mathbf{1}}_u^{jT} \ 1]_{1 \times 4}$ , and  $v_u^j$  is the user's measurement noise.

To calculate the differential correction errors for the user, we need to know the WADGPS corrections first. In this analysis, we used only three reference stations and therefore the minimum-norm estimate of the wide area location error for satellite  $j$  can be calculated using the pseudorange residual  $z_r^j = G_r x + v_r^j$  where  $G_r$  is observation matrix, and the state vector  $x^j = [\Delta r^j \ B^j]^T$  (the result justifies this geometric approach). The minimum-norm solution of the state is

$$\hat{x}^j = G^+ z = G_r^T (G_r G_r^T)^{-1} z_r^j\tag{B.2.2}$$

To find the variance of correction residual, we further assume

- (1) The user measurement noise and variance are  $E[v_u^j] = 0$  and  $\text{var}[v_u^j] = \sigma^2$ ,
- (2) Each of the wide area reference stations has equal measurement noise and variances, and they are  $E[v_r^j] = 0$  and  $\text{var}[v_r^j] = V_r$ , and
- (3)  $E[\varepsilon_w] = 0$

Then the variance of  $\varepsilon_w$  is

$$\text{var}[\varepsilon_w] = E[\varepsilon_w^2] = G_u P_{x-\hat{x}} G_u^T + \sigma^2\tag{B.2.3}$$

where

$$P_{x-\hat{x}} = E[(x^j - \hat{x}^j)(x^j - \hat{x}^j)^T]\tag{B.2.4}$$

$$= E\left[x^j x^{jT}\right] + E\left[\hat{x}^j \hat{x}^{jT}\right] - 2E\left[x^j \hat{x}^{jT}\right]$$

Since

$$E\left[x^j \hat{x}^{jT}\right] = E\left[x^j z G^+\right] \quad (B.2.5)$$

then

$$\begin{aligned} P_{x-\hat{x}} &= W + E\left[G^+ z z^T G^{+T}\right] - 2E\left[x^j z G^+\right] \quad (B.2.6) \\ &= W + E\left[G^+ (G_r x^j + v_r^j) (G_r x^j + v_r^j)^T G^{+T}\right] - 2E\left[x^j (G_r x^j + v_r^j) G^+\right] \\ &= W + E\left[G^+ G_r x x^T G_r^T G^{+T}\right] + E\left[G^+ v_r^j v_r^{jT} G^{+T}\right] - 2E\left[x^j x^{jT} G_r G_r^+\right] \\ &= W + G^+ G_r W G_r^T G^{+T} - 2W G_r G_r^+ + G^+ V G^+ \\ &= (I - G^+ G_r) W (I - G^+ G_r)^T + G^+ V G^+ \end{aligned}$$

Substituting into Equation (B.2.3), the WADGPS variance due to errors in the satellite location becomes

$$Var[\varepsilon_w] = G_u \left[ (I - G^+ G_r) W (I - G^+ G_r)^T + G^+ V G^+ \right] G_u^T + \sigma^2 \quad (B.2.7)$$

### B.3 Covariance Analysis

For the purpose of the covariance analysis, a three reference station network is set up to estimate the location error and clock bias of one satellite. Then the pseudorange error variances for a grid of users are calculated using Equations (B.1.11) and (B.2.7) for LADGPS and WADGPS corrections, respectively. The result is presented in Section 2.1 for comparison.

## Appendix C

# Tropospheric Delay Model

The troposphere creates a delay in the GPS pseudorange. The total line of sight tropospheric delay can be calculated by the line integral from satellite ( $s$ ) to receiver ( $r$ ):

$$\Delta t_{\tau} = \int_s^r \left( \frac{ds}{V} - \frac{ds}{C} \right) = \frac{1}{C} \cdot \int_s^r (n - 1) ds \quad \text{seconds, or}$$

$$\tau = C \cdot \Delta t_{\tau} \quad \text{meters}$$

where

$n$  is index of refraction of atmosphere,  $n > 1$  for the troposphere,

$V$  is the actual signal velocity in the troposphere,  $V = \frac{C}{n}$ , and

$C$  is the speed of light in the vacuum.

Note that in order to avoid confusion, I use script  $\tau$  to represent the tropospheric delay and  $T$  to represent the temperature that will be used later in this appendix.

### C.1 Model

By defining atmospheric refractivity  $N = 10^6 (n - 1)$ , the line-of-sight tropospheric delay becomes

$$\tau = 10^{-6} \cdot \int_s^r N ds \quad (\text{C.1.1})$$

A widely used formula for the atmospheric refractivity  $N$  is that it comprises dry ( $N_d$ ) and wet ( $N_w$ ) components [Smith and Weintraub, 1953], i.e.,

$$N = N_d + N_w \quad (\text{C.1.2})$$

or

$$\tau = 10^{-6} \cdot \left( \int_s^r N_d ds + \int_s^r N_w ds \right) = \tau_d + \tau_w \quad (\text{C.1.3})$$

Their expression separates the tropospheric delay into two components: the dry part and the wet part. The dry part is mainly contributed by the gas molecules in the atmosphere and constitute 85 to 90% of the total tropospheric effect. As modeled by the perfect gas law and assuming hydrostatic equilibrium, the dry component is highly predictable and can be estimated accurately. Given surface pressure measurement accurate to 0.3 mbar or better, it is usually possible to predict the dry delay to better than 1 mm. However, the wet delay is proportional to the perceptible water vapor in the atmosphere *on the average*, and only models of the mean value of the wet delay are available—the variation on top of the average needs to be treated as a stochastic process. As a rule of thumb, the zenith dry delay is usually 2.3 m in normal atmospheric conditions, and the zenith wet delay can be as large as 35 cm in very humid weather. Note that the above expression is valid for frequencies up to 30 GHz (GPS broadcasts at about 1.5 GHz ) [Hopfield, 1971, Black, 1978, Black and Eisner, 1984]. Smith/Weintraub expressed the dry term as

$$N_d = 77.6 \frac{P}{T} \quad (\text{C.1.4})$$

and the wet term as

$$N_w = 3.73 \times 10^5 \left( \frac{e}{T^2} \right) \quad (\text{C.1.5})$$

where

$P$  = total pressure, milibars,

$T$  = temperature, Kelvin, and

$e$  = partial pressure of the water vapor, mbar.

To calculate the tropospheric delay from the above equations, one needs to know the profiles of  $N_d$  and  $N_w$  in terms of altitude. These profiles are generally hard to obtain, especially for real-time use. Fortunately, Hopfield [1969] derived an altitude profile for dry refractivity and an analogous expression for the wet term within the troposphere. Hopfield calculates the dry refractivity in terms of surface value refractivity,  $N_d^{(s)}$ , and a quartic function of altitude, that is,

$$N_d = N_d^{(s)} \left[ \frac{r_d - r}{r_d - r_s} \right]^4 \quad r_s \leq r \leq r_d \quad (\text{C.1.6})$$

where

$r_d$  = the radius of the top of the troposphere from the center of the Earth

$r_s$  = the radius of the Earth surface, and

$r_d - r_s \equiv h_d$  is the thickness of the troposphere.

This expression was derived under 1) linear decreasing of temperature with altitude at lapse rate around  $6.71^\circ/\text{km}$ , 2) the perfect gas law and 3) the Smith/Weintraub expressions.

## C.2 Implementation

The computation of the tropospheric delay dry and wet components used at Stanford WAAS is summarized in the following discussions.

### C.2.1 Dry Component

Using Equation (C.1.7), the dry delay can be written as

$$\tau_d = 10^{-6} \frac{N_d^{(s)}}{h_d^4} \int_0^L (r_d - r)^4 ds \quad (\text{C.2.1})$$

where  $L$  is the length of the line-of-sight segment in the troposphere. Referring to the geometry shown in Figure C.2.1, we can express the LOS path as

$$s = [r^2 - r_s^2 \cos^2(el)]^{1/2} - r_s \cos(el) \quad (\text{C.2.2})$$

Then the differential path is

$$ds = r dr / [r^2 - r_s^2 \cos^2(el)]^{1/2} \quad (\text{C.2.3})$$

By changing the variable, the dry delay is

$$\tau_d = 10^{-6} \frac{N_d^{(s)}}{h_d^4} \int_{r_s}^{r_d} \frac{(r_d - r)^4}{[r^2 - r_s^2 \cos^2(el)]^{1/2}} r dr \quad (\text{C.2.4})$$

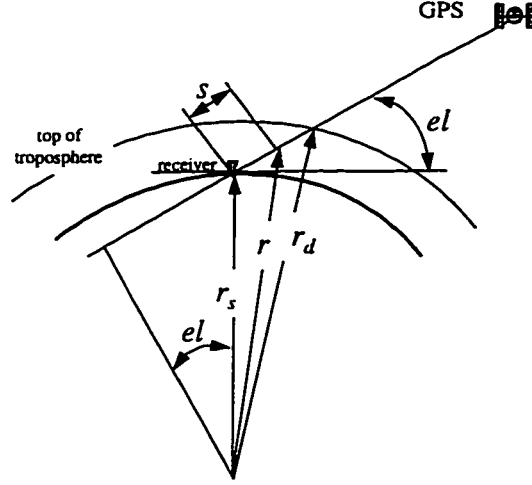


**Figure C.2.1 Geometry of Tropospheric Delay**

Letting  $\rho = \frac{r_d - r}{h_d}$  with  $\rho(r = r_d) = 0$  and  $\rho(r = r_s) = 1$  and changing the variable again,

we have

$$\tau_d = 10^{-6} N_d^{(s)} h_d \int_0^1 \frac{\rho^4 d\rho}{\sqrt{1 - [\cos(el) / [1 + (1 - \rho) h_d / r_s]]^2}} \quad (C.2.5)$$

Since  $(1 - \rho) h_d / r_s < 46 \text{ km} / 6478 \text{ km} = 7 \times 10^{-3}$  ( $h_d \approx 46 \text{ km}$ ), one can approximate it as a constant. The dry delay has an expression similar to the ionosphere delay, that is LOS delay is equal to the vertical delay at zenith direction times an obliquity factor:

$$\tau_d = 10^{-6} \frac{N_d^{(s)} h_d}{5} \cdot M_d(el) = \tau_{d,z} \cdot M_d(el) \quad (C.2.6)$$

where  $\tau_{d,z}$  is the tropospheric ‘dry’ delay in the zenith direction and  $M_d(el)$  is the obliquity factor for conversion from slant (LOS) delay to vertical (zenith) delay.

If we neglect the small term  $(1 - \rho) h_d / r_s$ , the obliquity factor can be simplified to an expression commonly cited:

$$M_d(el) = \frac{1}{\sqrt{1 - [\cos(el) / [1 + (1 - \rho) h_d / r_s]]^2}} \cong \frac{1}{\sin(el)} \quad (C.2.7)$$

In her paper, Hopfield [1971] also derived an expression for the thickness of the troposphere,

$$h_d = 148.98 (T - 4.12) \text{ meters} \quad (\text{C.2.8})$$

Putting together all the components

$$\begin{aligned} \tau_d &= \tau_{d,z} \cdot M_d(el) \\ &= \frac{10^{-6} \cdot 77.6}{5} \frac{P^{(s)}}{T} \cdot h_d \cdot M_d(el) \\ &= 1.552 \times 10^{-5} \frac{P^{(s)}}{T} \cdot h_d \cdot M_d(el) \end{aligned} \quad (\text{C.2.9})$$

where  $P^{(s)}$  is the surface pressure in mbar.

### C.2.2 Wet Component

Using the same altitude profile for  $N_w$  and from Equations (C.1.3) and (C.1.5), the integral of wet delay can be written as

$$\tau_w = 3.73 \times 10^{-1} \cdot \frac{1}{5} \cdot \frac{e}{T^2} h_w \cdot M_d(el), \text{ or} \quad (\text{C.2.10})$$

$$\tau_w = 7.46 \times 10^{-2} \cdot \frac{e}{T^2} h_w \cdot M_w(el) \quad (\text{C.2.11})$$

where  $h_w \approx 13000 \text{ m}$ .

The water vapor pressure in the formula can be calculated using its surface measurement and relative humidity as

$$e = e_s \cdot \frac{RH}{100} \quad (\text{C.2.12})$$

where  $e_s = \text{saturated water vapor pressure}$  is calculated using the following equations [Stull, 1995]:

$$\begin{aligned} e_s &= e_o \exp \left[ \frac{(T - T_1)}{T - T_2} \right] \\ &= 0.611 \cdot \exp \left[ \frac{17.2694 (T - 273.16)}{T - 35.86} \right] \text{ kpa} \\ &= 6.11 \cdot \exp \left[ \frac{17.2694 (T - 273.16)}{T - 35.86} \right] \text{ mbar} \end{aligned} \quad (\text{C.2.13})$$

For simplicity, we chose to use  $M_w(el) = M_d(el)$ .



# Appendix D

## Dual-Frequency Carrier-Smoothing

### Algorithm

A carrier-smoothing algorithm was proposed by Hatch [1982] to take advantage of the low noise characteristic in the GPS carrier-phase measurements and to smooth the noisy and multipath-affected pseudoranges. His original work applied to single-frequency measurements. The basic concept can also be applied to dual-frequency measurements with some improvements. Dual-frequency smoothing further eliminated the “ionospheric divergence” between the two measurements and therefore can achieve longer smoothing time constant and smoother results. This appendix describes the dual-frequency carrier-smoothing algorithm that is used at the Stanford Master Station.

#### D.1 Introduction

In Hatch’s paper, the smoothing filter for the pseudorange ( $PR$ ) at epoch  $k$  was expressed as

$$\hat{PR}_{k+1} = \frac{k}{k+1} (\hat{PR}_k + \Delta\phi_{k+1}) + \frac{1}{k} PR_k \quad (\text{D.1.1})$$

where  $\hat{PR}_{k+1}$  is the smoothed pseudorange,

$\Delta\phi_{k+1} = \phi_{k+1} - \phi_k$  is the increment of carrier phase, and

$PR_k$  is the pseudorange measurement.

This smoothing formula uses the increment in carrier-phase to predict the pseudorange and the weighting factor  $\frac{k}{k+1}$  approaches unity as  $k$  grows. Therefore, as time progresses, the smoothing result relies on the increment of carrier-phase more and becomes smoother.

This formula can be derived from a Kalman filter and measurement equation approach. The Kalman filter further provides the confidence number, or the covariance matrix, of the smoothing result. One Kalman filter which leads to exactly the same smoothing formula can be described as follows [Gazit, 1996].

This derivation uses a first order system equation and achieves the same form of Equation (D.1.1) by treating  $\Delta\phi_{k+1}$  as the control input, instead of a measurement. That is, in the Kalman filter notation, the system and measurement equations are

$$x_{k+1} = \Phi x_k + \Gamma u_{k+1} + w_k \quad (D.1.2)$$

$$z_k = Hx_k + v_k \quad (D.1.3)$$

where  $x_k = PR_k$ , the raw pseudorange

$u_k = \Delta\phi_k$ , the difference between two carrier phase measurements

$w_k$  is the noise on  $\Delta\phi_k$ , with variance  $W_k = 2\sigma_\phi$ , or twice the measurement noise of carrier-phase

$v_k$  is the pseudorange measurement noise, with variance  $V_k = \sigma_{PR}^2$ , and

$\Phi = \Gamma = H = 1$ .

The Kalman filter measurement update equations are

$$K_k = \hat{P}HV^{-1} = \bar{P}_k H^T [V + H\bar{P}_k H^T]^{-1} = \frac{\bar{P}_k}{\bar{P}_k + V} \quad (D.1.4)$$

$$\hat{x}_k = \bar{x}_k + K_k [z_k - H \bar{x}_k] = \bar{x}_k + K_k [z_k - \bar{x}_k] \quad (D.1.5)$$

$$\hat{P}_k = \bar{P}_k - K_k H \bar{P}_k = \bar{P}_k - K_k \bar{P}_k = \frac{V \bar{P}_k}{\bar{P}_k + V} \quad (D.1.6)$$

and the time update equations are

$$\bar{x}_{k+1} = \Phi \hat{x}_k + \Gamma u_{k+1} = \hat{x}_k + \Delta\phi_{k+1} \quad (D.1.7)$$

$$\bar{P}_{k+1} = \Phi \hat{P}_k \Phi^T + W = \hat{P}_k + W \quad (D.1.8)$$

Substituting Equation (D.1.7) into (D.1.5), we have

$$\begin{aligned} \hat{x}_k &= (1 - K_k) \hat{x}_{k-1} + (1 - K_k) \Delta\phi_k + K_k z_k \\ &= (1 - K_k) (\hat{x}_{k-1} + \Delta\phi_k) + K_k z_k \end{aligned} \quad (D.1.9)$$

If  $W \ll V$ , and  $\bar{P}_0 = V$ , then the Kalman gain ( $K_k$ ) will take a schedule as

$$K_1 = \frac{1}{2}, K_2 = \frac{1}{3}, K_3 = \frac{1}{4} \dots$$

Together with Equation (D.1.9), we have derived the Hatch carrier-smoothing filter using Kalman filter formulation. Furthermore, the variance of this smoothing is also derived, which is necessary in the propagation of errors in the WMS data processing. Note that because of the ionospheric divergence problem between the carrier and pseudorange, the smoothing constant,  $k$  in Equation (D.1.1), is limited to 50 to 100 in practice [Chou, 1992]. Hence, the effectiveness of the smoothing is limited. Furthermore, Gazit showed that for  $W/V = 0.012$ , the steady state Kalman gain can be shown to be

$$K_{ss} = -\frac{W}{2V} + \sqrt{\left(\frac{W}{V}\right)^2 + 4\frac{W}{V}} = 0.02 \quad (\text{D.1.10})$$

which is equivalent to limiting the Hatch smoothing constant to 50. This number is commonly used in single-frequency smoothing to avoid the ionosphere divergence problem.

## D.2 Stanford's WMS Dual-Frequency Carrier-Smoothing Algorithm

As discussed in Chapter 2, the dual-frequency smoothing approach effectively eliminates the divergence problem between the carrier-phase and pseudorange. Stanford's WMS implements the Hatch filter with the smoothing variance derived from the Kalman filter. The estimate is expressed in the following form.

$$\hat{x}_k = (1 - L_k)(\hat{x}_{k-1} + \Delta\phi_k) + L_k z_k$$

where the gain  $L_k$  is calculated as

$$L_k = \frac{w_k}{\sum_{i=1}^{k-1} w_i + w_k}$$

and the weighting  $w_k$  is the inverse of pseudorange noise variance or  $w_k = 1/\sigma_k^2$

The variance (or the confidence) is calculated as

$$\hat{P}_k = \bar{P}_k - K_k \bar{P} = \bar{P}_k - \frac{\bar{P}_k}{V + \bar{P}} \text{ and } \bar{P}_{k+1} = \hat{P}_k + W$$

where process noise variance  $W$  is added to account for the variation of the states.

In the design of the filter, the most important factor is the determination of pseudorange measurement noise. Currently, the pseudorange measurement noise is calculated using the formula similar to the one stated in WAAS MOPS Appendix E (WAAS MOPS):

$$\sigma^2 = \sigma_{DC}^2 + \frac{\sigma_{m45}^2}{\tan^2(el)} + \sigma_{SNR}^2 \quad (D.2.1)$$

This expression assumes the pseudorange measurement is composed of three parts: 1) a noise floor ( $\sigma_{DC}^2$ ), 2) an elevation dependent multipath error, and 3) an signal-to-noise-ratio (SNR) related receiver tracking error. In general, at low elevation, the signal strength is weaker due to the antenna gain pattern and atmospheric signal degradation, therefore it is harder to track the signal, leading to more errors. More specifically, the Equation (D.2.1) is

$$\sigma^2 = \sigma_{DC}^2 + \frac{\sigma_{m45}^2}{\tan^2(el)} + [\sigma_{AMP} \exp(-C \cdot SNR)]^2 \quad (D.2.2)$$

We derive different parameters of the  $\sigma^2$  curve for each reference station according to the real measurements. The input measurements of the dual-frequency carrier smoothing are:

$$I_{L1,PR} \equiv \frac{PR_{L2} - PR_{L1}}{\gamma - 1} = I_{L1} + v_{PR} \quad (D.2.3)$$

$$I_{L1,\phi} \equiv \frac{\phi_{L1} - \phi_{L2}}{\gamma - 1} = I_{L1} + Amb + v_{\phi} \quad (D.2.4)$$

$$I_{L1,L1} \equiv \frac{PR_{L1} - \phi_{L1}}{2} = I_{L1} - \frac{N_1 \lambda_1}{2} + v_{L1} \quad (D.2.5)$$

where  $I_{L1}$  is the ionospheric delay at the  $L_1$  frequency, and the extra subscripts represent the observables used in the combination,  $Amb$  represents the combination of ambiguities from the  $L_1$  and  $L_2$  carrier phases, and  $v_{PR}^2 = \sigma^2$  calculated above (see also Chapter 2). As shown in Figure D.2.1, the filter estimates the smoothed ionospheric delay  $\hat{I}_{1,smth}$  and the ionospheric-free pseudorange,  $\hat{PR}_{L1}$ . The first step in the implementation is to smooth  $I_{L1,PR}$  by the low-noise  $I_{L1,\phi}$  and produce  $\hat{I}_{1,smth}$  and its confidence. Then

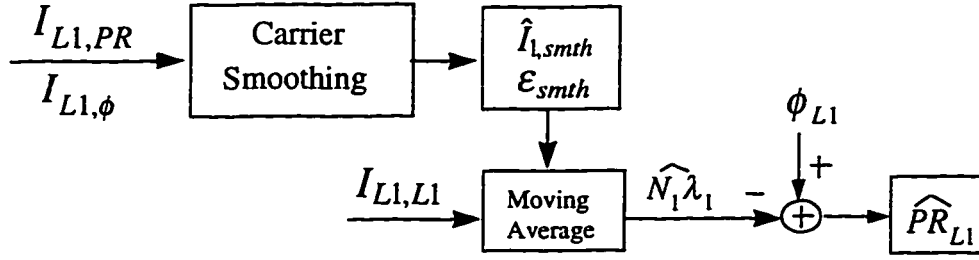


**Figure D.2.1 Dual-frequency Smoothing of Ionospheric Delays and Pseudoranges**

combining  $\hat{I}_{l,smth}$  and Equation (D.2.5), we can estimate  $N_1\lambda_1$  by the moving average estimator. Finally, substituting  $\hat{I}_{l,smth}$  and  $N_1\lambda_1$  into the L1 carrier phase, Equation 2.3.3), we obtain the estimate of smoothed ionosphere-free pseudorange  $\hat{PR}_{L1}$ . Figure D.2.2 presents one of the smoothing results. The dual-frequency smoothing technique has two significant advantages over the single-frequency smoothing: 1) The ionosphere divergence between code-phase and carrier-phase measurements is completely avoided. As the filter converges with time, the multipath problem will be minimized. 2) Cycle slips can be easily detected and patched because of the slow variation of the physical ionosphere.

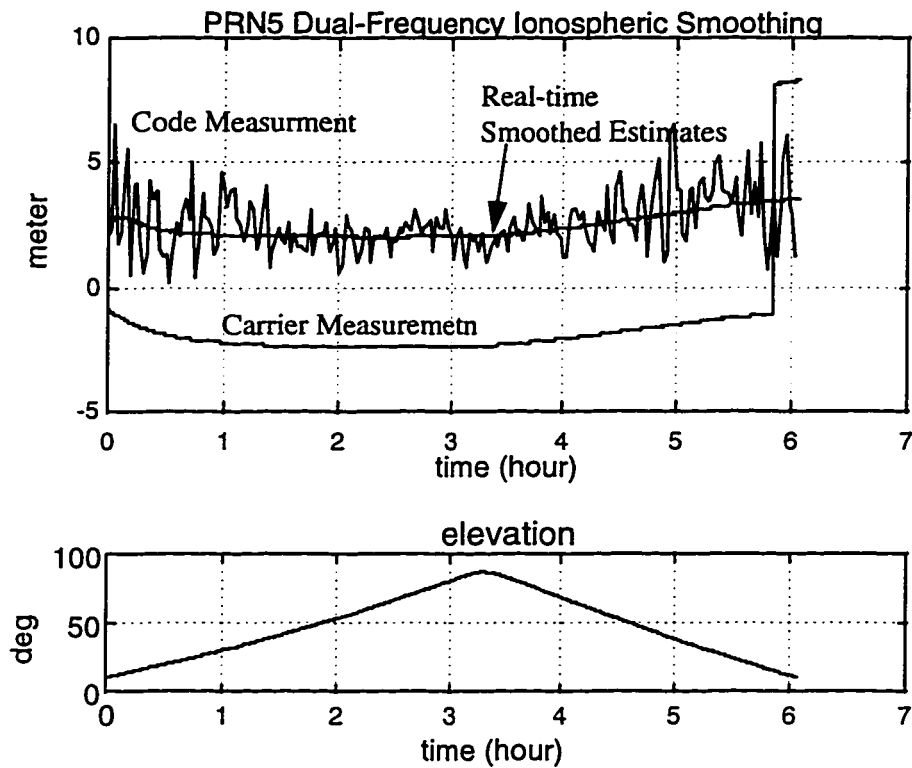


**Figure D.2.2 Dual-frequency Smoothing Result**

After 15 to 20 minutes, the filter converges and the smoothed result has noise at the 10-cm level. The carrier measurement is biased by carrier phase ambiguity and is presented close to zero in order to view easily. The jump of the carrier phase is not an exact integer but is adjusted to fit into the plot to show the existence of cycle slips.

# Appendix E

## Master Clock Estimation

This appendix presents an algorithm to estimate the master clock in the WAAS network. Since the estimated satellite clock biases still include the master clock term, the Wide Area Master Station (WMS) needs to subtract the estimate of the master clock from them in order to keep the fast clock corrections within the WAAS message Type 2 quantization range (Chapter 2).

We assume each GPS receiver at Wide Area Master Stations (WRS) is connected to a high quality Rubidium (Rb) oscillator. The measurements of the master clock at a stand-alone WRS are error-corrupted pseudoranges, and the satellite Selective Availability is the dominating error source. In general, the behavior of the Rb oscillator is quite stable and can be assumed to be linear for several hours; that is the master clock is modeled as

$$b_M = a_0 + a_1 \cdot \Delta t \quad (\text{E.1})$$

The design of this estimator is not trivial, particularly under the effects of SA, to ensure a smooth result, the estimator needs to satisfy the following two requirements:

1. The result, which should not diverge due to SA, has to keep track of the variation of the Rubidium (Rb) oscillator. The variation of the oscillator can be caused both by the drift of the oscillator frequency and by the variation of the power source.
2. When the number of satellites in view changes or the receiver clock millisecond resets, the estimator should be able to minimize the jumpiness in the clock estimates.

To meet the requirements, an algorithm which takes advantage of both the recursive least-squares (RLS) and the moving average (MA) was devised. Note that we did not choose the Kalman filter approach because it needs many hours to extract the clock parameters from the SA-corrupted measurements. In contrast, RLS can efficiently initialize the linear parameters of the Rb clock within half an hour.

The measurements of the master clock ( $b_M$ ) are pseudorange residuals,  $\Delta PR_M^j$ ,

$$\Delta PR_M^j = PR_M^j - \rho_M^j \approx -SA^j + b_M + \varepsilon_M^j, \quad j=1 \dots N \quad (E.2)$$

where  $N$  is the total number of satellites in view. For satellites without SAs, the numerical values of broadcast User Range Accuracy (URAs) are four meters in the pseudorange accuracy. This accounts for satellite location errors in the orbit estimation. For those with SAs on, the URAs have a pseudorange uncertainty of 32 meters. To take advantage of this information, the filter uses URAs as the weights, i.e.,

$$z = \bar{b} = \frac{\sum_{j=1}^N w_j \cdot \Delta PR_M^j}{\sum_{j=1}^N w_j}, \quad (E.3)$$

where

$$w_j = 1/URA_j^2$$

Furthermore, to prevent jumpiness caused by rising/setting satellites, the weight of the low elevation satellite,  $w_i$ , is further modified by

$$w_j = \frac{w_j}{2^{0.6(12-el)}} \text{ if } el \leq 12^\circ \quad (E.4)$$

in order to smoothly transit the contribution of that satellite.

With the above measurements, WMS uses the following procedures, shown in computer pseudo-code, to estimate the master clock in the network:

**[pseudo-code of the master clock estimator]:**

IF [ (estimator initialization) OR (millisecond reset) ]

*Reset the clock to the raw measurement  $\bar{b}$ , but keep the previously estimated slope  $\hat{a}_1$ ,  
Augment the uncertainty of the clock  
Reset parameter  $w\_sum=0$*



ELSE IF [ ( $t\_elapsed < RLS\_TIME$ ) OR ( $w\_sum < MAX\_W\_SUM$ ) ]

*RLS estimator for  $\hat{a}_0$  and  $\hat{a}_1$*

ELSE

*MA estimator for  $\hat{a}_0$  and  $\hat{a}_1$*

Note that MA estimator is not implemented until the first convergent RLS estimates are reached. The purpose of MA is to keep track of the changing slope, which may be due to the drift of the oscillator frequency and/or to the instability of the oscillator's power source.

The RLS estimator measurement updates of the state and covariance matrix are

$$\hat{x}_k = \bar{x}_k + \hat{P}_k H^T V_k^{-1} (y_k - H \bar{x}_k) \quad (E.5)$$

$$\hat{P}_k = (\bar{P}_k^{-1} + H^T V_k^{-1} H)^{-1} = \bar{P}_k - \bar{P}_k H^T (V_k + H \bar{P}_k H^T)^{-1} H \bar{P}_k \quad (E.6)$$

where  $x = [a_0 \ a_1]^T$  is the clock parameter at the initial epoch ( $t_0$ ) and the current clock is calculated by  $\hat{b}_k = \hat{a}_0 + \hat{a}_1 \cdot (t_k - t_0)$ .

The MA estimator, which estimates the current clock states, can be formulated as following: first the clock parameters are written in the moving-average regressive form as

$$\hat{a}_{0,i} = \frac{k-1}{k} \hat{a}_{0,i-1} + \frac{1}{k} a_{0,i} \quad (E.7)$$

$$\hat{a}_{1,i} = \frac{k-1}{k} \hat{a}_{1,i-1} + \frac{1}{k} a_{1,i}, \quad (E.8)$$

Then the MA estimator of the clock is expressed in terms of the previous state as

$$\hat{b}_i = \hat{a}_{0,i} + \hat{a}_{1,i} \cdot (t_i - t_0) \quad (E.9)$$

$$\begin{aligned} &= \left( \frac{k-1}{k} \hat{a}_{0,i-1} + \frac{1}{k} a_{0,i} \right) + \left( \frac{k-1}{k} \hat{a}_{1,i-1} + \frac{1}{k} a_{1,i} \right) \cdot (t_i - t_0) \\ &= \frac{k-1}{k} \{ \hat{a}_{0,i-1} + \hat{a}_{1,i-1} \cdot (t_i - t_0) \} + \frac{1}{k} \{ a_{0,i} + a_{1,i} \cdot (t_i - t_0) \} \\ &= \frac{k-1}{k} \{ \hat{a}_{0,i-1} + \hat{a}_{1,i-1} \cdot [(t_{i-1} - t_0) + (t_i - t_{i-1})] \} + \frac{1}{k} \{ a_{0,i} + a_{1,i} \cdot (t_i - t_0) \} \end{aligned}$$

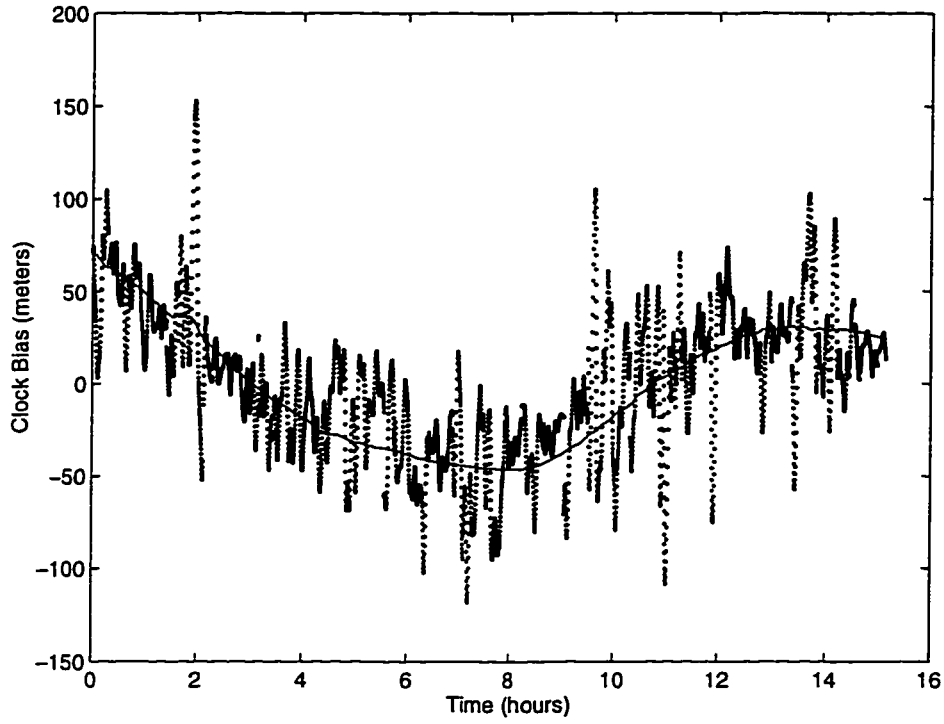


**Figure E.1 Master Clock Estimation**

The dashed line is the clock bias measurement and the solid line is the estimation result. Data is from the Stanford TRS Trimble 4000 SSE receiver with external Rubidium oscillator connected as the receiver clock.

or

$$\hat{b}_i = \frac{k-1}{k} \left\{ \hat{b}_{i-1} + \hat{a}_{1,i-1} \cdot \Delta t \right\} + \frac{1}{k} \bar{b}_i$$

where

$\Delta t$  is the sampling time, and

$\bar{b}_i$  is the raw measurement, as expressed in Equation (E.3).

An example of the master clock estimation is shown in Figure E.1.

# Appendix F

## Ionospheric Delay

### F.1 Code and Carrier Divergence

This section presents the derivation of GPS ionospheric effects. These cause the delay in the code phase and the advance in the carrier phase by equal magnitude but opposite sign. This is a direct result of the ionosphere being a dispersive medium with the group delays of the ionosphere proportional to  $1/f^2$ .

As the GPS signal travels through the ionosphere, it is refracted and propagates at a different speed than the speed of light in the vacuum because of the free electron density in the ionosphere. The time difference introduced by the ionosphere can be expressed as:

$$\Delta t_I = \int_s^r (dl/v - dl/c) = \frac{1}{c} \int_s^r (n - 1) ds, \quad \text{since } v = \frac{c}{n} \text{ and } n \neq 1 \quad (\text{F.1.1})$$

where  $c$  is the speed of light,  $v$  is the actual signal propagation speed,  $n$  is the index of refraction of the medium. The integration is along the path from the satellite ( $s$ ) to the receiver ( $r$ ). When multiplied by the speed of light, the ionospheric time delay in terms of distance is

$$I = c \cdot \Delta t_I \quad \text{meters} \quad (\text{F.1.2})$$

Under this expression, the ionospheric effect is:

$I > 0$  if  $I$  is a delay in the signal, and

$I < 0$  if  $I$  is an advance in the signal (F.1.3)

An information-bearing signal, such as the GPS signal, normally has a small spread of frequency (sidebands) around a high carrier frequency. Such a signal comprises a “group” of frequencies and forms a wave packet. The group velocity is the velocity of propagation of the wave packet envelope and the phase velocity is the carrier propagation

velocity. To use Equation (F.1.2) to calculate the ionospheric effects on both carrier (traveling at phase velocity) and information (traveling at group velocity), we need to calculate the index of refraction of the ionosphere that both carrier and information experienced.

From electro-magnetic (EM) wave theory, Appleton and Hartree derived a theoretical expression for the index of refraction [Hargreaves, 1992]. Although this equation is complicated, the expression is greatly simplified in the GPS frequency range, i.e.,

$$n_{\phi}^2 \cong 1 - X \quad (\text{F.1.4})$$

for the first order approximation, and

$$X = \frac{80.6}{f^2} N_e \quad (\text{F.1.5})$$

where  $N_e$  is the free electron density in the ionosphere and  $f$  is the carrier frequency.

Then

$$n_{\phi} = 1 - \frac{X}{2}, \text{ and}$$

$$I_{\phi} = \int_s^r (n_{\phi} - 1) ds = -\frac{40.3}{f^2} \int_s^r N_e ds < 0$$

Also, from EM wave theory, the index of refraction of the information is

$$n_g = n_{\phi} + f \frac{\partial n_{\phi}}{\partial f} = 1 + \frac{X}{2}, \text{ and}$$

$$I_g = \int_s^r (n_g - 1) ds = \frac{40.3}{f^2} \int_s^r N_e ds > 0$$

Therefore, the ionosphere created a delay in the code-phase measurement (where the information is) and an advance in the carrier-phase measurement. The delay and the advance are exactly the same but in opposite directions. This phenomenon is usually called “code-carrier divergence” in the GPS literature and is presented in the GPS measurement equations in Chapter 3. Note that this “divergence” between the code and carrier poses a limit on the ‘single-frequency’ smoothing time constant. However, the dual-frequency smoothing algorithm presented in Chapter 3 does not contain the

divergence anymore and therefore allows for a long time constant, up to several hours. Also note that the above derivation is the first order approximation. Even though the first order term contains most of the ionospheric effect, researchers have shown the second order term can have up to a 10-cm effect and have observed some discrepancies in the high-accuracy geophysics applications [Bassiri et al., 1993, Parkinson et al., 1996].

## F.2 Klobuchar Thin Slab Vertical Delay Model

Klobuchar devised a thin slab ionospheric model in 1986 for GPS single-frequency users, which this is widely available through the GPS navigation message [Klobuchar, 1986]. This model approximates the ionosphere as a condensed thin slab centered at 350 km above the earth's surface. The ionospheric vertical time delay at elevation 90° in the L1 pseudorange is modeled by a raised cosine function. That is, the model assumes a constant minimum delay at night, and uses a cosine function to represent the delay in the day time. The formula is

$$\Delta t_{klob} = DC + A \cos\left(\frac{2\pi(t - T_p)}{P}\right) \text{ seconds, if } \left|\frac{2\pi(t - T_p)}{P}\right| < \frac{\pi}{2} \quad (\text{F.2.1})$$

$$\Delta t_{klob} = DC, \text{ else}$$

where

$DC$  is the night time minimum delay value and is a constant 3 nano-seconds or 1.5 meters,

$P$  is the period of this cosine function, represents the time interval of the ionospheric activity in the day time,

$T_p$  is the local time of the maximum delay, typically 2 PM, and

$A$  is the amplitude of the cosine function, is the maximum delay in the day time.

Although, this model can only represent 50 to 60% of the ionospheric effect on the GPS pseudoranges, it is very easy to implement. First of all, the model requires the receiver to calculate the location of the ionosphere pierce points (IPPs) for each satellite in view in the geomagnetic coordinate. Then the receiver calculates the amplitude ( $A$ ) and the period

( $P$ ) of the cosine function using third order polynomials of IPP's geomagnetic latitude ( $\phi_m$ ). That is,

$$A = \sum_{n=0}^3 \alpha_n \phi_m^n \quad \text{sec, and} \quad (\text{F.2.2})$$

$$P = \sum_{n=0}^3 \beta_n \phi_m^n \quad \text{sec} \quad (\text{F.2.3})$$

where  $\alpha_i$  and  $\beta_i$ ,  $i = 0 \dots 3$  are from the GPS broadcast messages, and are chosen from a data base of 370 sets of constants. The data base was created by fitting the previously recorded data. The specific one being broadcast is based on the information of 1) the day of the year (a total of 37 groupings are used to represent seasonal effects), and 2) average solar flux values from the previous five days (10 groupings). These coefficients,  $\alpha_i$  and  $\beta_i$ , are chosen daily from sets of constants that reflect the sensitivity to solar-flux and seasonal variation. The database of these coefficients are from those stored in the master control station computer, and their numerical values were not scaled to reflect the transmitted quantities [Feess et al., 1987]

All the calculations, including the derivation of IPP locations, are simplified or approximated for the receivers with limited computation power. For example, the cosine function in the vertical delay is approximated by the Taylor series, so that Equation (F.2.2) is expressed as

$$\Delta t_{klob} = DC + A \cdot \left( 1 - \frac{x}{2} + \frac{x^2}{4!} \right) \quad \text{where } x = \frac{2\pi(t - T_p)}{P} \quad \text{and } |x| \leq \frac{\pi}{2}$$

Finally, the vertical delay is multiplied by an obliquity factor to account for the LOS corrections. Even though this model is not highly accurate, it does provide a relationship for longitudinal and latitudinal dependency of the ionosphere, and therefore we used it as the nominal model to transport the delay measurement from IPP locations to the grid point, as described in Chapter 4. For detailed implementation and the approximations of the model, the reader is referred to GPS-ICD-200 document. The next section describes the derivation of the IPP location and the obliquity factor used in this thin slab model.

### F.3 Obliquity Factor

The obliquity factor (OF) is used in the thin slab model to convert the slant to vertical delays. Figure F.3.1 shows the geometry of the OF derivations.

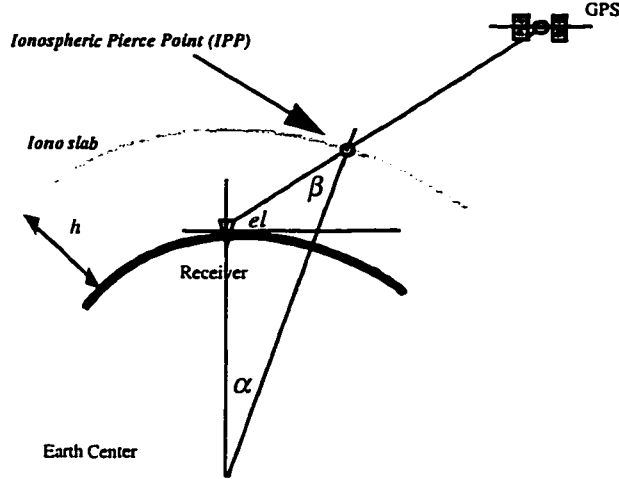


Figure F.3.1 Thin Slab Ionospheric Model Geometry

In the figure, the Earth angle,  $\alpha$ , can be calculated by

$$\alpha = 90 - el - \beta \quad (F.3.1)$$

Using the Law of Sine,

$$\frac{\sin \beta}{R_e} = \frac{\sin(el + 90^\circ)}{R_e + h} \quad (F.3.2)$$

we can find  $\beta$  as

$$\beta = \sin^{-1} \left[ \frac{R_e}{R_e + h} \cos(el) \right] \quad (F.3.3)$$

Then the obliquity factor is

$$OF = \frac{\text{slant delay}}{\text{vertical delay}} = \frac{1}{\cos \beta} = \frac{1}{\cos \left[ \sin^{-1} \left[ \frac{R_e}{R_e + h} \cos(el) \right] \right]} \quad (F.3.4)$$

Furthermore, using the trigonometry identity,  $\cos^2(el) + \sin^2(el) = 1$ ,  $OF$  can also be expressed as

$$OF = \frac{1}{\sqrt{1 - \left(\frac{R_e}{R_e + h} \cos(el)\right)^2}} \quad (\text{F.3.5})$$

#### F.4 Location of Ionospheric Pierce Point

The ionospheric pierce point (IPP) is defined in the thin slab model as the intersection of the satellite-receiver LOS and the ionospheric slab. As stated, the slab is assumed to be located at a height of 350 km above the earth's surface.

**[Known]:** Receiver's latitude ( $\phi_r$ ) and longitude ( $\lambda_r$ ), satellite's elevation ( $el$ ) and azimuth ( $az$ ) angles

**[Unknown]:** IPP's latitude ( $\phi_{ipp}$ ) and longitude ( $\lambda_{ipp}$ )

**[Solution]:** Assume  $\hat{I}_i$  is the basis of the Earth-centered-Earth-fixed (ECEF) frame,  $i=1,2,3$ ,  $\hat{L}_i$  is the receiver local east, north, vertical (ENU) frame, and  $\hat{P}_i$  is the pierce point frame with  $\hat{P}_3$  pointing to the local vertical upwards. Then the IPP's location can be expressed as

$$\bar{r}_i = \cos(\phi_{ipp}) \cos(\lambda_{ipp}) \hat{I}_1 + \cos(\phi_{ipp}) \sin(\lambda_{ipp}) \hat{I}_2 + \sin(\phi_{ipp}) \hat{I}_3, \text{ and} \quad (\text{F.4.1})$$

$$\bar{r}_p = \hat{P}_3 \quad (\text{F.4.2})$$

assuming a spherical earth with a radius normalized to unity. The key is to express  $\hat{P}_3$  in terms of the ECEF  $\hat{I}_i$  frame. We then can solve for  $\phi_{ipp}$  and  $\lambda_{ipp}$  by comparing with Equation (F.4.1).

From the coordinate transformation theory [Greenwood, 1988], the basis of the pierce point frame  $\hat{P}$  can be related to the ECEF frame  $\hat{I}$  through the receiver local frame  $\hat{L}$  by the transformation matrices:

$$\begin{aligned} \hat{P}_i &= T_{PII} \cdot \hat{I}_i \\ &= T_{PIL} \cdot \hat{L}_i = T_{PIL} \cdot T_{LII} \cdot \hat{I}_i, \quad i=1,2,3 \end{aligned}$$



The transformation matrix from  $\hat{L}$  to  $\hat{P}$ ,  $T_{P/L}$  can be calculated through two consecutive coordinate rotations of the earth angle  $\alpha$  and azimuth  $az$ :

$$T_{P/L} = R_1(-\alpha) R_3(-az)$$

$$= \begin{bmatrix} 1 & 0 & 0 \\ 0 & C_\alpha & -S_\alpha \\ 0 & S_\alpha & C_\alpha \end{bmatrix} \begin{bmatrix} C_{az} & -S_{az} & 0 \\ S_{az} & C_{az} & 0 \\ 0 & 0 & 1 \end{bmatrix}$$

Note that even though  $\hat{P}_1$  and  $\hat{P}_2$  are not pointing to local east and north,  $\hat{P}_3$  is now pointing to the IPP's local vertical and is the one to which we pay attention.

$T_{L/I}$ , the transformation matrix from ECEF  $\hat{I}$  frame to the receiver local  $\hat{L}$  (ENU) frame, can be calculated as

$$T_{L/I} = R_3(90^\circ) R_2(90^\circ - \phi_r) R_3(\lambda_r)$$

$$= \begin{bmatrix} 0 & 1 & 0 \\ -1 & 0 & 0 \\ 0 & 0 & 1 \end{bmatrix} \begin{bmatrix} C_{90^\circ - \phi_r} & 0 & -S_{90^\circ - \phi_r} \\ 0 & 1 & 0 \\ S_{90^\circ - \phi_r} & 0 & C_{90^\circ - \phi_r} \end{bmatrix} \begin{bmatrix} C_{\lambda_r} & S_{\lambda_r} & 0 \\ -S_{\lambda_r} & C_{\lambda_r} & 0 \\ 0 & 0 & 1 \end{bmatrix}$$

then

$$T_{P/I} = T_{P/L} \cdot T_{L/I}$$

$$= \begin{bmatrix} C_{az} & -S_{az} & 0 \\ C_\alpha S_{az} & C_\alpha C_{az} & -S_\alpha \\ S_\alpha S_{az} & S_\alpha C_{az} & C_\alpha \end{bmatrix} \begin{bmatrix} -S_{\lambda_r} & C_{\lambda_r} & 0 \\ -S_{\phi_r} C_{\lambda_r} & -S_{\phi_r} S_{\lambda_r} & C_{\phi_r} \\ C_{\phi_r} C_{\lambda_r} & C_{\phi_r} S_{\lambda_r} & S_{\phi_r} \end{bmatrix}$$

Looking at the third component,  $\hat{P}_3$ ,

$$\hat{P}_3 = \begin{bmatrix} T_{31} & T_{32} & T_{33} \end{bmatrix} \begin{bmatrix} \hat{I}_1 \\ \hat{I}_2 \\ \hat{I}_3 \end{bmatrix} \quad \text{or} \quad \hat{P}_3 = T_{31} \cdot \hat{I}_1 + T_{32} \cdot \hat{I}_2 + T_{33} \cdot \hat{I}_3$$

where

$$T_{31} = -S_\alpha S_{az} S_{\lambda_r} - S_\alpha C_{az} S_{\phi_r} C_{\lambda_r} + C_\alpha C_{\phi_r} C_{\lambda_r}$$

$$T_{32} = S_\alpha S_{az} C_{\lambda_r} - S_\alpha C_{az} S_{\phi_r} S_{\lambda_r} + C_\alpha C_{\phi_r} S_{\lambda_r}$$

$$T_{33} = S_\alpha C_{az} C_{\phi_r} + C_\alpha S_{\phi_r}$$

Compared with Equation (F.4.1), the latitude of the pierce point is

$$\begin{aligned} \therefore S_{\phi_{pp}} &= S_{\alpha} S_{az} C_{\phi_r} + C_{\alpha} S_{\phi_r} \text{ or} \\ \phi_{ipp} &= \sin^{-1}(S_{\alpha} C_{az} C_{\phi_r} + C_{\alpha} S_{\phi_r}) \end{aligned} \quad (\text{F.4.3})$$

Also,

$$C_{\phi_{pp}} C_{\lambda_{pp}} = T_{31} \text{ and}$$

$$C_{\phi_{pp}} S_{\lambda_{pp}} = T_{32}$$

Forming  $T_{31} (-S_{\lambda_r}) + T_{32} (C_{\lambda_r})$ , we have

$$C_{\phi_{pp}} \cdot \sin(\lambda_{ipp} - \lambda_r) = S_{\alpha} S_{az}$$

Finally, the longitude of the pierce point can be found as

$$\lambda_{ipp} = \lambda_r + \sin^{-1} \left( \frac{S_{\alpha} S_{az}}{C_{\phi_{pp}}} \right) \quad (\text{F4.4})$$

## Appendix G

# Interfrequency Bias Calibration Filter

A square root information filter (SRIF) is used to estimate the interfrequency bias (IFB) using the ionospheric measurements and the time variation of the obliquity factor. To take advantage of the time variation of the obliquity factors, the thin slab model of the ionosphere mentioned in Chapter 3 is used. As time progresses, we can separate the biases from a modeled ionosphere. This appendix describes the ionospheric model and the filter implementation of the IFB estimation process.

### G.1 Coordinate Frames for Ionospheric Pierce Points

To model the first-order behavior of the ionosphere in a sequential form, we need to find a good coordinate frame to express the ionospheric pierce points (IPPs).

Since the state of the ionosphere is mainly driven by the sun and geomagnetic activities, it stays at an approximately constant condition in the solar-magnetic frame. Therefore, it is easier to model the ionosphere in this coordinate frame. Furthermore, since the WAAS reference network in the continental U.S. (CONUS) area can only sample a window of ionosphere as the network passes through it, a local coordinate system is finally used for the filtering. Therefore, the IPPs are first calculated in Earth-centered-Earth-fixed (ECEF) coordinates  $(\lambda_{ipp}, \phi_{ipp})$ , then converted to the sun-earth (SE) frame  $(\lambda_{SE}, \phi_{SE})$  and the solar-magnetic (SM) frame  $(\lambda_{SM}, \phi_{SM})$ , sequentially. Finally, IPPs are expressed in the CONUS local coordinates  $(\lambda_L, \phi_L)$  and are to be used in the spherical harmonics model of the ionosphere.

#### G.1.1 Sun-Earth Frame

The sun-earth (SE) frame is a geocentric ECEF right-handed Cartesian frame.

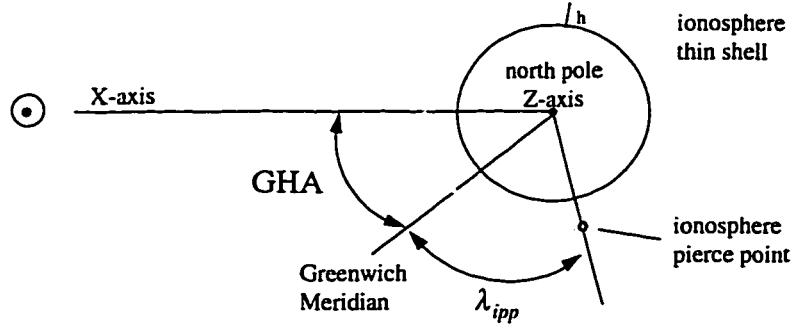


**Figure G.1.1 The Sun-Earth Coordinate Frame**

The Z axis of the SE frame is directed to the earth's north pole with X axis directed to the sun. Looking down from the north pole, this coordinate frame is shown in Figure G.1.1.

The longitude and latitude in this frame can be calculated as

$$\lambda_{SE} = \lambda_{ipp} + GHA \quad (G.1.1)$$

$$= \lambda_{ipp} + (\angle \text{ of GM from Noon})$$

$$= \lambda_{ipp} + \left\{ \angle (UTC \text{ of GM} - Noon) \cdot \frac{\pi}{12} \right\} \quad \text{in radians, and}$$

$$\phi_{SE} = \phi_{ipp} \quad (G.1.2)$$

## G.1.2 Solar-Magnetic Frame

The solar-magnetic (SM) frame is also an ECEF coordinate system. In this system, the Z-axis is pointing to the north magnetic dipole (78.5°N, 291.0°E) axis, and the Y-axis is perpendicular to the sun-earth line toward the dark side. Therefore, the X-axis is not always directly pointing to the sun, but rocking back and forth through 11.5 degree about the sun-earth line.

Using the latitude ( $\phi_{SE}$ ) and longitude ( $\lambda_{SE}$ ) expressed in the SE frame, the solar-magnetic coordinate of the IPPs can be calculated by one more coordinate transformation:

$$\mathbf{r}_{SM} = \mathbf{T}_{SM/SE} \cdot \mathbf{r}_{SE} \quad (G.1.3)$$

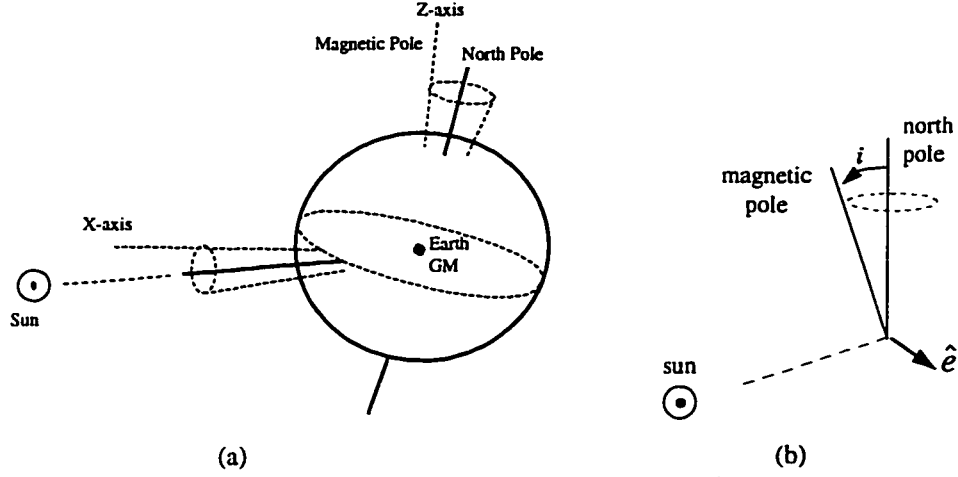


**Figure G.1.2 Solar-Magnetic Coordinate System**

$$(\lambda_{SE}, \phi_{SE}) \rightarrow \mathbf{r}_{SE} \text{ at altitude 350 km} \quad (\text{G.1.4})$$

$$\mathbf{r}_{SM} \rightarrow (\lambda_{SM}, \phi_{SM}) \quad (\text{G.1.5})$$

The coordinate transformation matrix can be calculated using the canonical expansion.

$$\mathbf{T}_{SM/SE} = I_{3 \times 3} - \sin(i) \hat{e} \times + [1 - \cos(i)] (\hat{e} \hat{e} - I_{3 \times 3}) \quad (\text{G.1.6})$$

where the unit vector  $\hat{e}$ , shown in the Figure G.1.2, is orthogonal to the plane formed by the north pole ( $\hat{N}$ ) and the magnetic pole ( $\mathbf{r}_M$ ). The calculation of  $\hat{e}$  comes from expressing the magnetic pole ( $78.5^\circ$  North,  $291^\circ$  East) in the solar-magnetic frame or

$$\mathbf{r}_M = [M_x \ M_y \ M_z]^T \quad (\text{G.1.7})$$

then

$$\bar{\mathbf{e}} = \hat{N} \times \mathbf{r}_M = \begin{bmatrix} \hat{i} & \hat{j} & \hat{k} \\ 0 & 0 & 1 \\ M_x & M_y & M_z \end{bmatrix} = -M_y \hat{i} + M_x \hat{j} \quad (\text{G.1.8})$$

and

$$\hat{e} = \frac{\bar{\mathbf{e}}}{\|\bar{\mathbf{e}}\|} = [e_x \ e_y \ e_z]^T \quad (\text{G.1.9})$$

Furthermore, the symbols in Equation (G.1.6) are

$$\hat{e} \times = \begin{bmatrix} 0 & -e_z & e_y \\ e_z & 0 & -e_x \\ -e_y & e_x & 0 \end{bmatrix} \quad (G.1.10)$$

$$\hat{e} \hat{e} = \hat{e} \cdot \hat{e}^T = \begin{bmatrix} e_x e_x & e_x e_y & e_x e_z \\ \cdot & e_y e_y & e_y e_z \\ \text{symm} & \cdot & e_z e_z \end{bmatrix} \quad (G.1.11)$$

### G.1.3 Local Frame

The local frame is referred to as the east-north-up (ENU) coordinate frame at a chosen center point of the CONUS region. This step expresses all the IPPs relative to the center and therefore makes it easier to use the spherical harmonics expansion to construct the ionospheric model.

The relationship of IPP location in the solar-magnetic frame to the local east-north-up frame can be expressed as

$$\bar{\mathbf{r}}_{ENU} = \mathbf{T}_{ENU/SM} \bar{\mathbf{r}}_{SM} \quad (G.1.12)$$

$$\bar{\mathbf{r}}_{ENU} = \cos(\phi_L) \sin(\lambda_L) \hat{e}_e + \sin(\phi_L) \hat{e}_n + \cos(\phi_L) \cos(\lambda_L) \hat{e}_u$$

Assuming the CONUS center in the solar-magnetic frame is  $(\lambda_L, \phi_L)$ , then

$$\mathbf{T}_{ENU/SM} = R_3(90^\circ) R_2(90 - \phi_c) R_1(\lambda_c) \quad (G.1.13)$$

$$\bar{\mathbf{r}}_{ENU} = \begin{bmatrix} -\sin(\lambda_c) & \cos(\lambda_c) & 0 \\ -\sin(\phi_c) \cos(\lambda_c) & -\sin(\phi_c) \sin(\lambda_c) & \cos(\phi_c) \\ \cos(\phi_c) \cos(\lambda_c) & \cos(\phi_c) \sin(\lambda_c) & \sin(\phi_c) \end{bmatrix} \begin{bmatrix} \cos(\phi_{SM}) \cos(\lambda_{SM}) \\ \cos(\phi_{SM}) \sin(\lambda_{SM}) \\ \sin(\phi_{SM}) \end{bmatrix}$$

$$\bar{\mathbf{r}}_{ENU} = E \hat{e}_e + N \hat{e}_n + U \hat{e}_u \quad (G.1.14)$$

then

$$\begin{aligned} E &= \cos(\phi_{SM}) [-\sin(\lambda_c) \cos(\lambda_{SM}) + \cos(\lambda_c) \sin(\lambda_{SM})] = \cos(\phi_{SM}) \sin(\lambda_{SM} - \lambda_c) \\ N &= -\sin(\phi_c) \cos(\phi_{SM}) [\cos(\lambda_c) \cos(\lambda_{SM}) + \sin(\lambda_c) \sin(\lambda_{SM})] + \cos(\phi_c) \sin(\phi_{SM}) \\ &= \cos(\phi_c) \sin(\phi_{SM}) - \sin(\phi_c) \cos(\phi_{SM}) \cos(\lambda_{SM} - \lambda_c) \end{aligned}$$

$$\begin{aligned}
U &= \cos(\phi_c) \cos(\phi_{SM}) [\cos(\lambda_c) \cos(\lambda_{SM}) + \sin(\lambda_c) \sin(\lambda_{SM})] + \sin(\phi_c) \sin(\phi_{SM}) \\
&= \sin(\phi_c) \sin(\phi_{SM}) + \cos(\phi_c) \cos(\phi_{SM}) \cos(\lambda_{SM} - \lambda_c)
\end{aligned}$$

Comparing the coefficients, we have

$$\phi_L = \sin^{-1}(N) \quad (\text{G.1.15})$$

$$\lambda_L = \text{atan2}(E, U) = \sin^{-1} \left( \frac{E}{\sqrt{E^2 + U^2}} \right) \quad (\text{G.1.16})$$

## G.2 Spherical Harmonics Expansion

A second-order spherical harmonic expansion is used to model the ionospheric vertical delay. The latitude and longitude in the equation are expressed in the solar-magnetic frame.

$$\begin{aligned}
&\sum_{n=0}^2 \sum_{m=0}^n \{C_{nm} \cos(m\lambda) + S_{nm} \sin(m\lambda)\} P_{nm}(\sin(\phi)) \quad (\text{G.2.1}) \\
&= C_0 + C_{10} \sin(\phi) + (C_{11} \cos(\lambda) + S_{11} \sin(\lambda)) \cos(\phi) \\
&\quad + C_{20} \cdot \frac{1}{2} (3 \sin^2(\phi) - 1) + (C_{21} \cos(\lambda) + S_{21} \sin(\lambda)) 3 \sin(\phi) \cos(\phi) \\
&\quad + (C_{22} \cos(2\lambda) + S_{22} \sin(2\lambda)) 3 \cos^2(\phi)
\end{aligned}$$

The coefficients, i.e. C's and S's, are estimated as part of the calibration process.

## G.3 Square Root Information Filter

In the estimation of the interfrequency biases, we have a long state vector (spherical harmonics coefficients, relative receiver IFBs and satellite IFBs), a large amount of measurements at each epoch (greater than 100 IPPs from 20 WRSs), and a Kalman filter in conventional covariance form usually with worrisome numerical stability. An implementation of Bierman's Square Root Information Filter (SRIF) was therefore chosen for this reason. SRIF is a sequential filter and has demonstrated excellent numerical stability and accuracy [Kaminski, et al., 1971]. This filter utilizes the

Householder orthogonal transformation in both the measurement and time updates of the square root of the information matrix which is the inverse of the covariance matrix [Bierman, 1975]. The implementation of SRIF is explained as follows.

In the discrete state-space formulation, the system and measurement equations are

$$x_{k+1} = \Phi_k x_k + w_k, \quad w_k \sim N(0, W_k), \quad W_k = E[w_k w_k^T] \quad (G.3.1)$$

$$z_k = H_k x_k + v_k, \quad v_k \sim N(0, V_k), \quad V_k = E[v_k v_k^T] \quad (G.3.2)$$

where the  $x$  is the state vector in Equation (3.4.2) and  $z$  is the ionospheric vertical delay measurement.  $H$  is the observation matrix and is defined in Equation (3.4.4).

To fit into the SRIF implementation, the measurement errors have to be first whitened first. A general whitening process is to use Cholesky decomposition to obtain the square root of  $V_k$ , or

$$V_k = L_k L_k^T \quad (G.3.3)$$

Multiplying the measurement Equation (G.3.2) with  $L_k^{-1}$ , we have

$$z_k^* = H_k^* x_k + v_k^*, \quad v_k^* \sim N(0, I) \quad (G.3.4)$$

where  $z_k^* = L_k^{-1} z_k$ ,  $H_k^* = L_k^{-1} H_k$ ,  $v_k^* = L_k^{-1} v_k$ , because

$$V_k^* = v_k^* v_k^{*T} = L_k^{-1} v_k v_k^T L_k^{-T} = I \quad (G.3.5)$$

For mutually uncorrelated measurements,  $V_k$  is a diagonal matrix and the above whitening process can be completed by simply multiplying each measurement equation with its inverse of the square root of the measurement noise. That is  $L_{k,i}^{-1} = 1/v_{k,i}$ , where  $i$  represents the  $i^{th}$  measurement.

Then the initial condition (*a priori*) of the state vector,  $\bar{x}_0$ , its uncertainty,  $\bar{P}_0$  must be expressed in terms of the following information form

$$\bar{z}_0 = \bar{R}_0 \bar{x}_0 + \bar{v}_0, \quad \bar{v}_0 \sim N(0, I) \quad (G.3.6)$$

with relationship  $\bar{P}_0 = (\bar{R}_0^T \bar{R}_0)^{-1}$  and  $\bar{z}_0 = \bar{R}_0 \bar{x}_0$ .

Likewise the initial process noise covariance matrix  $W_0$  should also be put into similar form



$$z_{w,0} = \mathbf{R}_{w,0} w_0 + \nu_{w,0}, \quad \nu_{w,0} \sim N(0, \mathbf{I}) \quad (\text{G.3.7})$$

with  $\mathbf{W}_0 = (\mathbf{R}_{w,0}^T \mathbf{R}_{w,0})^{-1}$  and  $z_{w,0} = \mathbf{R}_{w,0} w_0$

Then the measurement update with new measurement at epoch  $k$  is

$$\hat{\mathbf{T}}_k \begin{bmatrix} \bar{\mathbf{R}}_k & \bar{z}_k \\ H_k & z_k \end{bmatrix} = \begin{bmatrix} \hat{\mathbf{R}}_k & \hat{z}_k \\ 0 & e_k \end{bmatrix} \quad (\text{G.3.8})$$

and the best estimate and its covariance are  $\hat{x}_k = \hat{\mathbf{R}}_k^{-1} \hat{z}_k$  and  $\hat{\mathbf{P}}_k = \hat{\mathbf{R}}_k^{-1} \hat{\mathbf{R}}_k^{-T}$ .

The time update is

$$\bar{\mathbf{T}}_k \begin{bmatrix} \mathbf{R}_{w,k} & 0 & 0 \\ -\hat{\mathbf{R}}_k \Phi_k^{-1} & -\hat{\mathbf{R}}_k \Phi_k^{-1} & \hat{z}_k \end{bmatrix} = \begin{bmatrix} \bar{\mathbf{R}}_{w,k+1} & \bar{\mathbf{R}}_{wx,k+1} & \bar{z}_{w,k+1} \\ 0 & \bar{\mathbf{R}}_{k+1} & \bar{z}_{k+1} \end{bmatrix} \quad (\text{G.3.9})$$

and the optimal one step ahead prediction and its covariance matrix are  $\bar{x}_{k+1} = \bar{\mathbf{R}}_{k+1}^{-1} \bar{z}_{k+1}$  and  $\bar{\mathbf{P}}_{k+1} = \bar{\mathbf{R}}_{k+1}^{-1} \bar{\mathbf{R}}_{k+1}^{-T}$ . Note that both matrices in the above equations,  $\hat{\mathbf{T}}_k$  and  $\bar{\mathbf{T}}_k$ , are Householder orthogonal transformation matrices.

## G.4 IFB Estimation Program

Figure G.4.1 shows the block diagram of the data flow and updates of IFB estimation. In this diagram, IFB estimation can be viewed as a branch of the main WMS process. The IFB estimation program outputs its estimates at scheduled intervals to improve the calibration. The IFB values are applied to the measurement in the smoothing function. The values of IFBs are initialized with prior estimates (stored in a file).

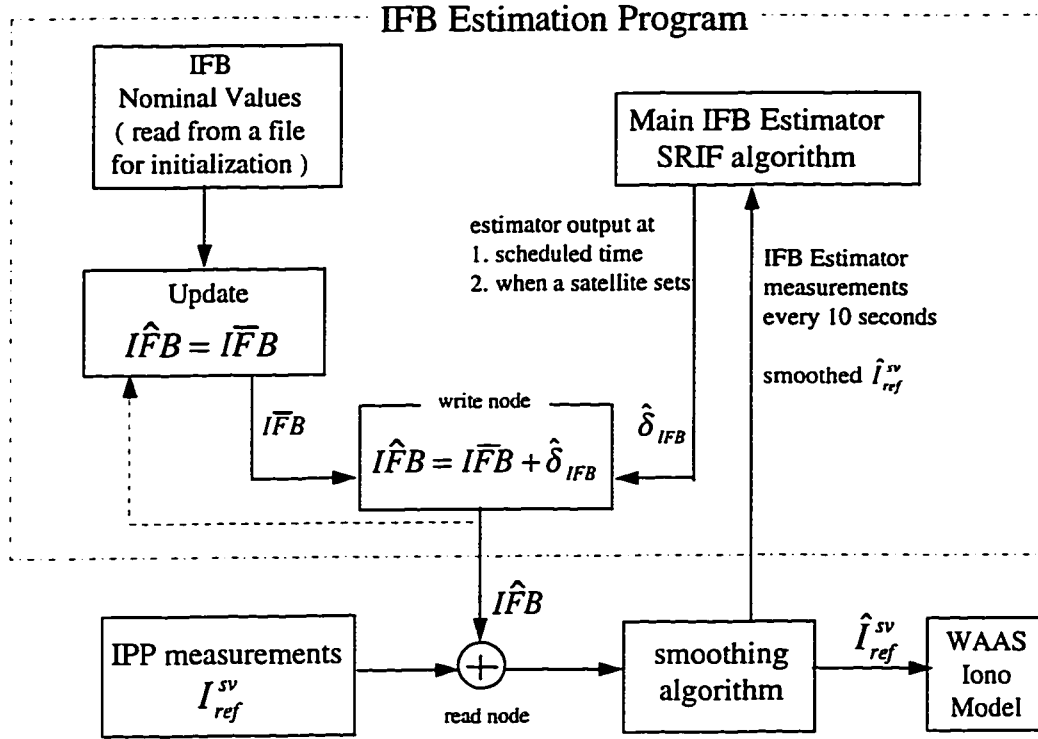


**Figure G.4.1 IFB Estimation Program Block Diagram and Flow Chart**

The a priori nominal values of IFB read from the file are  $T_{ref}^j + \frac{R_M}{\gamma - 1}; j = 1 \dots SV$  and  $\frac{R_i - R_M}{\gamma - 1}; i = 1 \dots TRS - 1$ , defined in Chapter 3.

To implement this estimator, four five data structures were defined and added to the main TMS main data structure, and they are

- IFB\_PARAM ----- to be read in by TMS (external)
- IFB\_MEAS ----- TMS supplies the measurements (external)
- IFB\_EST ----- major estimator structure (internal)
- IFB\_SV ----- output the result of SV IFBs to TMS (external)
- IFB\_TRS ----- output the result of TRS IFBs to TMS (external)

The following is the pseudo-code of the program

1. ReadIFB() in the tmsutil.c initialized the structures with a ifb\_nstb.est data file
2. TMS\_Process() calls IFB\_Estimation() every 10 seconds
3. Call the function IFB\_Estimation( ):

```

IFB_Estimation()
{
    if (first time) then (initialize the times)

```

```

build the SV list from the first 3 min data

after first 3 min, initialize the estimation process
    build the state vector and covariance matrix
    IFB_Estimation_Init() to initialize estimator states and covariance

SRIF estimation
    (Time Update (TU) and Measurement Update (MU) for each epoch
    be careful about bookkeeping of the rising and setting SVs)

    if (new epoch) {
        check if need to delete any SV that set already
        if (time to update ~30 min or 1 hr)
            update estimation results in the file/memory/screen

        SRIF_TU() for the entire state vector
    }

    check if (new SV), yes then add

    SRIF_MU() for every single satellite measurement for measurement
    update (note that SRIF_MU is done N times if N meas in one epoch)

} /* end of IFB_Estimation() */

```

## Appendix H

# WAAS Ionospheric Grid Model

## User Algorithm

This appendix is a description of the user's algorithm for using the WAAS ionospheric grid model. The interpolation algorithm that is defined in WAAS MOPS for calculating the ionospheric correction for user's IPP is presented below.

As mentioned in Section 4.4.4, for each the user's IPP, the ionospheric correction ( $I_v$ ) and  $UIVE$  are interpolated from the four grid points surrounding that IPP. Figure H.1 shows the geometry and Equations (H.1) and (H.2) are the interpolation formulas:

$$I_v = \sum_{i=1}^4 w_i \cdot I_i \quad (H.1)$$

$$UIVE = \sum_{i=1}^4 w_i \cdot GIVE_i \quad (H.2)$$

The weights ( $w_i$ ) in the interpolation are functions of IPP location and are calculated as [WAAS MOPS Appendix A]. The general weighting function is (using the notation in Figure H.1):

$$w(x, y) = x^2 y^2 (9 - 6x - 6y + 4xy) \quad (H.3)$$

$$\text{where } 0 \leq x \leq 1, \ 0 \leq y \leq 1$$

and the shape of the function is shown in Figure H.2.

The x and y parameters are calculated from

$$x = \frac{\Delta\lambda_{IPP}}{\text{longitude grid interval}} \quad (H.4)$$

$$y = \frac{\Delta\phi_{IPP}}{\text{latitude grid interval}} \quad (H.5)$$

The weight of each corner  $I_v$  and  $UIVE$  in Equation (H.1) is

$$w_1(x, y) = w(x, y) \quad (H.6)$$

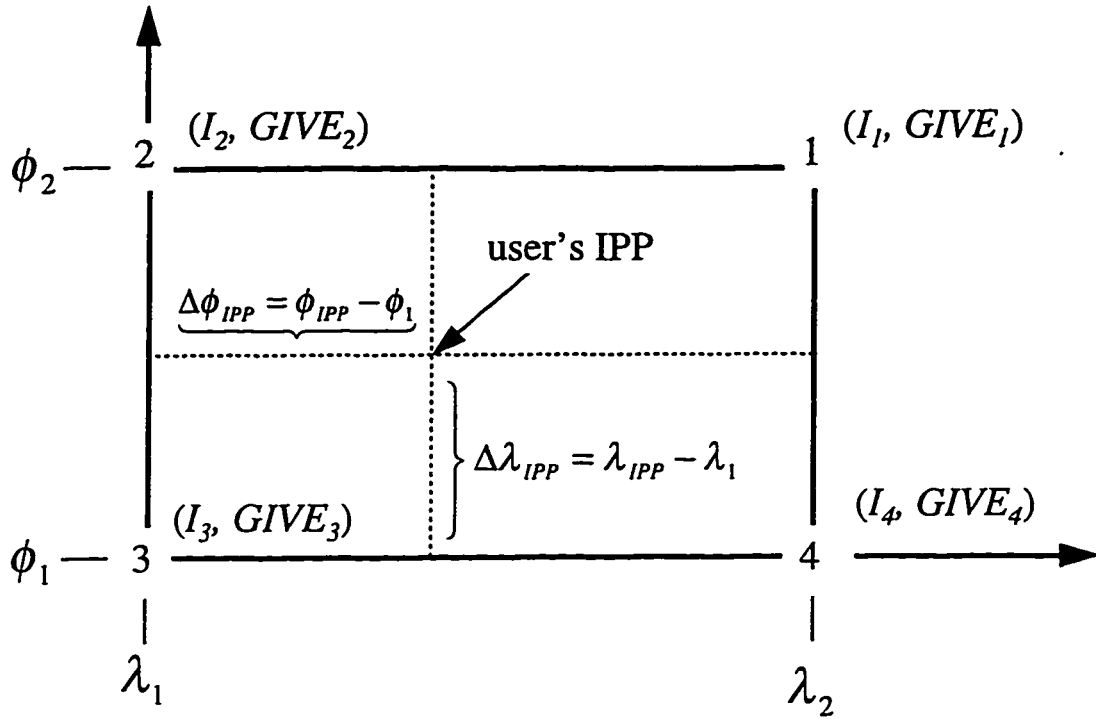


Figure H.1 Interpolation Algorithm Definitions

$$w_2(x, y) = w(1 - x, y) \quad (\text{H.7})$$

$$w_3(x, y) = w(1 - x, 1 - y) \quad (\text{H.8})$$

$$w_4(x, y) = w(x, 1 - y) \quad (\text{H.9})$$

There are two characteristics of the weighting function  $w(x, y)$  worth mentioning [Junkins et al., 1973]:

- 1)  $\sum_{i=1}^4 w_i = 1$ , that is the sum of the four weights is unity
- 2) The weighting function guarantees a smooth transition across the boundary of the grid cells. In other words, the first derivative of the weighting function at the boundary is zero.

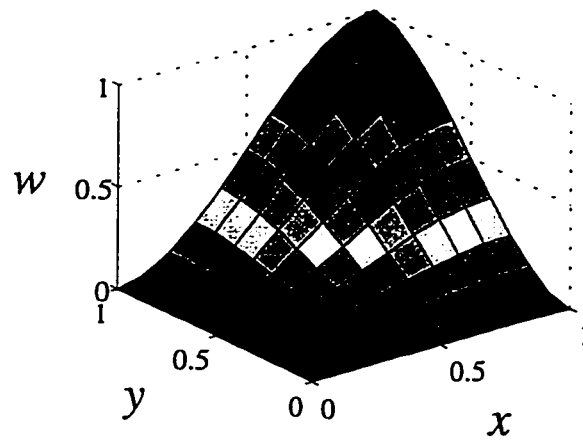


**Figure H.2 The Ionospheric Grid Model Interpolation Weighting function**

$$w(x, y) = x^2 y^2 (9 - 6x - 6y + 4xy)$$

Note that, as pointed out by Gazit's simulation [Gazit, 1997], a bilinear function [Press, 1992] can interpret the grid estimates better than Equation (H.3). However, this function does not have the smooth transition at the boundary between grid cells. Further investigation of the efficiency and accuracy of the interpolation function is need.

# Bibliography

AC120-28C, "Criteria for Approval of Category III Landing Weather Minima", *Federal Aviation Administration, Advisory Circular 120-28C*, Washington D.C., March 9, 1984.

Bassiri, S., G. A. Hajj, "Higher Order Ionospheric Effects on the GPS Observables and Means of Modeling Them", *Proceedings of The Third Annual Space Flight Mechanics*, Pasadena, 1993.

Beser, J., B. W. Parkinson, "The Application of NAVSTAR Differential GPS in the Civilian Community", 1981, *Global Positioning System, papers published in Journal of Navigation*, Volume II, pp167-196.

Bevington, P.R., D.K. Robinson, "Data Reduction and Error Analysis for the Physical Sciences", 2nd ed, 1992

Bierman, G.J., "Factorization Methods for Discrete Sequential Estimation," *Academic Press*, New York, 1977.

Black, H.D., "An Easily Implemented Algorithm for the Tropospheric Range Correction", *Journal of Geophysical Research*, Vol. 83, No. B4, April 10, 1978.

Black, H.D. A. Eisner, "Correcting Satellite Doppler Data for Tropospheric Effects", *Journal of Geophysical Research*, Vol. 89, No. D2, Page 2616-2626, April 20, 1984.

Bilitza, D. (ed), "International Reference Ionosphere 1990", *National Space Science Center/ World Data Center A for Rockets and Satellites*, Lanham, MD, Reprot number NSSDC/WDC-A-R&S 90-22. Also see IRI Model Web Page, <http://web.ngdc.noaa.gov/stp/IONO>.

Chao, Y.C., B.W. Parkinson, "The Statistics of Selective Availability and Its Effect on Differential GPS," *Proceedings of ION-GPS-93*, Salt Lake City, Utah, September, 1993.

- Chao, Y.C. Y.J.Tsai, T.Walter, C.Kee, P.Enge, B. Parkinson, "An Algorithm for Inter-frequency Bias Calibration and Application to WAAS Ionosphere Modeling", *Proceedings of ION-GPS-95*, Palm Spring, CA, September, 1995. pp 639-646.
- Chao, Y.C. Y.J. Tsai, J. Evans, C.Kee, T. Walter, P.K.Enge, J.D.Powell, B.W. Parkinson, "Generation of Ionospheric Correction and Confidence Estimates for WAAS", *Proceedings of ION 52nd Annual Meeting*, Cambridge, Massachussetts, June 19-21, 1996.
- Chao, Y.C., S. Pullen, P.K. Enge, B.W. Parkinson, "Study of Ionospheric Integrity," *Proceedings of ION-GPS-96*, Kansas City, Kansas, September, 1996
- Chou, H. T., "An Adaptive Correction Technique for Differential Global Positioning System", *Stanford University Ph.D Dissertation*, Department of Aeronautics and Astronautics, June, 1991.
- Cohen C., B. Pervan, B. Parkinson, "Estimation of Absolute Ionospheric Delay Exclusively through Single-Frequency GPS measurements", *Proceedings of ION-GPS-Albuquerque*, NM, Sept, 1992.
- Cohen, C., D.Lawrence, H.S. Cobb, B. Pervan, J.D. Powell, B. Parkinson, G.Aubrey, W. Loewe, D. Ormiston, B.D. McNally, D.Kaufmann, V. Wullschleger, and R. Swider, "Preliminary Results of Category III Precision Landing With 110 Automatic Landings of United Boeing 737 Using GNSS Integrity Beacons," *Proceedings of the 51st National Technical Meeting of the Institute of Navigation*, Anaheim, Page 157-166, January, 1995.
- Conker, R., B. El-Arini, T. Albertson, J. Klobuchar, P.Doherty, "Development of Real-Time Algorithms to estimate the Ionospheric Error Bounds for WAAS", *Proceedings of ION-GPS-95*, Palm Spring, CA, September, 1995. pp 1247-1258
- El-Arini M.B., P.A. O'Donnel, P.M. Kellam, J.A. Klobuchar, T.C. Wisser and P.J. Doherty, "The FAA Wide Area Differential GPS (WADGPS) Static Ionospheric Experiment," *Proceeding of the Institute of Navigation 1993 National Technical Meeting*, January 1993



- Enge, P. K. et al, "Architecture for a Civil Integrity Network Using Inmarsat," *Proceedings of 3rd International Technical Meeting of the Satellite Division, ION-GPS-90*, Colorado Springs, September, 1990.
- Enge, P. K., AA-297 *Flight Dynamics and Control Seminar*, Stanford University, 1992.
- Enge, P. K., T. Walter, S. Pullen, C. Kee, Y.C. Chao, Y.J. Tsai, "Wide Area Augmentation of the Global Positioning System", *Proceeding of the IEEE*, Vol. 84, No 8, August, 1996.
- Enge, P. K., T. Walter, Y.C. Chao, "Wide Area Differential GPS Reference System and Method," *United States Patent No. 5,621,646*, April, 1997.
- FAA WAAS, "Wide Area Augmentation System (WAAS)", Federal Aviation Administration, *RTCA Paper No. 276-94/SC159-542*, March 1994.
- Feess, W.A., S.G. Stephens, "Evaluation of GPS Ionospheric Time-Delay Model," *IEEE Transaction on Aerospace and Electronic System*, Vol. AES-23, No. 3, May, 1987
- Franklin, G., D. Powell, M. Workman, "Digital Control of Dynamic Systems", 2nd edition, *Addison-Wesley*, 1990.
- Gazit, Ran, "Kalman Filter Carrier Smoothing", *unpublished manuscript*, Stanford WAAS Lab, December, 1996.
- Gazit, Ran, *WAAS and RTK Simulation Package*, Stanford WAAS Lab, March, 1997.
- Greenwood, D.T., "Principle of Dynamics," *Prentice-Hall International*, 2nd edition, 1988.
- Hansen, A. J. "Computerized Ionospheric Tomography", *unpublished manuscript*, Stanford University, Nov. 1996.
- Hargreaves, J.K., "The Solar-Terrestrial Environment," *Cambridge Atmospheric and Space Science Series*, 1992.
- Hatch, R.R., "The Synergism of GPS Code and Carrier Measurements," *Proceedings of the Third Geodetic Symposium on Satellite Doppler Positioning*, Las Cruces, NM, Feb, 1982, pp1213-1232.
- Hopfield, H.S., "Two Quartic Tropospheric Refractivity Profile for Correcting Satellite Data", *Journal of Geophysical Research*, 74, Page 4487-4499, 1969.

- Hopfield, H.S., "Tropospheric Effect on Electromagnetically Measured Range: Prediction from Surface Weather Data", *Radio Science*, Vol. 6, No 3, Page 357-367, March 1971.
- Howe, B. M., "4-D Simulations of Ionospheric Tomography", *Proceedings of Technical Meeting, Institute of Navigation*, Santa Monica, CA, Jan. 14-16, 1997.
- ICD-GPS-200, *Revision B-PR*, Rockwell International, July 1992
- ION Newsletter, The Institute of Navigation Newsletter, Volume 7, Number 1, Spring, 1997.
- Junkins, Miller, Jancaitis, "A Weighting Function Approach to Modeling of Irregular Surfaces", *Journal of Geophysical Research*, Volume 78, No 110, April, 1973.
- Kaminski, P.G., A.E. Bryson Jr., S.F. Schmidt, "Discrete Square Root Filtering: A Survey of Current Techniques," *IEEE Trans. on Automatic Control*, Vol. AC-16, No. 6, December 1971, page 727-736.
- Kee C., B. Parkinson, P. Axlerad, "Wide Area Differential GPS Navigation", *Journal of the Institute of Navigation*, vol.38, no.2, Summer, 1991.
- Kee C., "Wide Area Differential GPS," *Ph.D dissertation*, Stanford University, December, 1993.
- Kee, C., T. Walter, Y.C. Chao, Y.J.Tsai, J.Evans, A.K.Barrows,E. Abbott, D. Powell, P. Enge, B. Parkinson, "Comparison of Full Vector and Common View WAAS Algorithm," *Proceedings of ION 51th Annual Conference*, Colorado Spring, Colorado, June 7, 1995.
- Kee, C., T.Walter, P.Enge, B. Parkinson, "Quality Control Algorithms on Wide-area Reference Station for WAAS," *Proceedings of 52nd Annual Meeting of the Institute of Navigation*, Cambridge, Massachussetts, June 19-21, 1996.
- Klobuchar, J.A, "Design and Characteristics of the GPS ionospheric Time Delay Algorithm for Single Frequency Users," *Proceedings of IEEE Position Location and Navigation Symposium*, Las Vegas, NV, Nov. 1986.
- Klobuchar, J.A., S. Basu, P.H. Doherty, "Potential Limitations in Making Absolute Ionospheric Measurements using Dual Frequency Radio Waves from GPS Satellites",

- Proceedings of the Seventh International Ionospheric Effects Symposium*,  
Alexandria, VA, May 1993.
- Klobuchar, J.A. "Ionospheric Effects on GPS", *Chapter 12 of Global Positioning System: Theory and Applications, Volume I*, edited by B. W. Parkinson and J. J. Spilker, AIAA, Progress in Astronautics and Aeronautics series, Volume 163, 1996.
- Knecht, D.J. Shuman, B.M. "Handbook of Geophysics and the Space Environment", *Chapter 4, The Geomagnetic Field*, 1985.
- Komjathy A., R.Langley, "Improvement of a Global Ionospheric Model to Provide Ionospheric Range Error Corrections for Single-frequency GPS Users", *Proceedings of ION 52nd Annual Meeting*, Cambridge, Massachusetts, June 19-21, 1996.
- Lawrence, D., J. Evans, Y.C. Chao, Y.J.Tsai, C.Cohen, T.Walter, P.Enge, J.D.Powell, B.Parkinson, "Integration of Wide Area DGPS with Local Area Kinematic DGPS," *Proceedings of IEEE PLANS 96*, Atlantic City, GA, April, 1996.
- Leon-Garcia, A. "Probability and Random Processes for Electrical Engineering," *2nd edition*, 1994
- Nagle, J. G.V. Kinal, "Geostationary Repeaters: A Low Cost Way To Enhance Civil User Performance of GPS and GLONASS," *Proceedings of IEEE PLANS-90*, Las Vegas, March, 1990
- US NGDC NOAA, National Geophysical Data Center, National Ocean and Atmosphere Administration, *web page*: <http://www.ngdc.noaa.gov/stp/SOLAR/SSN/annual.gif>
- Parkinson, B. W. "GPS Error Analysis", *Chapter 11 of Global Positioning System: Theory and Applications, Volume I*, edited by B. W. Parkinson and J. J. Spilker, AIAA, Progress in Astronautics and Aeronautics series, Volume 163, 1996.
- Press, William, B.P. Flannery, S.A.Teukolsky, W.T. Vetterling, "Numerical Recipes," *Chapter 14*, Cambridge Press, 2nd ed.
- Pullen, S.P., Y.C. Chao, P.K.Enge, B.W. Parkinson, "Effects of Local Ionospheric Anomalies on Navigation Performance and Integrity using WAAS", *Proceedings of IEEE PLANS*, Atlantic City, GA, April 1996.

- Raymund, T. D., J. R. Austen, S. J. Franke, C. H. Liu, J. A. Klobuchar, J. Stalker,  
 “Application of Computerized Tomography to the Investigation of Ionospheric  
 Structures,” *Radio Science*, Volume 25, Number 5, Page 71-789, Sep/Oct, 1990.
- RTCA Special Committee 159 Working Group 2 *Wide Area Augmentation System Signal  
 Specification*, March 1994
- RTCA Special Committee 159, Minimum Operational Performance Standards (MOPS)  
 for Airborne Supplemental Navigation Equipment Using GPS, *RTCA 204-91/SC159-  
 29*, These MOPS are modified by Technical Standard Order TSO-C129, which was  
 released December 10, 1992.
- Stull, R. B., “Meteorology Today For Scientists and Engineers —A Technical  
 Companion Book To Meteorology Today by C. D. Ahrens”, *West Publishing  
 Company*, 1995.
- Teasley, S.P., W.M.Hoover and C.R. Johnson, “Differential GPS Navigation,”  
*Proceedings of PLANS 80*, Atlantic City, New Jersey, December 1980, page 9-16
- Tsai Y.J., Y.C. Chao, T. Walter, C. Kee, D. Powell, P. Enge, B. Parkinson, “Evaluation  
 of Orbit and Clock Models for Real Time WAAS,” *Proceedings of the Institute of  
 Navigation 1995 National Technical Meeting*, CA, January 1995
- Tsai, Y.J., P.Enge, Y.C. Chao, T. Walter, C.Kee, J.Evans, A.Barrows, D.Powell,  
 B.Parkinson, “Validation of the RTCA Message Format for WAAS”, *Proceedings of  
 ION-GPS-95*, Palm Spring, CA, Sept. 1995
- Van Dierendonck, A. J. “Understanding GPS Receiver Terminology: A Tutorial on What  
 Those Words Mean”, *Proceedings of International Symposium on Kinematic Systems  
 in Geodesy, Geomatics and Navigation, KIS-94*, Banff, Canada, Aug 30- Sep 2, 1994
- van Grass, F., M. S. Braasch “Selective Availability”, *Chapter 17 of Global Positioning  
 System: Theory and Applications, Volume I*, edited by B. W. Parkinson and J. J.  
 Spilker, AIAA, Progress in Astronautics and Aeronautics series, Volume 163, 1996.
- Walter T., C. Kee, Y.C. Chao, Y.J. Tsai, U. Peled, J. Ceva, A. Barrows, E. Abbott, D.  
 Powell, P. Enge and B. Parkinson, “Flight Trials of the Wide Area Augmentation  
 System (WAAS),” *Proceedings of ION GPS-94*, Salt Lake City, Salt Lake City, Sept,  
 1994

- Walter, T., P. Enge, A. Hansen, "An Integrity Equation for Use With Space Based Augmentation Systems", *Proceedings of GNSS-97*, Germany, April, 1997.
- Wilson B., A. Mannucci, "Extracting Ionospheric Measurements from GPS in the Presence of Anti-Spoofing," *Proceeding of ION-GPS-93*, Salt Lake City, Sept, 1994.